Advanced Robotic Inspection Technology Based on Force Information Processing

July 2022

KUWAHARA, Hiroaki

A Thesis for the Degree of Ph.D. in Engineering

Advanced Robotic Inspection Technology Based on Force Information Processing

July 2022

Graduate School of Science and Technology
Keio University

KUWAHARA, Hiroaki

Acknowledgements

I have completed this dissertation to summarize the research as a member of the Murakami laboratory, the Faculty of Science and Technology at Keio University. I would like to express my gratitude to the people who supported the doctoral research.

First and foremost, my heartfelt appreciation should go to my supervisor, Professor Dr. Toshiyuki Murakami. He took time out of his busy schedule to discuss with me many times, and I gained many insights from the discussions. He is also a great motivator with excellent interpersonal skills. I was able to immerse myself in my research, encouraged by his comments. Without his guidance and supervision, the completion of this dissertation would not be a success.

I would like to express my deep gratitude to Emeritus Professor Dr. Kohei Onishi, who was my supervisor during my undergraduate and master's degrees and a member of my Ph. D. dissertation committee. His enormous support and insightful comments were invaluable and always to the point, which helped me. I believe that Real Haptics, which I studied under him, is one of the key foundations of this dissertation. His guidance has also been essential for completing this dissertation.

I greatly appreciate the members of my Ph. D. dissertation committee, Professor Dr. Hiromitsu Ohmori, Professor Dr. Kenjiro Takemura, and Associate Professor Dr. Takahiro Yakoh at Keio University. Their comments and advice were of tremendous help in enhancing the accuracy, novelty, and usefulness of this dissertation.

I acknowledge Assistant Professor Dr. Takahiro Nozaki at Keio University and the SUM group members for helpful discussions and comments on my research. The discussions about my research with them were constructive, enjoyable, and beneficial to me.

I have a special note of thanks to Mr. Tomio Iwata, Dr. Fujio Terai, Mr. Kazuo Ito, and Mr. Kazuma Hiraguri of Toshiba Corporation for their enthusiastic support in developing the generator inspection robot. With their support, I learned how to incorporate social issues into technical issues and manufacturing techniques to embody the results of my research.

I would like to convey my sincere thanks to Associate Professor Dr. Tomoyuki Shimono at Yokohama National University and Dr. Takahiro Mizoguchi at Motion LIB Corporation. Their advice regarding the force-sensorless percussion inspection devices highly improved the direction and quality of my research.

Finally, I would like to express my sincere gratitude to my family. They were always concerned about my health and kept sending me warm encouragement. Their support has enabled me to focus on the research, for which I am truly grateful.

I could carry out research on technology that contributes to society with the help of many people. The experience and personal connections I have acquired at Keio University are invaluable. I hope to leverage the assets to contribute to society.

July, 2022
Hiroaki Kuwahara

Contents

List of Figures

List of Tables

Chapter 1

Introduction

1.1 Robotic Inspection Technology for Social Infrastructure Facilities

With increasing growth in economy, social infrastructure facilities, such as roads, bridges, sewers, and harbor walls, have developed rapidly. Investment in social infrastructure facilities is strongly related to national policies. For example, in the United States, large-scale infrastructure development was promoted by New Deal programs in the 1920s, ahead of Japan. Consequently, in the United States, the aging infrastructure problem became apparent in the 1980s, affecting the economy and people's lives by making huge inroads in the budget for structural repair and constituting a significant safety hazard. In Japan, social infrastructure facilities built during the period of rapid economic growth in the 1980s are aging, and the number of aging infrastructure facilities is expected to increase rapidly, as shown in Fig. 1-1[1]. Thus, the problem of aging social infrastructure facilities is a global social issue that can occur anywhere in the world.

The aging of social infrastructure facilities can cause life-threatening accidents in the worst-case scenario. However, the reconstruction of existing social infrastructure facilities is often difficult owing to time and economic constraints. Therefore, the establishment of preventive maintenance technologies such as inspection and repair is urgently needed to ensure the continuous and stable operation of these facilities. Periodic inspections of these facilities are required by law, and until now, inspections and repairs have mainly been carried out manually. However, the inspection of such social infrastructure facilities requires dealing with highly restricted locations that are inaccessible and costly for people

[1] This graph was plotted based on the data described in [1].

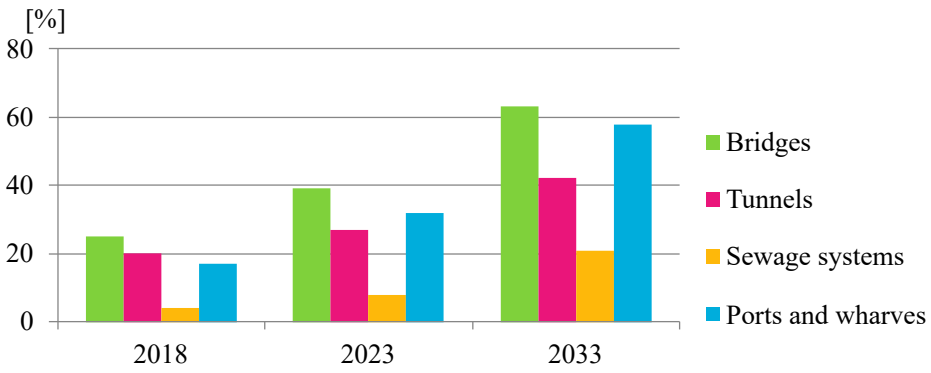

Fig. 1-1: Percentage of social infrastructure that is more than 50 years old.

to approach. Additionally, many sensory inspections require inspection skills; the training of skilled workers is expected to be costly and time-consuming. Therefore, the development and introduction of an infrastructure inspection robot that can access the inspection target and realize quantitative inspection instead of manual inspection have been attempted. Infrastructure inspection robots have a wide range of applications. Researches have been conducted to develop drones to inspect power lines[2–4], bridges[5], and power plants[6]; submersible robots to inspect nuclear reactors[7], dams[8], and port structures[9, 10]; and ground mobile robots to move through and inspect narrow spaces by installing sensors on wheeled[11–14], crawler[15–17], rail-running[18, 19], and leg-running robots[20–22] according to the traveling environment and road conditions. The inspection robots can be mainly classified into those that access the inspection location from outside or inside the structure. Drones and submersible robots that can move freely in the space are applied to access the inspection location from outside the structure. On the other hand, for inspection robots that access the inspection location from inside the structure, mobile robots that can adapt to the shape and condition of inside the structure are suitable. As mentioned above, mobile robots include wheeled, crawler, rail-traveling, and leg-traveling robots, but especially in environments where high mobility is required. Tracked vehicles are considered to be suitable for this purpose. Therefore, it can be said that tracked vehicle can be used for all inspection robots that access the inspection target from inside the structure.

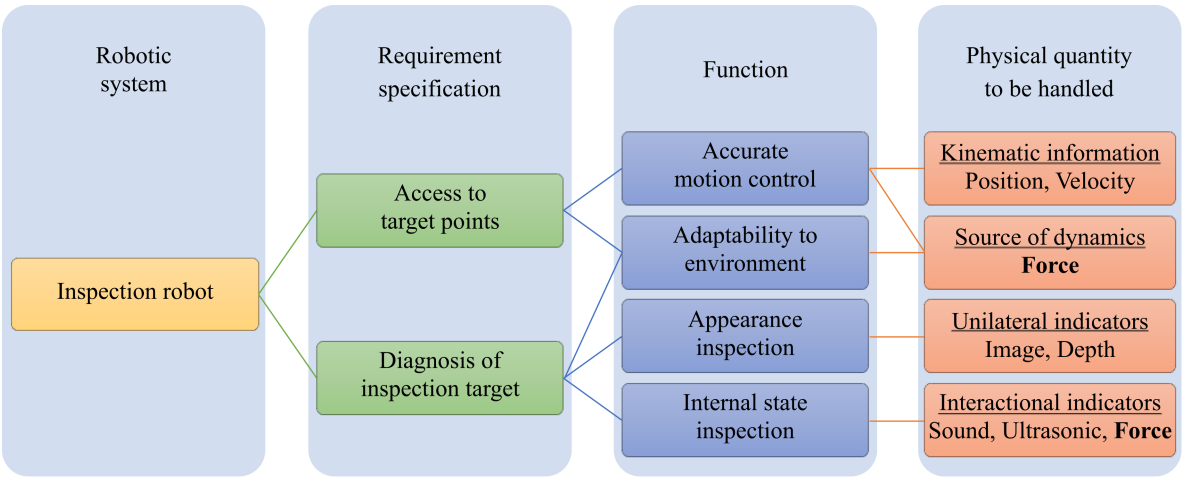

Fig. 1-2: Relationship between required function and physical quantity handled by inspection robots.

1.2 Relationship between Robotic Inspection Technology and Force Information

Figure 1-2 shows the relationship between the required function and the corresponding physical quantity to be handled by the inspection robot. The required functions of the inspection robot can be categorized into the access function to the target position and the function of diagnosing the inspection target.

The access function to the target position requires adaptability to the environment in which the inspection robot moves, such as the road surface environment and narrow space as well as the accurate motion control required for a general mobile robot. To realize the function of moving to the target position, it is naturally necessary to measure or estimate the position and speed of the inspection robot and control it. For more accurate movement, the driving force, which is the source of the movement dynamics, must be considered. Driving force is defined as the reaction force to the force given by the inspection robot to the road surface, which generates the kinetic energy of the robot. By effectively controlling the driving force, the motion of the inspection robot can be controlled. As a secondary effect of the driving force control, for example, slippage can be suppressed in slippery road environments. Additionally, when the inspection robot moves while changing its posture in a narrow space, for example, in a pipe, it can generate a pushing force in the narrow space to support its posture. Hence, the use of force information is effective for advancing the access function of inspection robots. This is because the access function of the inspection robot should be realized while the robot adapts to the mobile environment. However,

unlike the position or velocity, which represents motion, force is a physical quantity that represents the degree of interaction between objects in contact. Therefore, by controlling the interaction force between the inspection robot and moving environment, access function to the inspection target can be realized accurately while adapting to the environment.

Generally, inspections of structures are carried out on a periodic schedule, using data from previous inspections by people with inspection skills as a reference. Therefore, by replacing human inspections with robots, the data and technical knowledge from past inspections can be utilized. The diagnostic function of the inspection object has been popularized by the visual inspection of structures using vision systems such as cameras and lasers[23, 24]. However, it has been considered necessary to detect internal conditions to accurately determine the deterioration of structures, and diagnostic methods using sound[25,26], ultrasound[27,28], or acceleration[29] have been studied. In these methods, it is necessary to prepare sensors that are appropriate for each form of reverberation vibration and mount them on the inspection robot. Particularly, in inspection robots that move through environments that are inaccessible to humans, the size and placement of sensors is often affected owing to portability constraints. For example, to measure the echo vibration from a struck structure using a microphone or accelerometer, the sensitivity and directivity of the sensors should be changed according to the target. In addition, while ultrasonic inspection can detect defects inside structures non-destructive manner, its application is limited to objects whose failure locations can be predicted. However, these methods for diagnosing internal conditions have one thing in common: they are based on measuring the reverberating vibration from the object. As mentioned earlier, force information is physical information that represents an interaction. For example, when applying a striking force to an object, the reaction force of the object is felt. This reaction force is considered to be a form of reverberatory vibration. Therefore, the application of force information is expected to establish an unprecedented method of diagnosing internal conditions. Additionally, the use of reaction forces may eliminate the need for sensors to measure physical quantities that have been used in the past. This suggests that it may be possible to develop inspection devices that are advantageous to the portability constraints of inspection robots.

1.3 Motivation and Contribution

Force is the common physical information for the realization of each function. The motivation and contribution of this dissertation is to develop and demonstrate approaches for the advancement of robotic inspection capabilities based on force information processing. In this dissertation, the approach to extract and apply force information is studied from the perspective of each required function.

First, the driving force of the mobile part of the inspection robot is estimated and controlled to suppress slippage and improve the moving performance in road conditions. The posture of the inspection robot is then maintained by estimating and controlling the normal force in a confined space using a pushing force control mechanism consisting of a spring and an actuator. Finally, the reaction force when striking with a force-controlled device is estimated and the internal condition of the structure is diagnosed based on the reaction force.

1.3.1 Motion Control Based on Driving Force

Inspection robots must have mobile functions, especially positioning performance, to access the inspection position. Generally, however, two major disturbances in the motion control of the mobile mechanism that runs on a road surface prevent precise movement: 1) complex slippage on the ground and 2) nonholonomic constraints of vehicle motion. Therefore, the motion control for the mobile mechanism must consider slippage and nonholonomic constraints to ensure high-performance position control as a mobile mechanism. Slippage cannot be ignored, especially when the mobile mechanism is of the wire or crawler type where the contact area between the drive unit and road surface is larger than the wheel type. Various available simulators have been proposed to describe the motion mechanisms, including the slippage, of a tracked vehicle [30–32]. For the real-time detection of slippage in mobile mechanisms such as tracked vehicles and automobiles, there are several methods, including estimation using models and a Kalman filter[33], translational slippage detection based on a multi-sensor fusion of location data and inertial measurements [34], and lateral slippage detection based on image processing[35]. Moreover, several methods have been proposed to handle slippage, such as backstepping[36], sliding mode control[37], model predictive control[38], observer-based robust control[39, 40], and trajectory planning[41]. These methods are designed to ensure system robustness against slippage; however, they do not suppress slippage. Slippage is related to the friction coefficient between the drive unit and ground surface[42], and friction force corresponds to the crawler driving force. Considering these relations, slippage can be sup-

pressed by controlling the driving force. For automobiles, considerable research has been conducted on the friction modeling of tires. It has been found that the Magic formula[43] can represent it well; methods for estimating and controlling the driving force using this model have been proposed[44–47]. However, to consider the driving force of mobile mechanisms such as crawlers and wires, which have different dynamic models on the road surface, it is necessary to construct separate models. Therefore, this dissertation proposes a method for extracting and controlling driving force in a mobile mechanism without complex models, using the tracked vehicle as a subject. First, a method for estimating the vehicle velocity including slippage is proposed using disturbances to actuators with complex slippage information and machine learning. In this study, a disturbance observer (DOB)[48,49] is used to estimate the disturbance to the actuator. Next, the driving force is estimated from the estimated velocity using inverse kinematics and the driving force observer (DFOB). The effect of controlling the estimated driving force to suppress slippage in the translational direction is demonstrated. However, in the control of tracked vehicles using the driving force feedback to suppress slippage, the driving forces of the right and left crawlers interfere with each other. The driving force distribution that generates the yaw moment for turning must be considered because turning induces slippage along the turning direction. In a general mobile robot, when lateral slippage is ignored, a nonholonomic constraint is established to set a zero velocity along the lateral direction of the vehicle. In other words, nonholonomic constraints nullify commands along the lateral direction. Previous studies have shown that a position controller improved the path-following performance of a wheeled mobile robot by including compensation for lateral slippage[50,51]. Even for a tracked vehicle with crawlers that can slip, an improvement in the position control can be expected by suppressing the disturbance caused by the nonholonomic constraints while allowing adequate slippage. Therefore, this dissertation introduces a driving force distribution that induces slippage along the turning direction by decoupling the right and left driving forces using the instantaneous turning center. The driving force distribution ensures a tracked vehicle to slip while turning properly. Additionally, this dissertation defines the disturbance along the lateral direction of the tracked vehicle as the equivalent lateral disturbance. The equivalent lateral disturbance in the acceleration dimension is estimated by a workspace observer (WOB)[52], a coordinate transformation, and a selection matrix. Moreover, a virtual turning velocity reference is derived from the equivalent lateral disturbance and vehicle velocity. Hence, this dissertation proposes a virtual turning velocity control to suppress the lateral disturbance by making the turning velocity of the tracked vehicle follow the virtual turning velocity reference. A position controller is then integrated with the virtual turning velocity controller in the acceleration dimension. The resulting

control system ensures high-performance position tracking by suppressing the lateral disturbance while allowing the tracked vehicle to slip appropriately. The experiments demonstrate the effectiveness of the proposed method.

The proposed method of estimating velocity and driving force without using complex models and motion control based on driving force in this dissertation will contribute to the improvement of inspection robots' access performance to the inspection targets while adapting to the environment.

1.3.2 Force Control Mechanism Adaptable to Environment

General social infrastructure facilities have a three-dimensional structure, and inspection robots have to move in three-dimensional space. For example, when moving through a narrow space for pipeline inspection, it is necessary for the robot to maintain its posture even when gravity acts in the direction of fall. For this purpose, mechanisms have been proposed that generate adsorption forces on the road surface using magnets[53–55] and generate pushing forces that restrain the robots and maintain their postures[56–58]. In this way, the infrastructure inspection robot can move by adapting to the structure of the moving environment. For example, when traveling inside a structure mainly composed of magnetic iron, such as a generator, the magnetic force is an effective mechanism for movement[59–62]. However, when inspecting a non-magnetic structure, such as a pipeline, pushing force control mechanisms have been employed to maintain the posture by generating pushing force with an arm or other device mounted on the mobile mechanism against the inner wall of the moving environment. This pushing type can flexibly adapt to changes in gravity by controlling the pushing force. Previously, pushing force control mechanisms were achieved by actuators such as air cylinders[57, 63] or spring mechanisms[56]. Actuators are superior to spring mechanisms because they can actively generate the desired pressing force by control. However, because such mechanisms require power, they cannot maintain the posture of the robot in an emergency such as loss of power or air. Spring mechanisms use passive mechanical elements; hence, the force generated against the posture of the pushing control mechanism can be designed if the design value of the inspection target (e.g., the inner diameter of the pipe for piping) is determined in advance.

Therefore, this dissertation proposes pushing force control mechanisms for inspection robots that move and inspect narrow spaces, combining the aforementioned two control mechanisms. The proposed mechanism for controlling the pushing force consists of an actuator (motor or air cylinder) and a spring. At the time of pushing, a pushing force consisting of an actuator and a spring is generated, and the

environment's reaction force is model-based controlled. Additionally, in case of loss of power or air, the actuator stops pushing in; however, the spring maintains the pushing state and protects the sensor mounted on the actuator. The experiments demonstrated the performance of the proposed pushing force control method. The pushing force control mechanism proposed in this dissertation will contribute to the development of inspection robots with safety functions.

1.3.3 Force-based Diagnosis of the Internal Structural State

In many cases, the inspection robot should be a suitable size and shape for moving to the inspection position. For example, when the robot inspects the inner wall of a pipeline, it must be sufficiently small to move inside the pipe. In generator inspection, many robots are thin and curved to follow the gap between the rotor and stator[61]. Accordingly, the inspection devices such as a camera for visual inspection and the device for vibration inspection mounted on the inspection robot should meet the constraints of the inspection robot, such as its portable size, payload, and layout. Particularly, when inspecting the internal state using an inspection robot, a striking function to apply vibration to the object and sensing functions for reverberating vibration such as accelerometers, microphones, and ultrasonic probes are required. Generally, these functions are realized by separate devices, such as a hammer and microphone in percussion inspection[64–66]. In other words, if the striking and sensing functions of the reverberating vibration can be realized in a single device, the inspection device can be compacted to a size that can be mounted on the inspection robot, and the sensor placement constraint can be solved.

This dissertation proposes a percussion inspection device that realizes both the striking and sensing functions of reverberation vibration using a single device, regarding the reaction force given to a striking device when a structure is struck as a form of reverberation vibration. In the proposed percussion inspection device, a small motor is force-controlled to ensure a constant striking force. When striking with a force-controlled motor, the reaction force from the striking object becomes a disturbance to the motor. Therefore, a robust force control system can be realized by applying the DOB to generate the desired impact force. To realize the sensing function of reaction force without using additional sensors such as load cells, a reaction force observer (RFOB)[67] is applied in the proposed percussion inspection device. Additionally, this dissertation proposes a method to detect the internal state wedge loosening of a structure by estimating the internal structure model parameters based on the input/output characteristics of the percussion inspection device and evaluating the fixation of the internal components of the target. The feasibility of the reaction force estimation function and the inspection method of the proposed per-

cussion inspection device are evaluated through basic experiments. The inspection system described in this dissertation is the first of its kind in achieving both controls of the impact force and sense of reverberation vibration with a single mechanism, as well as using estimated force information as an index for inspecting structures. The percussion inspection device and the method of inspecting the internal state of structures using the device proposed in this dissertation will contribute to the advancement of robot inspection technology for social infrastructure facilities.

1.4 Organization of Dissertation

This dissertation is organized into seven chapters, as shown in Fig. 1-3. In Chapter 2, the fundamental technologies of motion control and force extraction considered in this dissertation are introduced. In Chapter 3, a development method of velocity estimation using the DOB and neural networks is discussed as a method to estimate velocity, including nonlinear and complex slippage. In Chapter 4, the design of a mobile robot motion control system based on driving force control is discussed as an approach to the control design of infrastructure inspection robots. In Chapter 5, a pushing force control mechanism using a force-controlled actuator and a passive mechanism is discussed as an approach to designing a mechanism to maintain posture in a confined space. In Chapter 6, a diagnosis method based on a percussion mechanism and a coupled vibration model that achieves actuator impact force control and reaction force estimation are discussed as an approach to the internal inspection of structures by infrastructure inspection robots. This dissertation is concluded in Chapter 7.

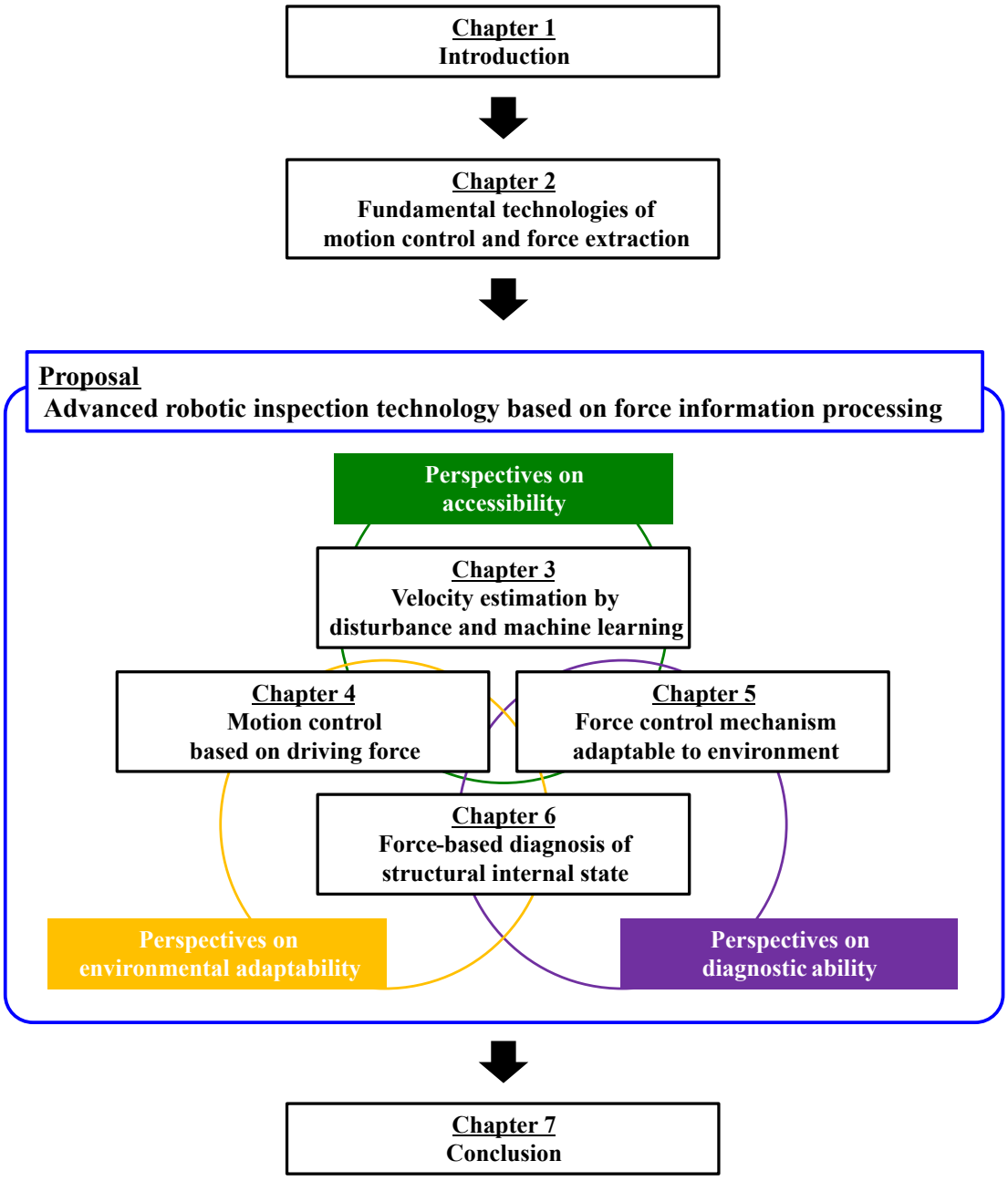

Fig. 1-3: Chapter organization.

Nomenclature

Abbreviations

DOB	Disturbance observer
RFOB	Reaction force observer
DFOB	Driving force observer
WOB	Workspace observer
NN	Neural network
PID	Proportional-integral-derivative
DOF	Degree of freedom

Variables

$x,\ y,\ z$	Position
f	Force
I	Current
m	Mass
J	Inertia
k	Stiffness
C	Controller
K	Gain
g	Cutoff frequency
k_t	Torque constant
t	Current time
s	Laplace operator

Superscripts

cmd	Command value
res	Response value
ref	Reference value
cmp	Compensation value
dis	Disturbance value
$\hat{\circ}$	Estimated value

Subscript

a	Armature
d	Value of DOB
rf	Value of RFOB
df	Value of DFOB

w	Value of WOB
g	Gravitational value
i	Value of integral
n	Nominal value

Chapter 2

Fundamental technologies of motion control and force extraction

2.1 Introduction

In this chapter, the fundamental technologies of motion control and force extraction used in this dissertation are described. Originally, the term "motion control" referred to the control of motion in systems that integrate electrical and mechanical systems, such as mechatronic devices and robots[68]. In a typical motion control system, the intended motion is achieved by controlling the position or force. To achieve a wide variety of motion control, it is necessary to ensure the robustness of the system to the motion[69]. In this dissertation, robust acceleration control[70] is considered a key motion control technology. This is because acceleration is a physical quantity common to position and force, obtained by the second derivative of position (first derivative of velocity) or by dividing force by inertia. Particularly, the robust control of acceleration is equivalent to the robust control of position (velocity) and force. In this study, a disturbance observer (DOB) is used to suppress the disturbance to the actuator to achieve robust acceleration control. Additionally, a reaction force observer (RFOB), which is designed by applying the DOB, is employed to extract force information from the actuator during motion.

This chapter is organized as follows: Section 2.2 describes the DOB for robust acceleration control. Section 2.3 describes the RFOB to estimate the reaction force and torque without using a force sensor. Section 2.4 describes position and force control based on robust acceleration control. Finally, the conclusion of this chapter is presented in Section 2.5.

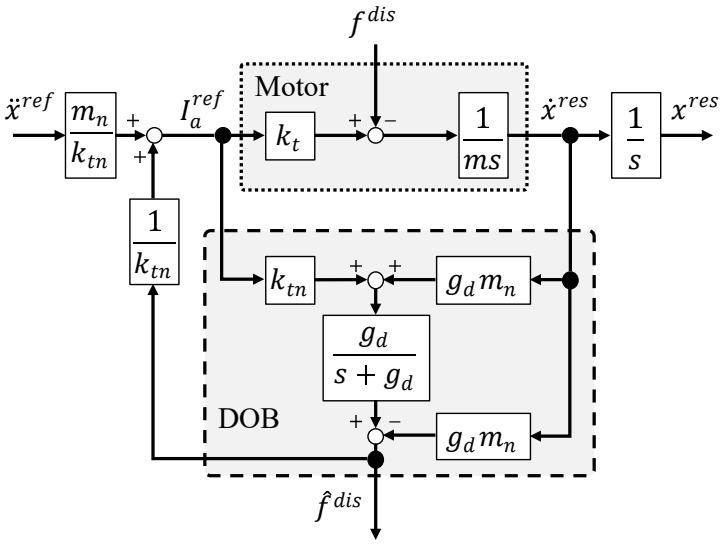

Fig. 2-1: DOB.

2.2 Disturbance Observer (DOB)

The primary role of the DOB[48, 49] is to estimate the disturbance added to the actuator. The feedback of the estimated disturbance achieves robust acceleration control of the actuator. When considering the linear motion of a one-degree-of-freedom (1DOF) motor to simplify the explanation, the motor's configuration and DOB are represented in Fig. 2-1. In Fig. 2-1, x, f, I, m, k_t, and g_d represent the position, force, current, mass, thrust coefficient, and cutoff frequency of the low-pass filter, respectively. The superscripts ^{ref}, ^{res}, and ^{cmp} represent the reference value, command value, and feedback amount to compensate for the disturbance f^{dis}, respectively. The subscripts $_a$ and $_n$ represent the actuator and nominal values, respectively. It should be noted that the DOB in Fig. 2-1 requires velocity information. When a position sensor such as a linear position encoder is used to measure motion, pseudo-differentiation using the cutoff frequency g_v of a low-pass filter is used to obtain derivative values such as the velocity response from the position response, as follows:

$$\dot{x}^{res} = \frac{g_v s}{s + g_v} x^{res}. \tag{2.1}$$

The disturbance force f^{dis} is expressed as follows:

$$f^{dis} = \delta m \ddot{x}^{res} - \delta k_t I_a^{ref} + f_{cf} + D\dot{x}^{res} + f^{ext} + f_{int}, \tag{2.2}$$

where f_{cf}, $D\dot{x}^{res}$, f^{ext}, f_{int}, δm, and δk_t denote the Coulomb friction term, viscous friction term, exter-

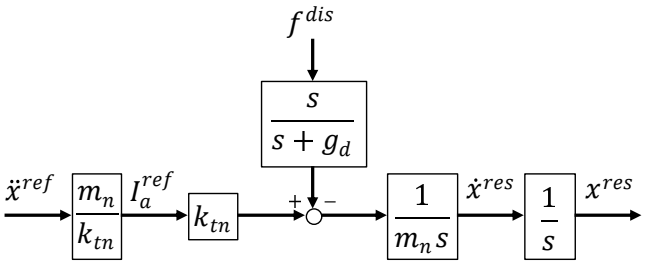

Fig. 2-2: Equivalent system with DOB.

nal forces, interaction forces (Coriolis force, centrifugal force, and gravity), and disturbances equivalent to inertia fluctuations and thrust constant fluctuations, respectively. Here, δm and δk_t are expressed as the difference between the actual and nominal values of mass m and thrust constant k_t as follows:

$$\delta m = m - m_n, \tag{2.3}$$

$$\delta k_t = k_t - k_{tn}. \tag{2.4}$$

In the DOB, the disturbance f^{dis} is estimated as $\hat{f}^{dis}$ as follows:

$$\hat{f}^{dis} = \frac{g_d}{s+g_d} f^{dis}. \tag{2.5}$$

By the feedback of the estimated disturbance force $\hat{f}^{dis}$, the acceleration response is obtained as follows:

$$\ddot{x}^{res} = \ddot{x}^{ref} - \frac{1}{m_n} \cdot \frac{s}{s+g_d} f^{dis}. \tag{2.6}$$

As indicated by (2.6), the system shown in Fig. 2-1 can be transformed into the equivalent system shown in Fig. 2-2. Figure 2-2 shows that the system is unaffected by disturbances when the cutoff frequency ranges from 0 to g_d. From Fig. 2-2, the disturbance force has almost no effect on the system when the cutoff frequency is sufficiently large. Particularly, when g_d is sufficiently large, the robust acceleration control is achieved.

The DOB can also be applied to rotational motion by replacing position x, force f, and mass m with angle θ, torque τ, and inertia J, respectively. Furthermore, the DOB can be applied in both the joint space and workspace[71]. In the multi-DOF robots, Jacobian matrices are included in the control systems[67].

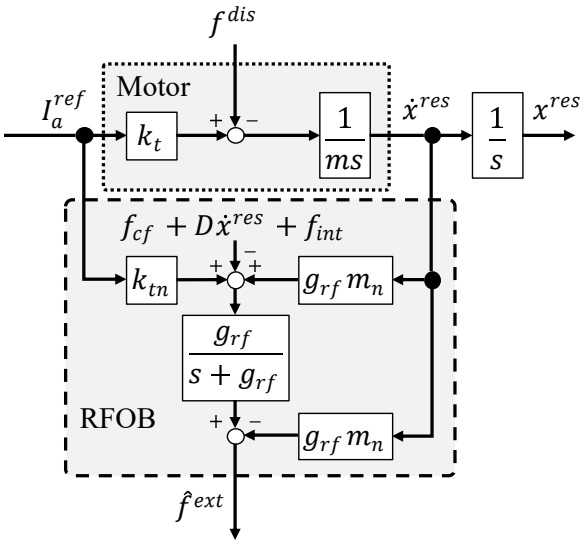

Fig. 2-3: RFOB.

2.3 Reaction Force Observer (RFOB)

External forces are helpful information to consider when interacting with the surrounding environment. The reaction force/torque observer (RFOB/RTOB)[67] is designed to estimate the external force/torque to the actuator by applying the DOB. An advantage of the RFOB is that the external force to the actuator can be estimated without any force sensors. The RFOB solves the problems caused by the force sensors, such as the narrow force-sensing bandwidth, adverse environmental effects such as temperature, and the non-co-location of a sensing point and an actuating point. Particularly, the force-sensing bandwidth and non-co-location of the points are critical issues because they affect the stability of the force control system[72]. Although the RFOB can estimate a wider bandwidth of the force information compared to a standard force sensor, it requires the prior identification of the Coulomb friction f_{cf}, viscous friction $D\dot{x}^{res}$, and interaction forces f_{int}. In a situation wherein the variables are perfectly identified and compensated while the DOB suppresses the disturbance, the disturbance coinciding with the external force is represented as follows:

$$f^{dis} = f^{ext}. \tag{2.7}$$

The configuration of the RFOB is shown in Fig. 2-3. Here, g_{rf} represents the cutoff frequency of the

low-pass filter. The estimated external force is computed by inserting the low-pass filter as follows:

$$\hat{f}^{ext} = \frac{g_{rf}}{s + g_{rf}} f^{ext}. \tag{2.8}$$

Using the RFOB, the reaction force can be estimated in the bandwidth up to the RFOB's cutoff frequency g_{rf}.

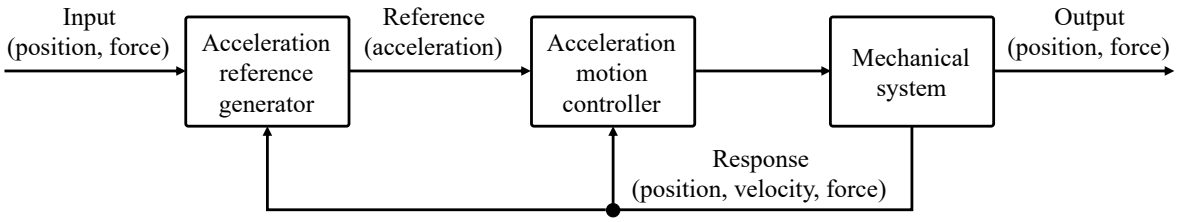

Fig. 2-4: Motion control based on acceleration control.

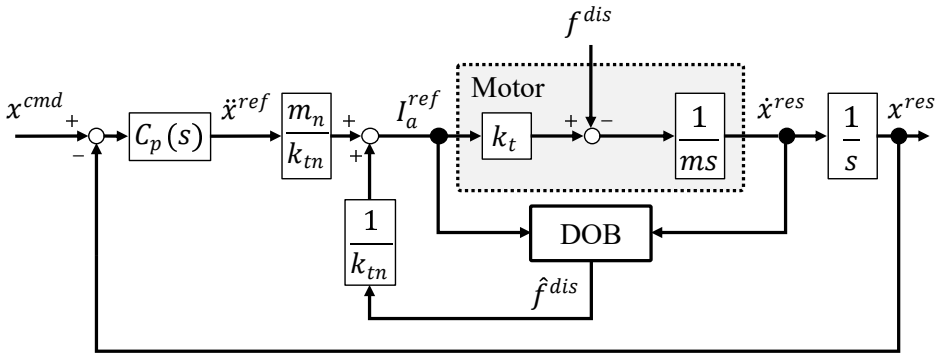

Fig. 2-5: Position control.

2.4 Motion Control Based on Acceleration Control

Figure 2-4 shows the structure of the motion control system, which is achieved by robustly controlling the acceleration. The motion control system is a cascade structure of an acceleration reference generator and acceleration controller. In Fig. 2-4, the outer controller shows an acceleration reference generator to achieve the intended goal of the control. The inner controller shows a robust motion controller. In this section, the position and force control systems designed based on the robust acceleration control are described.

2.4.1 Position Control

Position control is a simple example of the acceleration control system. First, an acceleration reference is generated to improve position tracking. This corresponds to the function of the outer loop in Fig. 2-4. Figure 2-5 shows a position control system based on the acceleration control. Here, the superscript ^{cmd} represents the command. $C_p(s)$ represents the position controller. The position controllers that generate the acceleration references are often designed using the proportional-derivative (PD) control as follows:

$$C_p(s) = K_{pp} + sK_{pd}, \tag{2.9}$$

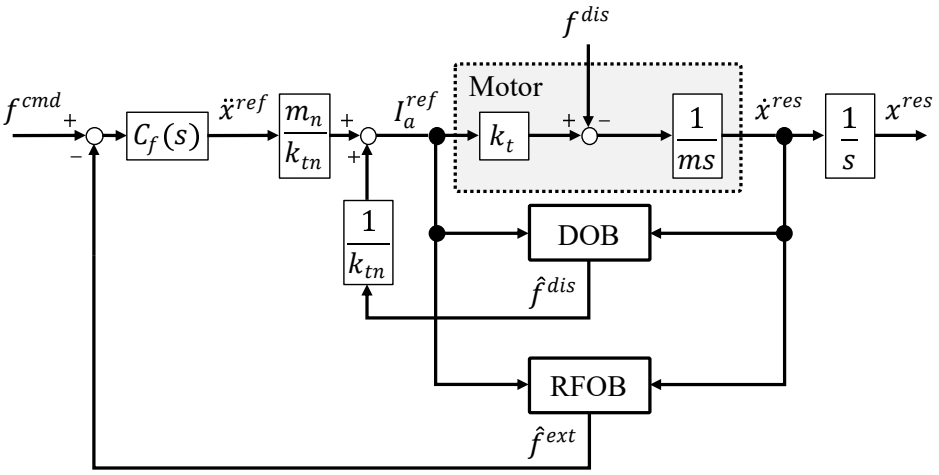

Fig. 2-6: Force control.

where K_{pp} and K_{pd} denote the P gain and D gain for the position, respectively. In this case, the target system is treated as a second-order system. In this position control system, the disturbances are suppressed by the DOB.

2.4.2 Force Control

The force control system based on the acceleration control is shown in Fig 2-6. Here, $C_f(s)$ represents the force controller. In this force control system, the external force to the actuator is extracted and controlled by the RFOB. The force controller $C_f(s)$, which generates the acceleration reference, is often designed as follows:

$$C_f(s) = K_{fp}, \tag{2.10}$$

where K_{fp} is the P gain for the force. For the stabilization of the force control system, it is more appropriate to use a D gain. However, because the derivative may amplify the force information noise, the force controller is designed without the D gain.

2.5 Summary

This chapter explained the fundamental technologies for motion control and force extraction. The robust acceleration control is the fundamental issue for motion control. This chapter first introduced the DOB for the robust acceleration control. Second, it showed that the estimation and compensation of disturbances by the DOB make the acceleration control system robust. Third, this chapter introduced the RFOB, which estimates the external force on the actuator without using a force sensor. Additionally, the chapter described the motion control based on acceleration control with concrete examples of position and force control systems.

Chapter 3

Velocity Estimation by Disturbance and Machine Learning

3.1 Introduction

This chapter proposes a method for estimating vehicle velocity, including slippage, using a disturbance to the actuator containing information on complex slippage, and machine learning.

Tracked vehicles have various applications, ranging from rescue tasks in rough terrains at disaster sites[73] to exploring extraterrestrial surfaces[74]. Since a tracked vehicle can secure contact between the crawler and road surfaces, excellent driving performance is expected. However, slippage occurs during its movement because of changes in the distribution of the shear stress generated between the road and crawler surfaces[42]. Generally, because slippage is not considered in the control of a mobile robot with wheels, it is not easy to apply this control method to tracked vehicles. Therefore, it is essential to develop estimation methods for slip states and to study their application in tracked vehicles.

Research in the terramechanics field has led to developments in soil models to clarify the slippage mechanism[75]. The constant changes in the soil model parameters depend on the road surface conditions and should be continuously estimated. However, the computational cost of real-time tracked vehicle control is a concern. Wills demonstrated an easy crawler-road handling method to estimate slip conditions using a pre-identified crawler-road contact friction model[76]. An experimental model was reported to demonstrate the relationship between the driving current and the slip velocity of a tracked vehicle[77]. Geometrical methods have also been proposed for obtaining the slip velocity from the instantaneous center of tracked vehicles[78, 79]. Two methods for describing the slip velocity can be

identified from existing literature: (1) The first is slip velocity as a parameter that correlates with the frictional force between the crawler and road surface from the perspective of dynamics. This method is based on the fact that the driving force of mobile mechanisms, including that of tracked vehicles, is related to the road surface friction[80, 81]. (2) Slip velocity is a parameter that expresses the relationship between the crawler and the vehicle translation velocities from the perspective of kinematics. Additionally, to control a tracked vehicle with slippage by estimating and controlling the driving force as described in the next chapter, an observer technique can be applied to estimate the driving force from the vehicle velocity. However, to improve the reliability of the driving force control under slippage, it is also necessary to estimate the velocity from slippage. Therefore, this chapter proposes a method to estimate the vehicle velocity, including slippage. In the proposed method, first, from the viewpoint of dynamics, the disturbance to the tracked vehicle's drive motor is assumed to contain the slippage information, and then the disturbance is estimated using the disturbance observer (DOB). A neural network is constructed to estimate the velocity of the tracked vehicle and is trained by the system using image processing. Experimental comparison and evaluation of the velocity estimation performance of the tracked vehicle are demonstrated using the proposed method and general mobile robot velocity estimation methods. The performance of the proposed method is also evaluated in environments that are different from the environment in which the vehicle is trained. The applicability of the proposed velocity estimation method is discussed based on the experimental results. Additionally, to extend the proposed method to the three-dimensional running of the tracked vehicle, the proposed velocity estimation method is extended to include gravity compensation for acceleration.

This chapter is organized as follows: Section 3.2 describes the tracked vehicle model. Section 3.3 proposes a velocity estimation method using the DOB and machine learning. Section 3.4 evaluates the velocity estimation performance using the trained neural network. In Section 3.5, the neural network estimation performance is evaluated in environments that are different from the environment in which it is trained. Section 3.6 discusses the effect of gravity compensation on the velocity estimation performance improvement when driving on a slope. In Section 3.7, the effect of the estimated disturbance on the velocity estimation is discussed from the viewpoint of robustness to environmental changes. This chapter is summarized in Section 3.8.

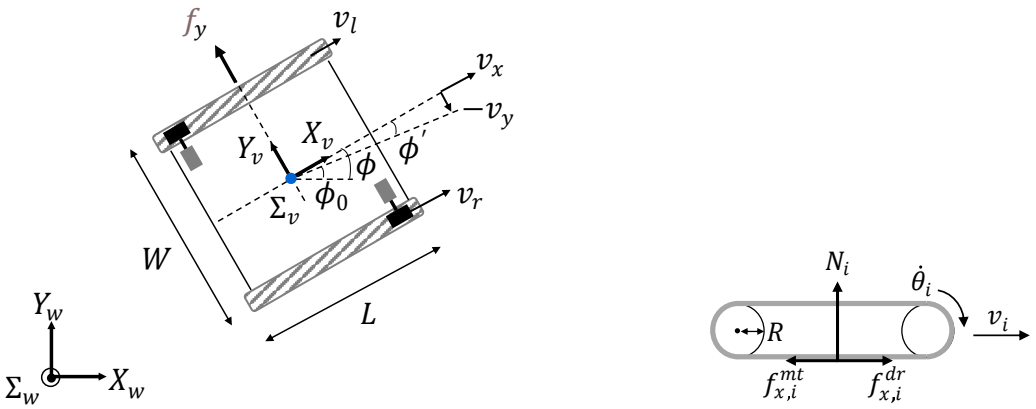

(a) Top view. (b) Side view.

Fig. 3-1: Tracked vehicle model.

3.2 Tracked Vehicle Model

3.2.1 Tracked Vehicle Model

Figure 3-1 shows the model of the tracked vehicle. Table 3.1 lists the model parameters, where the subscript i denotes the motor ID (r: right, l: left). The world and vehicle coordinates are defined as shown in Fig. 3-1. The center point and traveling directions of the tracked vehicle are the vehicle coordinates' origin and axes. The position vector representing the position and posture of the tracked vehicle in the world coordinates is defined as follows:

$$\boldsymbol{x} = [x, y, \phi]^T. \tag{3.1}$$

The turning angle is defined as follows:

$$\phi = \phi_0 + \phi'. \tag{3.2}$$

3.2.2 Kinematics

From Fig. 3-1 (a), the vehicle velocities in the world coordinates are transformed into vehicle coordinates using the following equations:

$$\dot{x}\cos\phi + \dot{y}\sin\phi = v_x, \tag{3.3}$$

$$\dot{x}\sin\phi - \dot{y}\cos\phi = v_y. \tag{3.4}$$

Table 3.1: Parameters of tracked vehicle model.

Parameter	Description
$\Sigma_w\ (X_w, Y_w)$	World coordinates
$\Sigma_v\ (X_v, Y_v)$	Vehicle coordinates
W	Vehicle thread
L	Crawler length
R	Sprocket radius
ϕ	Turning angle with slip angle
ϕ_0	Turning angle without slip angle
ϕ'	Slip angle
v_x	Vehicle translational velocity
v_y	Lateral slip velocity
f_y	Lateral force
v_i	Crawler velocity
$\dot{\theta}_i$	Crawler motor velocity
N_i	Normal force on crawler
$f_{x,i}^{mt}$	Force on road surface due to the motor torque
$f_{x,i}^{dr}$	Driving force

From (3.4), the nonholonomic constraint of the tracked vehicle is not satisfied owing to the slip. The slip angle of the tracked vehicle is obtained using the following equation:

$$\phi' = \tan^{-1}\frac{v_y}{v_x}. \tag{3.5}$$

The kinematic relationship between the vehicle velocity $(v_x, \dot{\phi})$ and crawler velocity (v_i) is as follows:

$$v_x + \frac{W}{2}\dot{\phi} \quad = v_r = (1-\lambda_r)R\dot{\theta}_r, \tag{3.6}$$

$$v_x - \frac{W}{2}\dot{\phi} \quad = v_l = (1-\lambda_l)R\dot{\theta}_l, \tag{3.7}$$

where λ_i represents the slip ratio between the crawler and road surface or between the crawler and its sprocket. The slip ratio is defined as follows:

$$\lambda_i = \begin{cases} \dfrac{R\dot{\theta}_i - v_x}{R\dot{\theta}_i} & (R\dot{\theta}_i \geq v_x) \\ \dfrac{R\dot{\theta}_i - v_x}{v_x} & (R\dot{\theta}_i < v_x). \end{cases} \tag{3.8}$$

3.2.3 Dynamics

From the equation of motion, the dynamic relationship between the vehicle velocity and frictional force (driving force) between the crawler and road surfaces is expressed as follows:

$$m\dot{v}_x = f_{x,r}^{dr} + f_{x,l}^{dr}, \tag{3.9}$$

$$m\dot{v}_y = f_y, \tag{3.10}$$

$$J\ddot{\phi} = \frac{W}{2}(f_{x,r}^{dr} - f_{x,l}^{dr}), \tag{3.11}$$

where m and J are the mass and moment of inertia of the vehicle, respectively. When the vertical pressure at the crawler contact surface is constant, the driving force can be quasi-experimentally expressed as follows[42]:

$$f_{x,i}^{dr} = N_i \mu f(\lambda_i, k, L), \tag{3.12}$$

where $\mu(\lambda_i)$ and $f(\lambda_i, L)$ represent the dynamic friction coefficient and a function with the slip ratio λ_i, shear displacement coefficient k, and crawler length L as arguments, respectively. From (3.12), the driving force depends on the slip ratio.

From Fig. 3-1 (b), the equation of motion of the crawler is expressed as follows:

$$J_m \frac{\dot{v}_i}{R^2} = f_{x,i}^{mt} - f_{x,i}^{dr}, \tag{3.13}$$

where J_m is the motor shaft conversion moment of inertia. Thus, the driving force moves the tracked vehicle, which simultaneously behaves as a disturbance and acts on the motor.

3.3 Velocity Estimation Method

As described in Section 3.2.2, the tracked vehicle slips in the translational and turning directions. However, when measuring the turning velocity with the gyro sensor attached to the tracked vehicle, the velocity caused by the slippage in the turning direction is included in the measured velocity. Therefore, methods for estimating the translational velocity of tracked vehicles, including slippage, are considered.

Conventional velocity estimation methods for mobile robots can be classified into the following four types[82]:

- Estimation based on kinematics, such as velocity conversion from motor angular velocity to translational velocity.
- Estimation based on dynamics, such as the Kalman filter[83].
- Estimation using a designed observer, such as a velocity estimation observer[84].
- Estimation using artificial neural networks.

All of these methods, except the method using the artificial neural network, require a model that additionally includes slippage. However, in the estimation method using the artificial neural network, nonlinear information can be expressed by the neural network, even in the absence of complex models. Therefore, the neural network structure for velocity estimation of the tracked vehicle, including nonlinear slip, is examined.

From (3.6) and (3.7), the translational velocity v_x of the tracked vehicle can be expressed by the function f_1 of the angular velocity of the motor, given by

$$v_x = \frac{R}{2}\left((1-\lambda_r)\dot{\theta}_r + (1-\lambda_l)\dot{\theta}_l\right) \equiv f_1(\dot{\theta}_r, \dot{\theta}_l). \tag{3.14}$$

From (3.9), the translational acceleration $\dot{v}_x$ can be expressed by the function f_2 of the estimated disturbance to the motor, given by

$$\dot{v}_x = \frac{f_{x,r}^{dr} + f_{x,l}^{dr}}{m} \equiv f_2(\tau_r^{dis}, \tau_l^{dis}). \tag{3.15}$$

Generally, the translational acceleration $\dot{v}_x$ is measured by an accelerometer, from which the translational velocity is obtained by integration over time. However, in this approach, the effects of drift and noise appear in the calculated velocity. To improve this issue, in the proposed approach, a neural network was built with the estimated translational velocity ($\hat{v}_x$) as the output, according to the measured motor

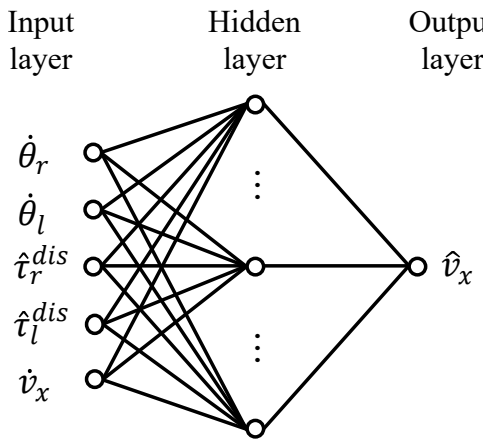

Fig. 3-2: Translational velocity estimation neural network (TVNN).

velocities ($\dot{\theta}_r^{res}, \dot{\theta}_l^{res}$), estimated motor disturbances ($\hat{\tau}_r^{dis}, \hat{\tau}_l^{dis}$), and translational acceleration ($\dot{v}_x^{res}$) as the inputs, as shown in Fig. 3-2. This neural network is defined as a translational velocity estimation neural network (TVNN). The TVNN consists of a feed-forward neural network with three layers: input, hidden, and output layers, which are used in general nonlinear regression problems. A hyperbolic tangent sigmoid function and a linearized transfer function were used as the weighting functions for the hidden and output layers, respectively. The training of TVNN can be performed using supervised machine learning or other methods. The trained TVNN generates a regression function to determine the translational velocity from the tracked vehicle information.

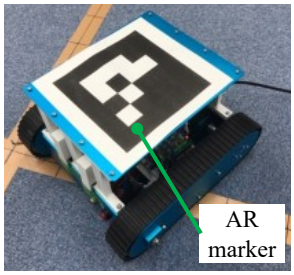

(a) Experimental device.

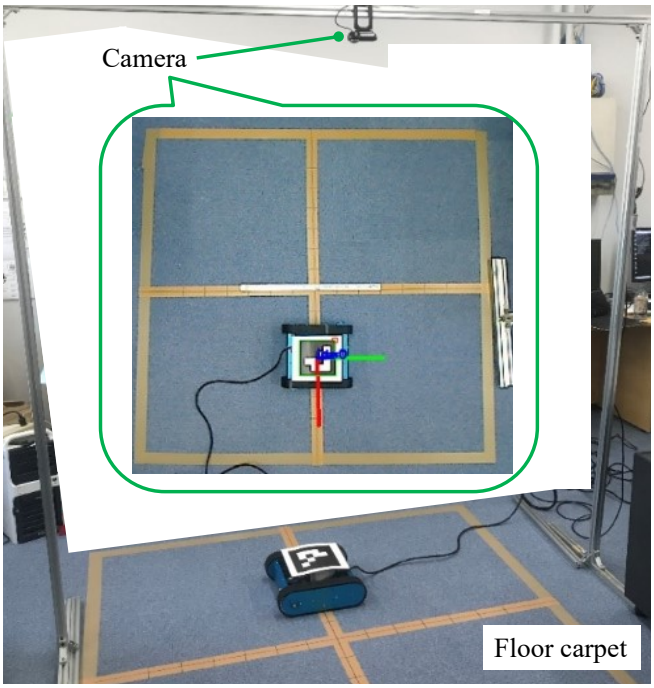

(b) Measurement environment.

Fig. 3-3: Experimental setup.

3.4 Evaluation of Velocity Estimation Performance by TVNN

3.4.1 Experimental Conditions

Figure 3-3 shows the experimental setup. The tracked vehicle used in the experiment was driven by two direct-current (DC) motors with encoders. Additionally, it was equipped with an inertial measurement unit (IMU) to measure the acceleration and angular velocity. The Kalman filter was applied to the measured acceleration and angular velocity to estimate the turning angle. An augmented reality (AR) marker[85] was installed on the surface of the tracked vehicle, and the position of the tracked vehicle was detected by processing the images captured by a camera. Tables 3.2 and 3.3 show the components and specifications of the experimental devices.

3.4.2 Evaluation of Velocity Estimation Performance

The angular velocity of the motor was controlled during TVNN training. The angular velocity command provided for the TVNN training is shown in Fig. 3-4. The parameters of the proportional-integral (PI) controller and the DOB, shown in Table 3.4, were used to control the motor angular velocity.

Table 3.2: Components of experimental devices.

Component	Type	Manufacturer
Tracked vehicle frame	10022	Nexus robot
DC motor	2342012CR	Faulhaber
Motor driver	ESCON 24/2	Maxon
IMU	BNO055	Bosch
Controller	STM32 Nucleo-F446RE	STMicroelectronics
Camera	Brio C1000eR	Logicool

Table 3.3: Specifications of experimental devices.

Parameter	Value
Mass of tracked vehicle m	5.3 kg
Vehicle thread W	0.24 m
Vehicle length L	0.25 m
Motor shaft conversion moment of inertia J_m	3.1 E-06 kgm^2
Sprocket radius R	0.05 m
Torque constant of motor k_{tn}	0.0134 Nm/A
Motor encoder resolution (quadruple)	3072 PPR
Sampling time	3 ms
Camera frame rate	60 fps

The information from the tracked vehicle was used as the input, while the translation velocity in the vehicle coordinates, calculated from the position detected by image processing, was used as the supervisory data. The number of neurons in the hidden layer of the TVNN was determined to be 15, according to prior trials. The TVNN was trained using the Bayesian regularization error backpropagation method.

Figure 3-5 shows the learning results. Panel (a) shows the relationship between the actual output and the prediction by the TVNN, indicating that the correlation is enough high (R=0.96588). In addition,

Table 3.4: Control parameters in learning experiment.

Parameter	Value
Motor angular velocity control P gain	500
Motor angular velocity control I gain	10
Cutoff freq. of DOB g_d	188.4 rad/s

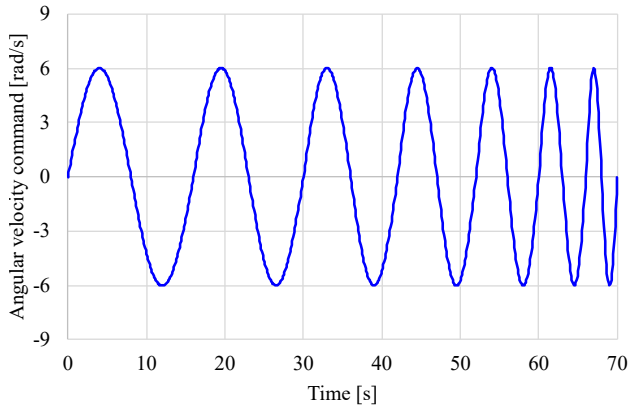

Fig. 3-4: Angular velocity command in TVNN learning.

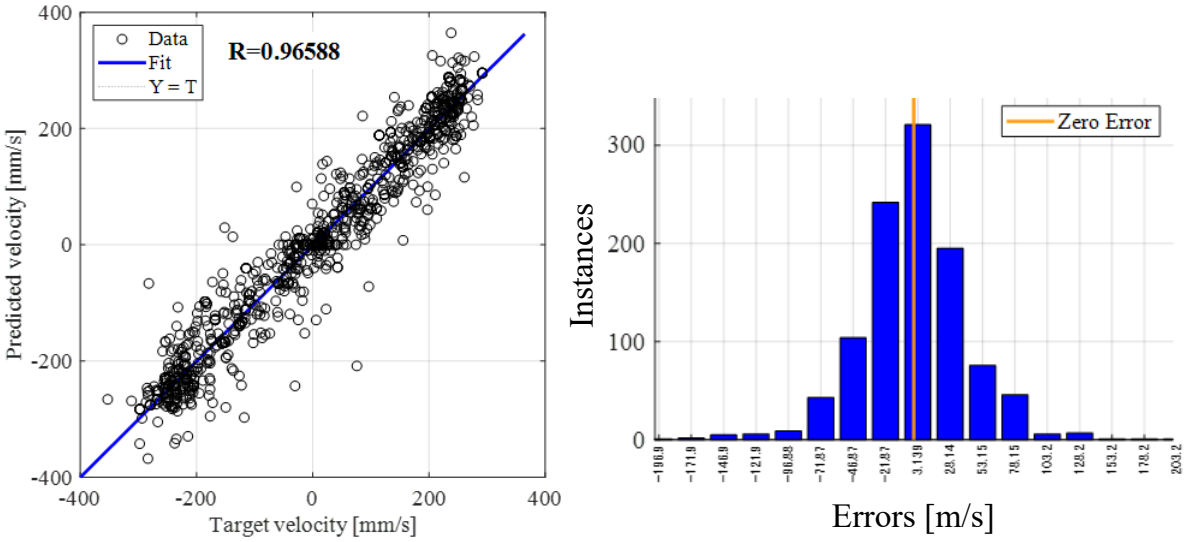

(a) Predictive correlation.

(b) Histogram of prediction error.

Fig. 3-5: Experimental results of TVNN learning.

panel (b) shows the histogram of the prediction error, indicating that the TVNN can estimate velocity with high accuracy.

For the performance evaluation of the proposed TVNN, a sinusoidal input with an amplitude of 6 rad/s and a period of 4 s was given as a motor angular velocity command. In this experiment, the translational velocity, measured by image processing (v^{meas}), was compared with the estimated velocities (v^{est}_{AVE}, v^{est}_{KF}, and v^{est}_{TVNN}), using the three types of sensor configurations and estimation method combinations, shown in Table 3.5. In applying the discrete Kalman filter[86] in Table 3.5, the required measurement

Table 3.5: Types of sensor configurations and estimation method combinations.

Velocity	Sensors configuration	Estimation method
v_{AVE}^{est}	Axle motor encoders	Average crawler velocity
v_{KF}^{est}	Axle motor encoders and accelerometer	Discrete Kalman filter
v_{TVNN}^{est}	Axle motor encoders and accelerometer	TVNN

noise variance and process noise variance matrices were determined according to prior experiments.

Figures 3-6 (a) and (b) show the measured and estimated velocities, along with the errors between each of their values. Table 3.6 summarizes the errors of each velocity estimation when the measured velocity is taken as the true value. Figure 3-6 shows that the velocity amplitude obtained from the axle motor angular velocity was more significant than the measured velocity, especially about the maximum and minimum measured velocities. This result indicates that the translational velocity was smaller than the crawler velocity due to slippage. The velocity estimation performance was improved by integrating the axle velocity and acceleration information with the discrete Kalman filter. However, the errors remained significant in the vicinity of the maximum and minimum velocities. In other words, the effect of slippage was still observed as an error. However, the translational velocity estimated by the TVNN almost followed the measured velocity. The results summarized in Table 3.6 indicate that the TVNN exhibited the highest velocity estimation accuracy among the three methods in this study. The table further shows that the TVNN velocity improved the velocity estimation performance. These results suggest that the TVNN can include the slippage velocity component in its estimate.

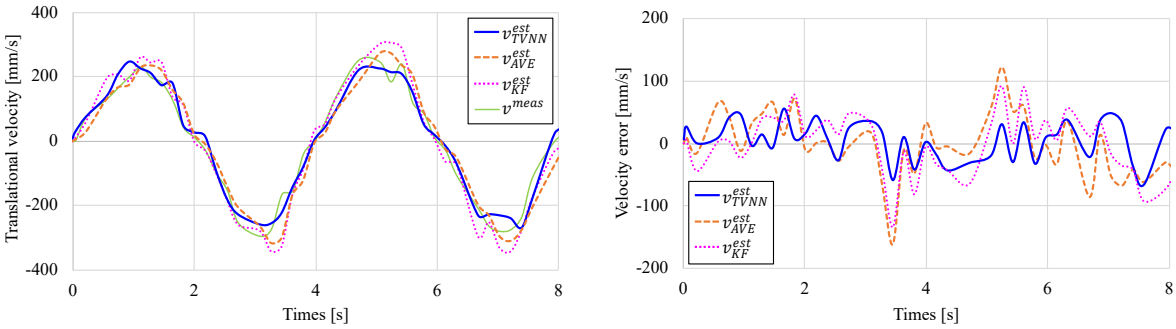

(a) Measured and estimated velocities.

(b) Velocity error.

Fig. 3-6: Experimental results comparing translational velocity estimation methods.

Table 3.6: Performance evaluation results of translational velocity estimation methods.

	v_{AVE}^{est} [mm/s]	v_{KF}^{est} [mm/s]	v_{TVNN}^{est} [mm/s]
Maximum error value	122.6	91.9	52.2
Minimum error value	-161.0	-135.0	-65.8
Standard deviation	51.6	48.7	30.2

(a) Polyurethane rubber.

(b) Fabric material.

(c) Polytetrafluoroethylene (PTFE).

Fig. 3-7: Road surface environments.

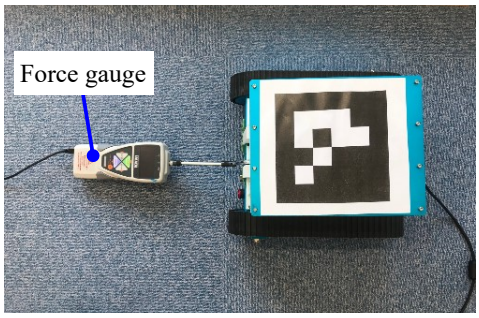

Fig. 3-8: Measurement of friction force.

3.5 Velocity Estimation Performance in Environments that Are Different from Training Environment

One of the characteristics of neural networks, in general, is the correlation between estimation performance and the amount of learning. Particularly, the TVNN treats disturbances, including reaction forces from the environment, as input. Since the friction coefficient of the driving environment is related to the disturbance, the velocity estimation is considered to be affected by the difference in the driving environment from the time of training. Therefore, this section experimentally investigates the effect when the driving environment differs from the training environment.

3.5.1 Environments for Evaluation

Figure 3-7 shows the road surface environments used in the evaluation. In this study, polyurethane rubber and polytetrafluoroethylene (PTFE) were adopted as environments with high and low friction coefficients, respectively. Additionally, an evaluation was conducted on the fabric material of the floor carpet in the experimental environment. As environmental reference information, the friction force of the tracked vehicle was measured with a force gauge (ZTA-500N, IMADA), as shown in Fig. 3-8. Figure 3-9 shows the measured friction force on the tracked vehicle. The friction force increases until the tracked

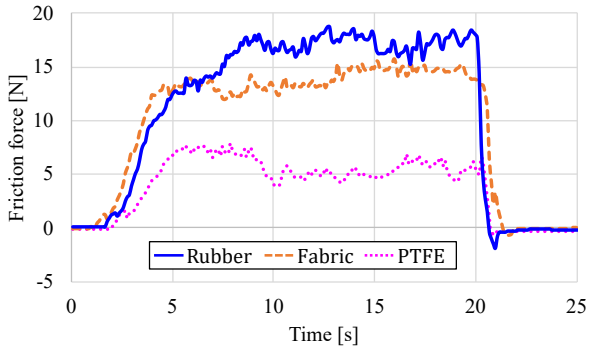

Fig. 3-9: Measured friction force.

Table 3.7: Dynamic friction coefficient for experimental environments.

	Average of friction force [N]	Dynamic friction coefficient [-]
Rubber	17.50	0.36
Fabric	13.88	0.28
PTFE	4.89	0.10

vehicle begins to move, and when the friction force exceeds the maximum static friction force, the vehicle begins to move. Table 3.7 shows the dynamic friction coefficient for each environment obtained from the saturated friction force (average of friction force measured from 10 s to 15 s in Fig. 3-9) and the mass of the vehicle (5kg). Table 3.8 shows the combination of learning and evaluation environments for this evaluation. In Table 3.8, “Rubber&PTFE” is a test course created by laminating sheets made of each material, as shown in Fig. 3-10. In this experiment, the tracked vehicle was controlled to output torque

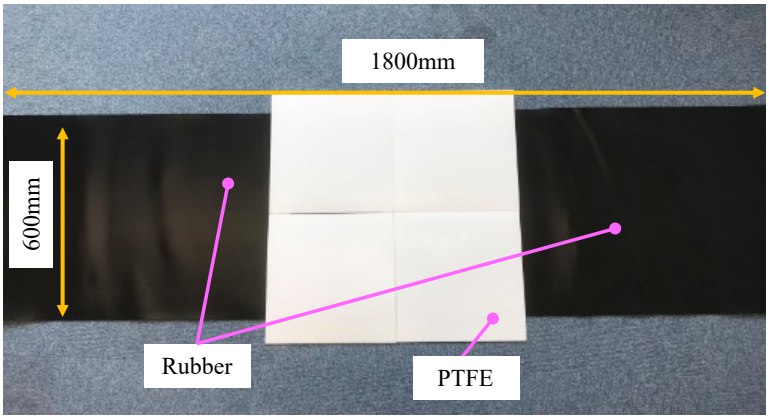

Fig. 3-10: Test course made of rubber and PTFE sheets.

Table 3.8: Combination of learning and evaluation environments.

Case No.	Learning environment	Evaluation environment
case 1	Rubber	Rubber
case 2	Rubber	PTFE
case 3	PTFE	PTFE
case 4	PTFE	Rubber
case 5	Rubber & PTFE	Rubber
case 6	Rubber & PTFE	PTFE
case 7	Rubber & PTFE	Rubber & PTFE
case 8	Fabric	Fabric
case 9	Rubber & PTFE	Fabric

by applying a current to the crawler motor. For the torque commands during training, sinusoidal inputs with amplitude as the rated torque of the crawler motor were applied with frequencies of 0.1, 0.2, 0.25, 0.5, 1, 2, 4, 5, 10, and 20 Hz. During the evaluation, the torque commands were given as sinusoidal inputs with the amplitude set to the rated torque of the crawler motor, and the frequency changed to 0.2, 0.25, 0.5, 1, and 5 Hz.

3.5.2 Velocity Estimation Performance Evaluation for Different Environments

Figure 3-11 shows the results of velocity estimation for each case in Table 3.8. The solid and dotted lines in each panel represent the estimated velocity by the TVNN (v^{est}_{TVNN}) and the measured velocity from the marker recognition position (v^{meas}), respectively. The statistics when the velocity measured from the marker recognition position is taken as the true value are shown in Table 3.9, and the error distribution is shown in Fig. 3-12. In Fig. 3-12, the "X" mark represents the mean value and the "○" mark represents the outlier. Table 3.9 and Fig. 3-12 show significant estimation errors in cases 2, 4, 5, and 6. Figure 3-12 also shows that there are significant outliers in cases 2 and 4. These results suggest that the estimation performance decreases in an environment that is different from the training environment. However, by increasing the amount of prior training, it is expected that a variety of environments can be handled. For example, comparing cases 2 and 6 and cases 4 and 5, it can be confirmed that the estimation performance can be improved by having the TVNN learn in multiple environments. The results of cases 8 and 9 suggest that the TVNN can estimate the velocity on the road surface with an intermediate friction coefficient, which is made of fabric if trained in an environment with high and low

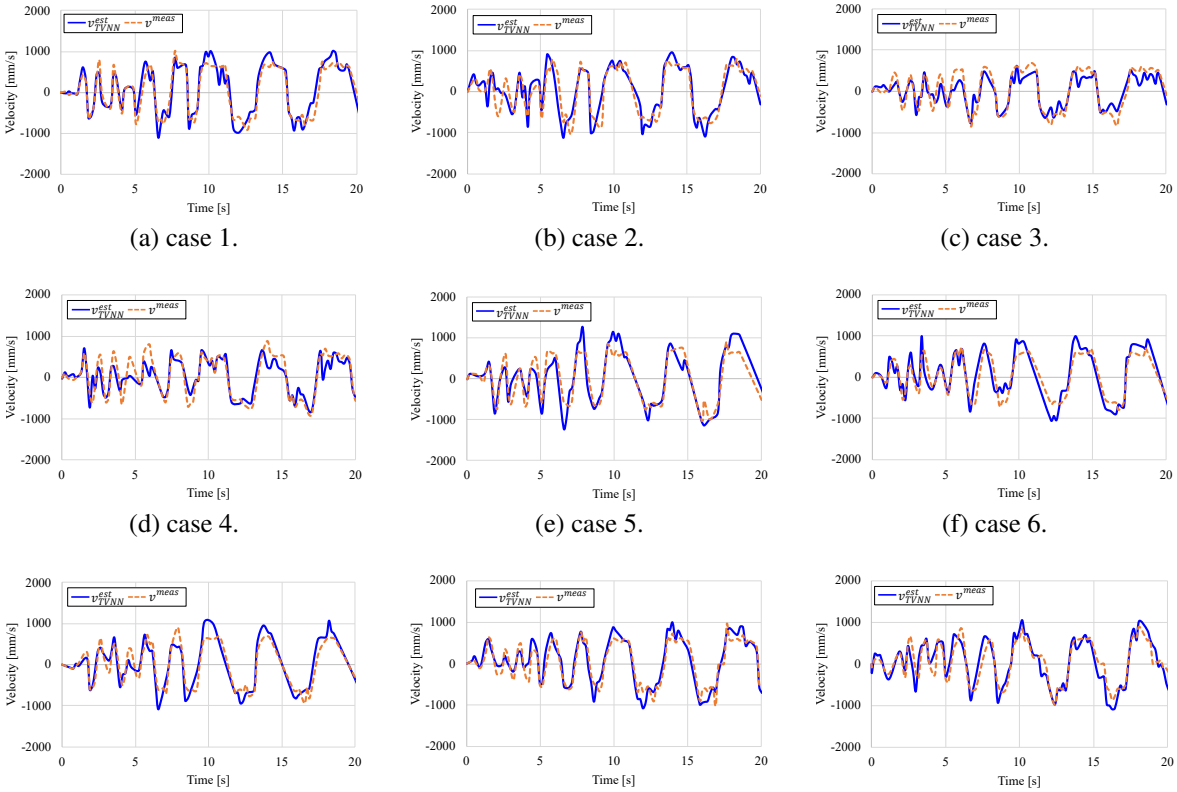

(a) case 1. (b) case 2. (c) case 3.

(d) case 4. (e) case 5. (f) case 6.

(g) case 7. (h) case 8. (i) case 9.

Fig. 3-11: Velocity estimation for each case in Table 3.8.

friction coefficients. These results suggest that by training the TVNN to take a wide range of values for the estimated disturbance as its input, the velocity estimation performance can be ensured even in environments that are different from the training environment.

Table 3.9: Statistics of velocity estimation error.

Case No.	Maximum value [mm/s]	Minimum value [mm/s]	Average [mm/s]	Standard deviation [mm/s]
case 1	483.6	-460.1	31.0	216.2
case 2	726,9	-759.2	-9.7	285.5
case 3	432.5	-505.5	-47.7	204.7
case 4	649.7	-769.3	-33.8	240.3
case 5	610.8	-637.6	6.9	286.9
case 6	585.0	-509.5	28.7	249.2
case 7	414.4	-482.5	-6.8	220.5
case 8	466.5	-435.3	15.4	202.8
case 9	559.9	-492.7	-12.4	231.1

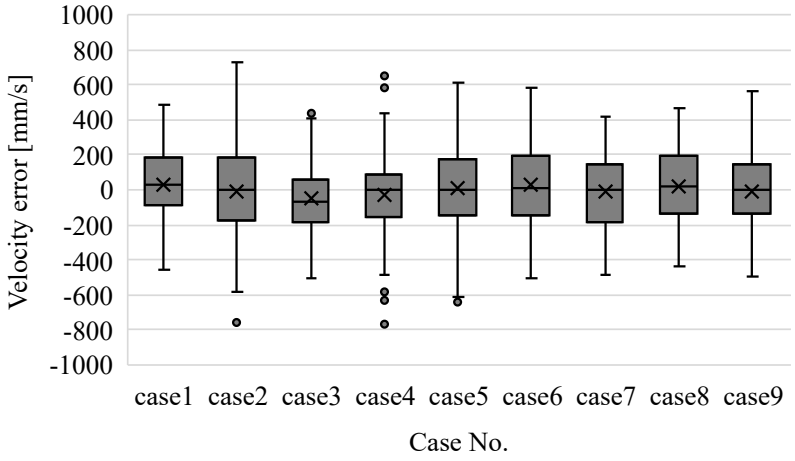

Fig. 3-12: Velocity estimation error distribution.

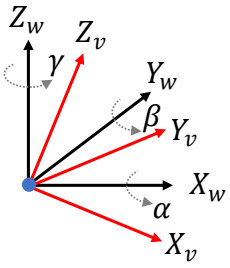

Fig. 3-13: Definition of rotation angle in coordinate transformation from world coordinates to vehicle coordinates.

3.6 Improvement of Velocity Estimation Performance by Gravity Compensation

The tracked vehicle can be considered to move in three-dimensional space on unstable terrain or slopes by taking advantage of its high traveling ability. In contrast, the proposed TVNN uses two-dimensional information measured by external sensors, such as cameras, for training. Therefore, to estimate the velocity of crawlers running in three-dimensional space using the TVNN, it is necessary to estimate the velocity considering the attitude of the tracked vehicle. The TVNN uses the translational acceleration measured by the accelerometer as one of its inputs. When the tracked vehicle runs three-dimensionally, the value measured by the acceleration sensor is mixed with the gravitational acceleration, which changes according to the vehicle's posture. Therefore, by compensating the acceleration sensor value with gravity before inputting to the TVNN, the velocity estimation performance during slope running can be improved. In this section, the velocity estimation performance during slope running is evaluated by gravity compensation.

3.6.1 Gravity Compensation of Acceleration

Acceleration is compensated by using a coordinate transformation between the world and the vehicle coordinates. The gravitational component is removed by transforming the vehicle coordinates where the accelerometer is mounted to the world coordinates. As shown in Fig. 3-13, consider the case where the accelerometer mounted on the vehicle is inclined by α on the X_w axis, β on the Y_w axis, and γ on the Z_w axis for the world coordinates. The rotation matrix ${}^{w}\boldsymbol{R_v}$ represents this rotation in the following

equation:

$$\begin{aligned} {}^{w}\boldsymbol{R}_{v} &= {}^{w}\boldsymbol{R}_{vx}{}^{w}\boldsymbol{R}_{vy}{}^{w}\boldsymbol{R}_{vz} \\ &= \begin{bmatrix} \cos\beta\cos\gamma & -\cos\beta\sin\gamma & \sin\beta \\ \cos\alpha\sin\gamma+\sin\alpha\sin\beta\cos\gamma & \cos\alpha\cos\gamma-\sin\alpha\sin\beta\sin\gamma & -\sin\alpha\cos\beta \\ \sin\alpha\sin\gamma-\cos\alpha\sin\beta\cos\gamma & \sin\alpha\cos\gamma+\cos\alpha\sin\beta\sin\gamma & \cos\alpha\cos\beta \end{bmatrix}, \end{aligned} \tag{3.16}$$

where ${}^{w}\boldsymbol{R}_{vx}$, ${}^{w}\boldsymbol{R}_{vy}$, and ${}^{w}\boldsymbol{R}_{vz}$ are rotation matrices around the X_w, Y_w, and Z_w axes, respectively, given by:

$${}^{w}\boldsymbol{R}_{vx} = \begin{bmatrix} 1 & 0 & 0 \\ 0 & \cos\alpha & -\sin\alpha \\ 0 & \sin\alpha & \cos\alpha \end{bmatrix}, \tag{3.17}$$

$${}^{w}\boldsymbol{R}_{vy} = \begin{bmatrix} \cos\beta & 0 & \sin\beta \\ 0 & 1 & 0 \\ -\sin\beta & 0 & \cos\beta \end{bmatrix} \tag{3.18}$$

$${}^{w}\boldsymbol{R}_{vz} = \begin{bmatrix} \cos\gamma & -\sin\gamma & 0 \\ \sin\gamma & \cos\gamma & 0 \\ 0 & 0 & 1 \end{bmatrix}. \tag{3.19}$$

When the acceleration vector in the world coordinates and the acceleration vector in the vehicle coordinates are defined as $\boldsymbol{a_w} = [a_{wx}, a_{wy}, a_{wz}]^T$ and $\boldsymbol{a_v} = [a_{vx}, a_{vy}, a_{vz}]^T$, respectively, the acceleration vector in the world coordinates ($\boldsymbol{a_w}$) is obtained as follows:

$$\boldsymbol{a_w} = {}^{w}\boldsymbol{R}_{v}^{-1}\boldsymbol{a_w}. \tag{3.20}$$

Here, the acceleration vector in the vehicle coordinates ($\boldsymbol{a_v}$) is measured using an accelerometer. When the gravity vector is defined as $\boldsymbol{a_g} = [0, 0, -g]^T$, the acceleration vector after gravity compensation ($\boldsymbol{a_w^{cmp}}$) is as follows:

$$\boldsymbol{a_w^{cmp}} = \boldsymbol{a_w} - \boldsymbol{a_g} \tag{3.21}$$

The acceleration vector in the vehicle coordinates is obtained as follows:

$$\boldsymbol{a_v^{cmp}} = {}^{w}\boldsymbol{R}_{v}\boldsymbol{a_w^{cmp}} \tag{3.22}$$

The X_v component of this acceleration vector after gravity compensation, the component fixed to the translational direction of the vehicle, is used as the input for the TVNN.

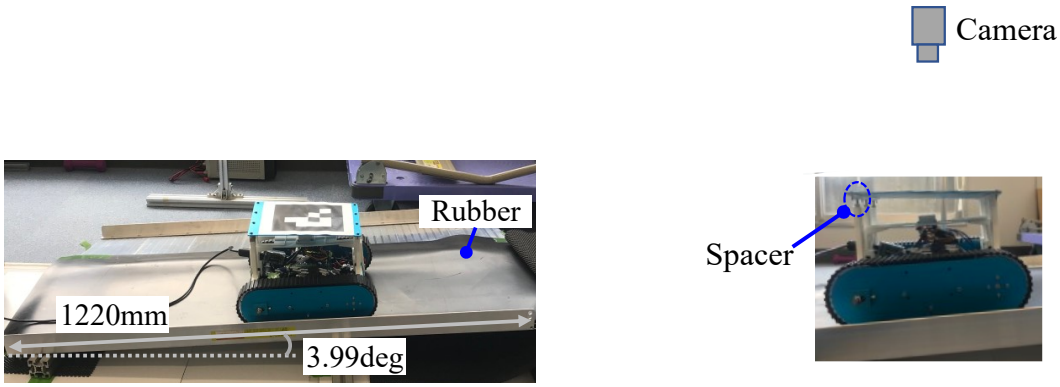

(a) Slope.

(b) Tracked vehicle.

Fig. 3-14: Evaluation environment for velocity estimation performance of TVNN with gravity compensation.

3.6.2 Environment for Evaluating Velocity Estimation Performance, including Gravity Compensation

The effect of gravity compensation on improving the velocity estimation performance is verified during slope driving shown in Fig. 3-14. For the evaluation, the camera above the vehicle and the AR marker are adjusted to be parallel using spacers. The camera detects the position of the AR marker. The road surface was inclined by approximately 4 degrees, and the robot moved on urethane rubber. The TVNN was trained beforehand on a urethane rubber laid on a flat surface. The training and evaluation of the TVNN were conducted in the same manner as described in Section 3.5.1. The tracked vehicle equipped with the trained TVNN was driven on a slope to investigate the effect of gravity compensation.

3.6.3 Evaluation Results of the Effects of Gravity Compensation

Figure 3-15 shows the acceleration in each direction. From Fig. 3-15, it can be seen that the acceleration in the Z_v direction, in particular, remains near zero, indicating that compensation has been achieved. Additionally, the effect of gravity in the X_v and Y_v directions is compensated.

Figure 3-16 shows the velocity measured from the AR marker and the estimated velocity by the TVNN with and without gravity compensation. In the figure, panels (a) and (b) show the velocity and error when the velocity measured from the AR marker is taken as the true value, respectively. From Fig. 3-16, it can be seen that gravity compensation reduces the error from the true value and improves performance. These results suggest that the acceleration after gravity compensation can be used as an input for the

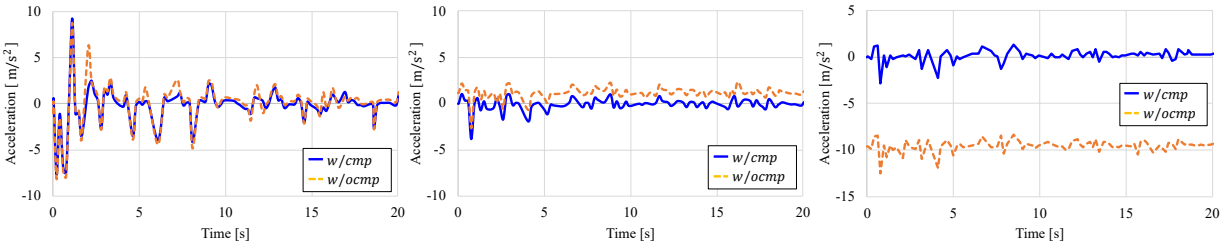

(a) X_v acceleration. (b) Y_v acceleration. (c) Z_v acceleration.

Fig. 3-15: Gravity compensation effect of acceleration in vehicle coordinates.

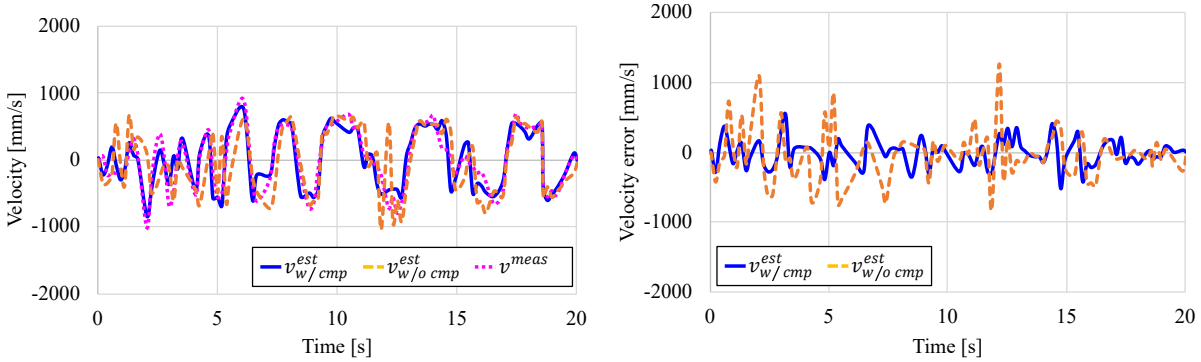

(a) Velocity. (b) Velocity error.

Fig. 3-16: Gravity compensation effect on velocity estimation by TVNN.

TVNN, which can be applied to slopes.

Table 3.10: Configurations of the TVNN.

Configuration No.	Inputs	Number of neurons
configuration 1	Motor velocities	25
	Translational acceleration	
configuration 2	Motor velocities	15
	Translational acceleration	
	Motor disturbances	

3.7 Discussion

In this study, the estimated disturbance of the crawler motor is used as one of the inputs to the TVNN. Since the estimated disturbance includes the driving force converted into motor torque, it includes the information of the driving environment such as slippage. This means that the estimated disturbance provides environmental information to the TVNN. By learning the environmental information, the TVNN can ensure robustness against environmental changes. Therefore, this section discusses the robustness of the velocity estimation performance to environmental changes by using estimated disturbances. In this study, the configuration of TVNN was set up as shown in configurations in Table 3.10. The configuration 1 has fewer inputs than the configuration 2 because it does not use the estimated disturbances as inputs. To ensure fairness in the evaluation, the configuration 1 has a large number of neurons. Using the same evaluation environment as shown in Section 3.5.1, the velocity estimation performance against the environment was experimentally evaluated. The combination of learning and evaluation environments in the evaluation is shown in Table 3.11. In the evaluation, the experimental data of the cases 1, 2, 6, 8, and 9 in Section 3.5.2 were used as input for the TVNN of each configuration. The TVNNs of the configurations. 1 and 2 were trained using the information obtained by applying current to the crawler motor and controlling the output torque as shown in Section 3.5.2.

Figure 3-17 shows the error distribution of the estimated velocity by the TVNN from the measured velocity by the AR marker. In Fig. 3-17 , the “X” mark represents the mean value and the “○” mark represents the outlier. First, comparing cases 1-1 and 1-2, when the training and evaluation environments are the same, no significant difference in velocity estimation performance was observed because of the difference in configuration. However, when comparing cases 2-1 and 2-2, configuration 1 (case 2-1) has a larger range of velocity estimation errors and more outliers than configution 2 (case 2-2). This suggests that the use of estimated disturbances has some effect on the environmental changes from the

Table 3.11: Combination of learning and evaluation environments and configurations.

Case No.	Configuration No.	Learning environment	Evaluation environment
case 1-1	1	Rubber	Rubber
case 2-1	1	Rubber	PTFE
case 6-1	1	Rubber & PTFE	PTFE
case 8-1	1	Fabric	Fabric
case 9-1	1	Rubber & PTFE	Fabric
case 1-2	2	Rubber	Rubber
case 2-2	2	Rubber	PTFE
case 6-2	2	Rubber & PTFE	PTFE
case 8-2	2	Fabric	Fabric
case 9-2	2	Rubber & PTFE	Fabric

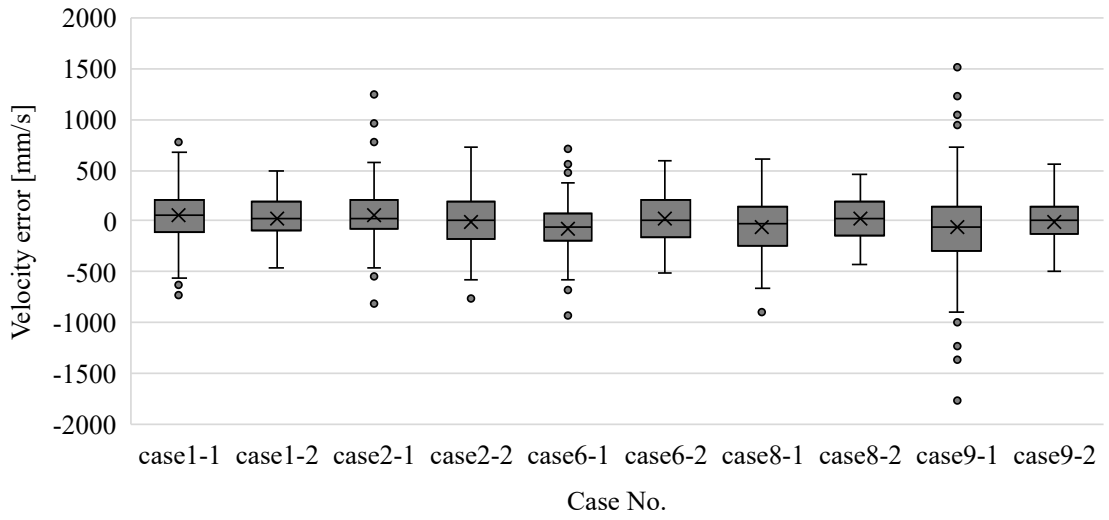

Fig. 3-17: Velocity estimation error distribution.

training. It was also confirmed from cases 6-1 and 6-2 that the velocity estimation performances of both configurations were improved by increasing the number of training environments. As mentioned in Section 3.5.2, the results of cases 8-2 and 9-2 suggest that the TVNN can estimate the velocity even in environments with intermediate friction coefficients when trained in environments with high and low friction coefficients. However, comparing cases 8-1 and 9-1, it was found that the lack of use of estimated disturbances did not ensure estimation performance for environments with intermediate friction coefficients. These results confirm that the use of estimated disturbances as input to the neural network contributes to improved robustness against environmental changes from the training.

3.8 Summary

This chapter proposed a method for estimating the velocity of a tracked vehicle, including slippage. In the proposed method, a neural network was constructed to estimate the translational velocity. The input to this neural network (TVNN) includes a disturbance of the motor. A comparison with general mobile robot velocity estimation methods demonstrated the effectiveness of the proposed method. Additionally, the performance of the velocity estimation was compared and verified when running in an environment that was different from the training environment. As a result, the applicability of the proposed method to various environments was confirmed by increasing the amount of prior learning. Additionally, using gravity-compensated acceleration as an input to the TVNN when driving on a slope, a method to improve the velocity estimation performance was proposed, and experiments demonstrated its effectiveness.

In this chapter, the discussion was based on a tracked vehicle, which is prone to slippage, unlike general mobile robots; however, the proposed method is also applicable to general mobile robots. Although the proposed velocity estimation method requires prior learning, the performance can be ensured by evaluating the method on a representative road surface considering the possible range of the estimated disturbance. Furthermore, to apply the proposed velocity estimation method to three-dimensional driving, an approach in which the preprocessed acceleration was given as input is used, and its effectiveness was confirmed. Finally, it was experimentally confirmed that using the estimated disturbance as an input to the TVNN gives the velocity estimation robustness to environmental changes.

Chapter 4

Motion Control Based on Driving Force

4.1 Introduction

This chapter proposes motion control of a moving mechanism based on appropriate suppression of slippage by controlling the driving force. As discussed in Chapter 3, a tracked vehicle, unlike a car, always experiences slippage and is challenging to model. This chapter proposes a method for controlling the tracked vehicle using driving force.

A tracked vehicle can traverse diverse terrains because its crawlers ensure ground contact while traveling. However, two significant disturbances during motion control of tracked vehicles hinder precise movement: (1) complex slippage of the crawler on the ground and (2) nonholonomic constraints of vehicle motion. Therefore, tracked vehicle motion control must consider slippage and nonholonomic constraints to ensure precise position control.

Several methods have been proposed to handle slippage, such as backstepping[36], sliding mode control[37], model predictive control[38], observer-based robust control[39], and trajectory planning[41]. These methods are designed to ensure that the system is robust against slippage, but do not suppress slippage. Slippage is related to the friction force between the crawler and ground surface[42], corresponding to the crawler's driving force. Accordingly, slippage can be suppressed by controlling the driving force. Although driving force control for automobiles has been investigated[44][46], few studies have considered tracked vehicles. The driving force was estimated using observers based on the axle velocity[46], with the effect of slippage being neglected. Additionally, during tracked vehicle control using driving force feedback, the crawlers' driving forces interfere with each other. Therefore, driving force distribu-

tion must be considered that decouples driving forces. Decoupled driving forces provide the necessary moment for turning, but slippage can be induced in the turning direction. Although this slippage facilitates lateral movement of the tracked vehicle, it interferes with motion control, such as positioning. Additionally, a nonholonomic constraint is established in typical mobile robots to nullify commands in the lateral direction. Recently, the effectiveness of position control, including a compensator for the effects of nonholonomic constraints, was demonstrated for a wheeled mobile robot[87]. For a tracked vehicle, an improvement in position control can be expected by suppressing the disturbance caused by the nonholonomic constraints while allowing adequate slippage.

This chapter estimates the driving force based on estimating the vehicle velocity, including slippage, using a disturbance observer and machine learning, discussed in Chapter 3. Then, a driving control system is proposed for a tracked vehicle that is based on driving force. First, an observer is designed to estimate the driving force of the track using the estimated translational velocity of the vehicle. Using driving force feedback, a driving control system that suppresses slippage in the translational direction is achieved. However, when turning occurs while controlling the driving force, the interference between the crawlers' driving forces prevents motion. Therefore, a driving force distribution is introduced that induces slippage in the turning direction by decoupling the driving forces. The distribution is designed using the instantaneous center of the vehicle. The lateral disturbance of the tracked vehicle, including the skidding and nonholonomic constraints, is defined as the equivalent lateral disturbance. The equivalent lateral disturbance is estimated by a workspace observer [52], coordinate transformation, and selection matrix. Moreover, a virtual turning velocity reference is derived from the equivalent lateral disturbance and vehicle velocity. Hence, virtual turning velocity control is proposed to suppress the equivalent lateral disturbance by ensuring that the actual turning velocity follows the virtual turning velocity reference. A position controller is integrated with a virtual turning velocity controller in the acceleration dimension. The resulting control system ensures high-performance position tracking by suppressing the lateral disturbance while allowing the tracked vehicle to slip appropriately. Experiments demonstrate the slip suppression performance by driving force control, the turning performance by driving force distribution, and the positioning performance by virtual turning control of the tracked vehicle.

This chapter is organized as follows: Section 4.2 describes the driving force observer and driving control that feeds back the driving force to suppress slippage in the translational direction. Section 4.3 describes the driving force distribution for the turning motion. Section 4.4 describes the virtual turning velocity control for suppressing the lateral disturbance, including the slippage generated by the dis-

tributed driving force. In Section 4.5, the stability of the proposed position control system is discussed based on passivity. This chapter is summarized in Section 4.6.

4.2 Driving Control to Suppress Slippage in Translational Direction

4.2.1 Driving Force Observer

The trained translational velocity estimation neural network (TVNN) estimates translational velocity $\hat{v}_x$. By substituting $\hat{v}_x$ and turning velocity $\dot{\phi}$, measured using a gyroscope, into the inverse kinematics, the estimated crawler velocity $\hat{v}_i$ is obtained as follows:

$$\hat{v}_i = \begin{cases} \hat{v}_x + \dfrac{W}{2}\dot{\phi} & (i = r) \\ \hat{v}_x - \dfrac{W}{2}\dot{\phi} & (i = l). \end{cases} \tag{4.1}$$

Here, the crawler velocity in the translational direction is estimated by considering slippage in the turning direction. The driving force observer (DFOB) was designed to estimate the driving force from the estimated crawler velocity. A block diagram of the DFOB is shown in Fig. 4-1. The driving force estimated by the DFOB is given by

$$\hat{f}^{dr}_{x,i} = \frac{g_{df}}{s + g_{df}}(f^{ref}_{x,i} - sJ_{mn}\frac{\hat{v}_i}{R^2}), \tag{4.2}$$

where J_{mn} and g_{df} are the nominal motor-shaft conversion moment of inertia J_m and DFOB cutoff frequency, respectively. The DFOB provides the driving force as a low-pass filtered value of the driving force calculated using (4.2). The driving force required for motion can be generated via feedback control of the estimated driving force, and slippage in the translational direction of the crawler can be suppressed.

4.2.2 Control System with Driving Force Feedback

Figure 4-8 shows a control system that suppresses the slippage of the tracked vehicle by controlling the estimated driving force. The proposed system consists of two closed-loop controls: an outer velocity loop and internal driving force control. These controllers are set in a cascade, where the output of the velocity controller manipulates the set-point of the driving force controller. In the velocity control loop,

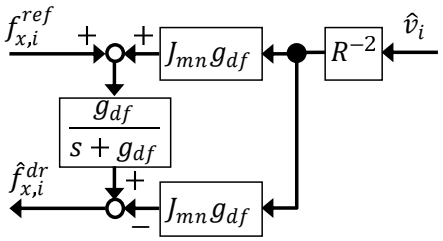

Fig. 4-1: Block diagram of the DFOB.

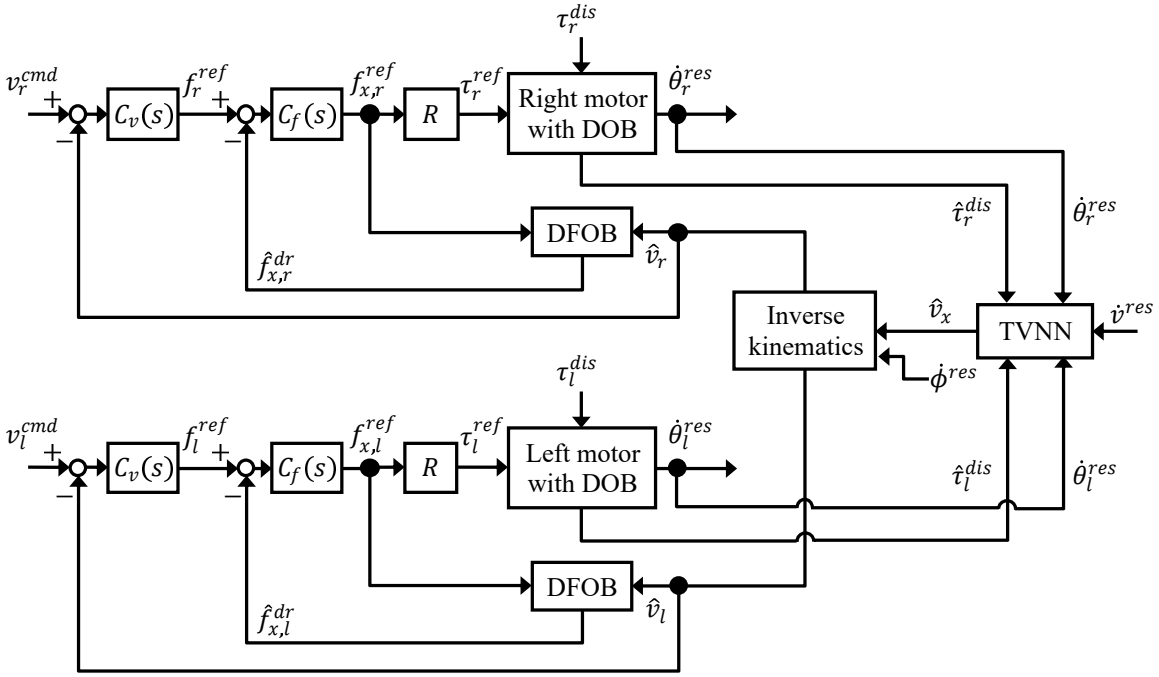

Fig. 4-2: Control system of tracked vehicle using estimated driving force.

the driving force reference f_i^{ref} for each track is determined by the velocity command v_i^{cmd} and the estimated track velocity $\hat{v}_i$ as follows:

$$f_i^{ref} = C_v(s)(v_i^{cmd} - \hat{v}_i), \tag{4.3}$$

where $C_v(s)$ represents a velocity controller that is physically equivalent to impedance.

In the driving force control loop, the driving force estimated by the DFOB is controlled to follow the driving force reference. The motor torque reference τ_i^{ref} is calculated as follows:

$$\tau_i^{ref} = \frac{1}{R} C_f(s)(f_i^{ref} - \hat{f}_{x,i}^{dr}), \tag{4.4}$$

where $C_f(s)$ represents a force controller. The proposed control system controls the driving force required for the crawler movement to ensure that the intended crawler velocity can be achieved regardless of the slip conditions.

4.2.3 Experiments on Suppression of Translational Slippage by Driving Force Control

Experiments were conducted to evaluate the slip suppression performance by driving force control. The TVNN was trained using the experimental setup shown in Fig. 3-3. The regression function gener-

Table 4.1: Experimental conditions in slip suppression.

Case no.	Velocity estimation	Driving force feedback
case 1	Calculated by motor encoder	Disable
case 2	Calculated by motor encoder	Enable
case 3	Estimated by TVNN and inverse kinematics	Disable
case 4	Estimated by TVNN and inverse kinematics	Enable

Table 4.2: Control parameters in slip suppression experiment.

Parameter	Value
Crawler velocity control P gain	0.1
Driving force control P gain	0.2
Driving force control I gain	500
Cutoff freq. of DOB g_d	188.4 rad/s
Cutoff freq. of DFOB g_{df}	188.4 rad/s

ated by the trained TVNN was incorporated into the tracked vehicle program in the C language. In this experiment, the experimental conditions were set as shown in Table 4.1. In cases 1 and 2 of Table 4.1, the motor angular velocity obtained from the crawler axle encoder multiplied by the sprocket radius ($R\dot{\theta}_i^{res}$) is used as the input to the DFOB ($\hat{v}_i$). The velocity command value v_i^{cmd} was obtained as a sine wave with an amplitude of 0.3 m/s and a period of 6.0 s. Table 4.2 shows the control parameters in this experiment.

Figures 4-3∼4-6 show the experimental results for each case. In each figure, (a) and (b) show the estimated crawler velocity and slip ratio, respectively. Here, the slip ratio was calculated by substituting the velocity response calculated from the AR marker position and the motor angular velocity response into (3.8). From Fig. 4-3 (a) and Fig. 4-5 (a), it is observed that the ability of the velocity response to follow the velocity command deteriorates near the inflection point of the velocity command when the driving force control is not implemented. This is because the absolute value of the driving force reference to the crawler is maximized at the inflection point of the velocity command; however, it is considered that the ability to follow the velocity command deteriorates because of slippage. Conversely, from Fig. 4-4 (a) and Fig. 4-6 (a), it is observed that in case 2, the velocity follows even at the inflection point. It was confirmed that the driving force control improved the velocity's ability to follow the command. Next, when Fig. 4-3 (b) and Fig. 4-4 (b), or Fig. 4-5 (b) and Fig. 4-6 (b) are compared, the slip ratio changes

momentarily without the driving force control, whereas with the driving force control, the slip ratio is generally low. This result suggests that the driving force control suppresses slippage. Additionally, when Fig. 4-4 (b) and Fig. 4-6 (b) are compared, as in case 2, the slippage rate suddenly changed, while in case 4, the slippage rate remained low across the board. This confirms that estimating the velocity of the vehicle body and using it for driving force control can have a higher slip suppression effect. From the results described above, the effectiveness of the proposed control system for a tracked vehicle was confirmed.

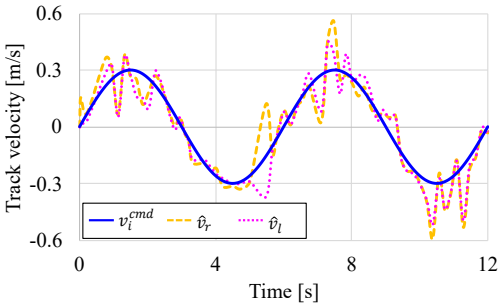

(a) Velocity control performance.

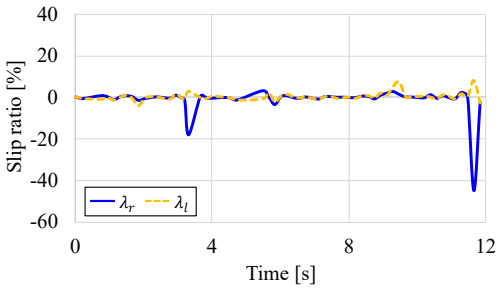

(b) Slip ratio.

Fig. 4-3: Experimental results of case 1.

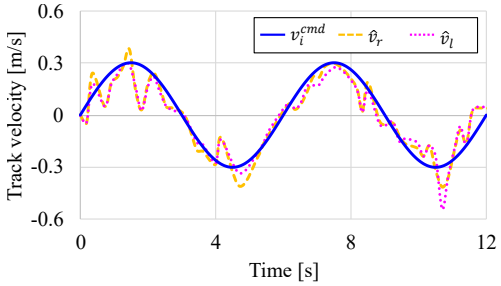

(a) Velocity control performance.

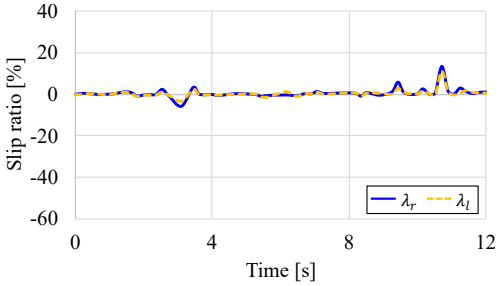

(b) Slip ratio.

Fig. 4-4: Experimental results of case 2.

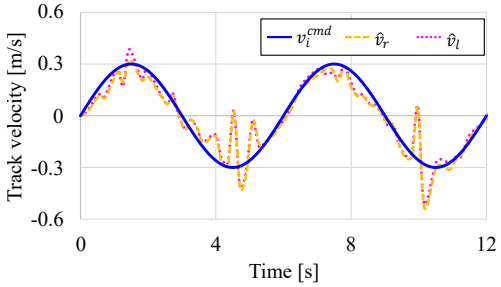

(a) Velocity control performance.

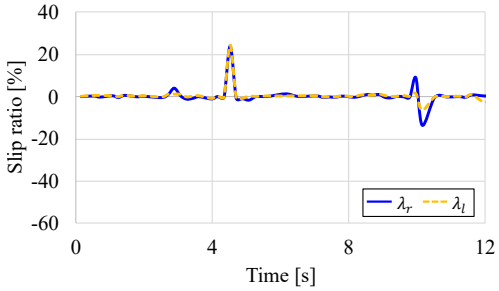

(b) Slip ratio.

Fig. 4-5: Experimental results of case 3.

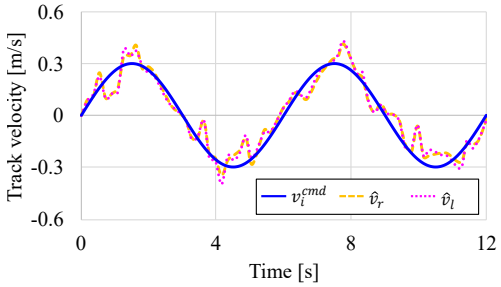

(a) Velocity control performance.

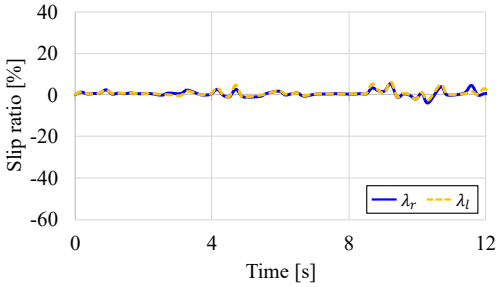

(b) Slip ratio.

Fig. 4-6: Experimental results of case 4.

4.3 Driving Force Distribution for Turning Motion

When controlling the vehicle's turning and driving force simultaneously, generating the moment necessary for turning is difficult because the right and left driving forces interfere with each other. Thus, the driving force is distributed based on the inverse kinematics solution using a weighted pseudoinverse matrix. For a typical two-wheeled mobile robot, the Jacobian matrix $\boldsymbol{J}$, which determines the relationship between the motor velocities $(\dot{\theta}_r,\ \dot{\theta}_l)$ and vehicle velocities $(v_x,\ \dot{\phi})$, becomes the following square matrix:

$$\begin{bmatrix} v_x \\ \dot{\phi} \end{bmatrix} = \boldsymbol{J} \begin{bmatrix} \dot{\theta}_r \\ \dot{\theta}_l \end{bmatrix}, \tag{4.5}$$

$$\boldsymbol{J} = \begin{bmatrix} \frac{R}{2} & \frac{R}{2} \\ \frac{R}{W} & -\frac{R}{W} \end{bmatrix}. \tag{4.6}$$

By differentiating both sides of (4.5), the relationship between the motor accelerations $(\ddot{\theta}_r,\ \ddot{\theta}_l)$ and vehicle acceleration $(\dot{v}_x,\ \ddot{\phi})$ can be obtained. When the total driving force is calculated from the vehicle accelerations, the inverse Jacobian matrix $\boldsymbol{J^{-1}}$ evenly distributes the driving forces among the crawlers evenly. Therefore, to design the distribution, a weight matrix is introduced as follows:

$$\boldsymbol{w} = \mathrm{diag} \begin{bmatrix} w_r & w_l \end{bmatrix}, \tag{4.7}$$

where w_r and w_l represent the equivalent inertia of the right and left crawlers, respectively. With the weight matrix, the relationship between the distributed driving force and vehicle acceleration can be obtained as follows:

$$\begin{bmatrix} f_{x,r}^{dr} \\ f_{x,l}^{dr} \end{bmatrix} = \frac{1}{R} \boldsymbol{w} \boldsymbol{J}^{-1} \begin{bmatrix} \dot{v}_x \\ \ddot{\phi} \end{bmatrix}, \tag{4.8}$$

Therefore, by designing the weight matrix, the driving force reference of the crawler can be determined, and the force is distributed from the acceleration reference generated by the position controller.

The design of the weight matrix involves the instantaneous turning center of the vehicle, as shown in Fig. 4-7. A line parallel to the Y_v axis drawn on the tracked vehicle from the center of rotation is defined as a non-slip line[90]. The instantaneous turning center is defined as a point on the non-slip line, and the velocity along the X_v axis at this point is the average of the crawler velocities. The position of the

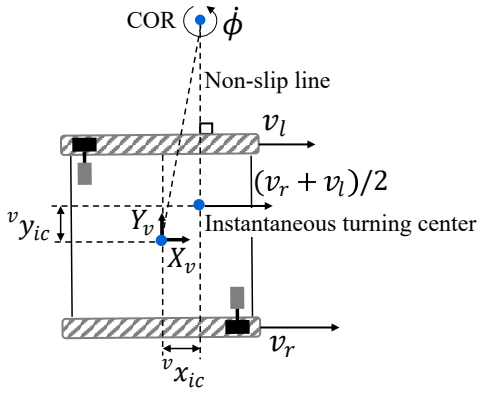

Fig. 4-7: Instantaneous turning center (COR, center of rotation).

instantaneous turning center in the vehicle coordinates $({}^v x_{ic}, {}^v y_{ic})$ is

$$ {}^v x_{ic} = -\frac{v_y}{\dot{\phi}}, \tag{4.9} $$

$$ {}^v y_{ic} = \frac{v_x}{\dot{\phi}} - \frac{v_r + v_l}{2\dot{\phi}}. \tag{4.10} $$

The equation of motion in the rotational direction at the instantaneous turning center can be expressed as follows:

$$ J'_v \ddot{\phi} = \left(\frac{W}{2} + {}^v y_{ic} \right) f^{dr}_{x,r} - \left(\frac{W}{2} - {}^v y_{ic} \right) f^{dr}_{x,l} - f_y \, {}^v x_{ic}, \tag{4.11} $$

$$ J'_v = J_v + \delta J_v, \tag{4.12} $$

$$ \delta J_v = m({}^v x_{ic}^2 + {}^v y_{ic}^2). \tag{4.13} $$

From (3.9), (4.11), and (4.12), the distributed driving force necessary for motion is given by

$$ \begin{bmatrix} f^{dr}_{x,r} \\ f^{dr}_{x,l} \end{bmatrix} = \begin{bmatrix} m(\frac{1}{2} - \frac{{}^v y_{ic}}{W}) & \frac{J_v}{W} \\ m(\frac{1}{2} + \frac{{}^v y_{ic}}{W}) & -\frac{J_v}{W} \end{bmatrix} \begin{bmatrix} \dot{v} \\ \ddot{\phi} \end{bmatrix} + \begin{bmatrix} \frac{\delta J_v \ddot{\phi} + {}^v x_{ic} f_y}{W} \\ -\frac{\delta J_v \ddot{\phi} + {}^v x_{ic} f_y}{W} \end{bmatrix}. \tag{4.14} $$

From (4.14), if the instantaneous turning center does not deviate from the vehicle center in the lateral direction (${}^v y_{ic} = 0$), the driving force should be equally distributed among the crawlers. Otherwise (${}^v y_{ic} \neq 0$), the deviation is represented by the weight of the crawler's driving forces. Thus, the elements of the weight matrix are designed as follows:

$$ w_r = m \left(\frac{1}{2} - \frac{{}^v y_{ic}}{W} \right), \ (0 \leq w_r \leq 1), \tag{4.15} $$

$$ w_l = m \left(\frac{1}{2} + \frac{{}^v y_{ic}}{W} \right), \ (0 \leq w_l \leq 1). \tag{4.16} $$

The second term on the right-hand side of (4.14) indicates the disturbance in the world coordinates, compensated by the workspace observer, as detailed in Section 4.4.

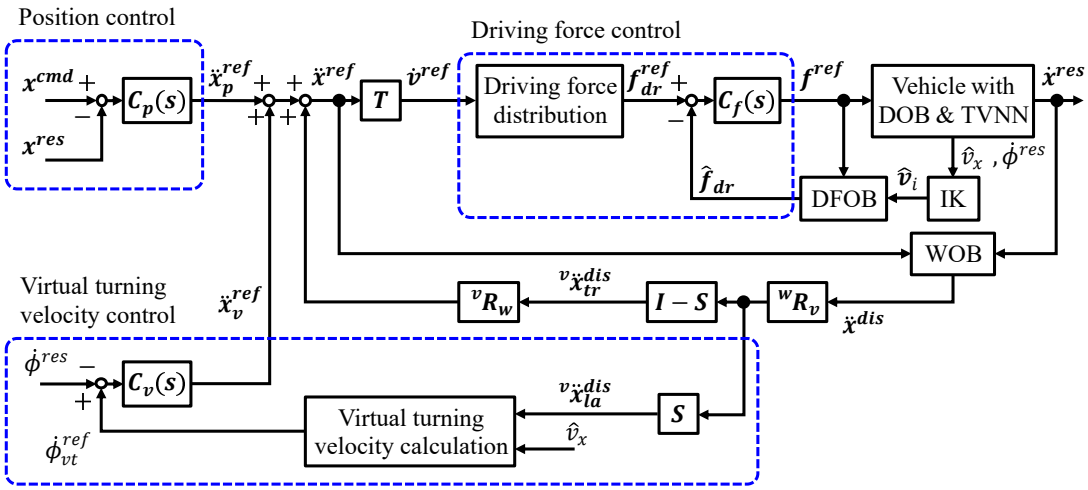

Fig. 4-8: Structure of the proposed motion control system (IK, Inverse Kinematics).

4.4 Motion Control by Driving Force Distribution and Lateral Disturbance Suppression

4.4.1 Control Scheme

In this study, the motion control system of a tracked vehicle is designed to achieve the intended motion and ensure robustness against disturbances. The proposed system is shown in Fig. 4-8. In the figure, the acceleration reference vector in the vehicle coordinates ($\dot{\boldsymbol{v}}$), estimated crawler driving force vector ($\hat{\boldsymbol{f}}_{\boldsymbol{dr}}$), estimated crawler velocity vector ($\hat{\boldsymbol{v}}_i$), and crawler motor force vector ($\boldsymbol{f}$) are defined as follows: $\dot{\boldsymbol{v}} = \begin{bmatrix} \dot{v}_x & \ddot{\phi} \end{bmatrix}^T$, $\hat{\boldsymbol{f}}_{\boldsymbol{dr}} = \begin{bmatrix} \hat{f}^{dr}_{x,r} & \hat{f}^{dr}_{x,l} \end{bmatrix}^T$, $\boldsymbol{v}_i = \begin{bmatrix} \hat{v}_r & \hat{v}_l \end{bmatrix}^T$, $\boldsymbol{f} = \begin{bmatrix} f_{x,r} & f_{x,l} \end{bmatrix}^T$. The superscripts cmd, res, ref, and dis represent a command, response, reference, and disturbance, respectively. The matrices ${}^{w}\boldsymbol{R}_{\boldsymbol{v}}$, ${}^{v}\boldsymbol{R}_{\boldsymbol{w}}$, $\boldsymbol{S}$, and $\boldsymbol{T}$ represent the transformation matrices from Σ_w to Σ_v and from Σ_v to Σ_w, the selection matrix, and the command conversion matrix, respectively. The control system comprises a position controller $\boldsymbol{C_p}(\boldsymbol{s})$, driving force controller $\boldsymbol{C_f}(\boldsymbol{s})$, and virtual turning velocity controller $\boldsymbol{C_v}(\boldsymbol{s})$. In the control system, the position $\boldsymbol{x^{res}}$ follows a command $\boldsymbol{x^{cmd}}$ in the world coordinates. To construct the motion control system with robustness against disturbances to the tracked vehicle, a disturbance observer (DOB) and a workspace observer (WOB)[91] are adopted. The WOB is also used to estimate the lateral disturbance, which is equivalent to the effects of skidding and nonholonomic constraints. We define this disturbance as the equivalent lateral disturbance. Based on the relation between the equivalent lateral disturbance and translational velocity, a virtual turning reference is determined to control the

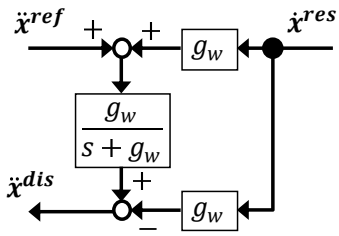

Fig. 4-9: Block diagram of the WOB.

orientation of the tracked vehicle.

4.4.2 Position Control

The position controller in the world coordinates is designed as follows:

$$\ddot{\boldsymbol{x}}_{\boldsymbol{p}}^{\boldsymbol{ref}} = [\ddot{x}^{ref}\ \ddot{y}^{ref}\ *]^T = \boldsymbol{C_p(s)}(\boldsymbol{x^{cmd}} - \boldsymbol{x^{res}}), \tag{4.17}$$

where $\ddot{\boldsymbol{x}}_{\boldsymbol{p}}^{\boldsymbol{ref}}$, $\ddot{x}^{ref}$, and $\ddot{y}^{ref}$ denote the acceleration reference vector provided by the position controller and its X_w and Y_w direction components, respectively. The turning direction component of the acceleration reference is controlled by virtual turning velocity control, and the position controller controls only the X_w and Y_w direction components. The position controller $\boldsymbol{C_p(s)}$ is designed using proportional-derivative (PD) control as follows:

$$\boldsymbol{C_p(s)} = \boldsymbol{K_{pp}} + s\boldsymbol{K_{pd}}, \tag{4.18}$$

where $\boldsymbol{K_{pp}}$ and $\boldsymbol{K_{pd}}$ represent the proportional and derivative gains for the position, respectively.

4.4.3 Virtual Turning Velocity Control Based on Equivalent Lateral Disturbance

We compensate for the disturbances to the crawler motor owing to the driving force and modeling errors using the DOB. Furthermore, we use the WOB to estimate disturbances to the vehicle in the world coordinates (workspace). Figure 4-9 shows a block diagram of the WOB. In the figure, g_W indicates the WOB cutoff frequency. The WOB estimates the disturbance in the acceleration dimension ($\ddot{\boldsymbol{x}}^{\boldsymbol{dis}} = \left[{}^w\ddot{x}^{dis}\ {}^w\ddot{y}^{dis}\ 0\right]^T$) to the vehicle from the acceleration reference $\ddot{\boldsymbol{x}}^{\boldsymbol{ref}}$ and the velocity response $\dot{\boldsymbol{x}}^{\boldsymbol{res}}$ in the world coordinates. Among the estimated disturbances, disturbance compensation in the turning direction is not carried out given the interference with the virtual turning control described below. By using the transformation matrix ${}^{\boldsymbol{w}}\boldsymbol{R_v}$ and selection matrix $\boldsymbol{S}$, the disturbance estimated by the WOB is

decomposed into a translational disturbance ${}^{v}\ddot{\boldsymbol{x}}^{dis}_{tr}$ and a lateral disturbance ${}^{v}\ddot{\boldsymbol{x}}^{dis}_{la}$ as follows:

$$ {}^{v}\ddot{\boldsymbol{x}}^{dis}_{tr} = (\boldsymbol{I} - \boldsymbol{S})\, {}^{w}\boldsymbol{R}_{v}\ddot{\boldsymbol{x}}^{dis} = \begin{bmatrix} {}^{v}\ddot{x}^{dis} & 0 & 0 \end{bmatrix}^{T}, \tag{4.19} $$

$$ {}^{v}\ddot{\boldsymbol{x}}^{dis}_{la} = \boldsymbol{S}\, {}^{w}\boldsymbol{R}_{v}\ddot{\boldsymbol{x}}^{dis} = \begin{bmatrix} 0 & {}^{v}\ddot{y}^{dis} & 0 \end{bmatrix}^{T}, \tag{4.20} $$

$$ \boldsymbol{S} = \mathrm{diag}\begin{bmatrix} 0 & 1 & 0 \end{bmatrix}. \tag{4.21} $$

The translational disturbance ${}^{v}\ddot{\boldsymbol{x}}^{dis}_{tr}$ can be suppressed by feeding it back to the acceleration reference in the world coordinates. The lateral disturbance ${}^{v}\ddot{\boldsymbol{x}}^{dis}_{la}$ is equivalent to the effects of lateral slippage and nonholonomic constraints, defined as the equivalent lateral disturbance. The direct feedback of the equivalent lateral disturbance ${}^{v}\ddot{\boldsymbol{x}}^{dis}_{la}$ does not suppress it because it has nonholonomic constraints. Therefore, a virtual turning velocity control method to suppress the equivalent lateral disturbance is proposed.

In virtual turning velocity control, the equivalent lateral disturbance is indirectly suppressed by ensuring that the turning velocity follows the virtual turning velocity reference, defined using the equivalent lateral disturbance and vehicle velocity. To indirectly compensate for the equivalent lateral disturbance, the vehicle should turn to generate a velocity in the direction opposite to the disturbance. For a sufficiently small slip angle ϕ', the following equation can be derived by transforming the equation of motion in (3.10) using the turning velocity and slipping angular velocity:

$$ mv_x(\dot{\phi} - \dot{\phi}') = f_y = m\,{}^{v}\ddot{y}^{dis}. \tag{4.22} $$

Therefore, the velocity reference to compensate for the equivalent lateral disturbance is defined as the virtual turning velocity reference $\dot{\phi}^{ref}_{vt}$ as follows:

$$ \dot{\phi}^{ref}_{vt} = \frac{{}^{v}\ddot{y}^{dis}}{v_x}. \tag{4.23} $$

In practice, oscillatory variation should be considered because of the division between velocity and acceleration. Therefore, the experimentally determined virtual turning velocity gain K_{vt} and threshold $\dot{\phi}^{lim}_{vt}$ are given by

$$ \dot{\phi}^{ref}_{vt} = K_{vt}\frac{{}^{v}\ddot{y}^{dis}}{v_x}, \tag{4.24} $$

$$ |\dot{\phi}^{ref}_{vt}| \leq \dot{\phi}^{lim}_{vt}. \tag{4.25} $$

The velocity controller is then designed as follows:

$$ \ddot{\boldsymbol{x}}^{\boldsymbol{ref}}_{\boldsymbol{v}} = [* \;\; * \;\; \ddot{\phi}^{ref}]^{T} = \boldsymbol{C_v(s)}(\dot{\phi}^{ref}_{vt} - \dot{\phi}^{res}), \tag{4.26} $$

where $\ddot{\boldsymbol{x}}_{\boldsymbol{v}}^{\boldsymbol{ref}}$ and $\ddot{\phi}^{ref}$ denote the acceleration reference vector provided by the velocity controller and its turning direction component, respectively. The velocity controller $\boldsymbol{C_v}(\boldsymbol{s})$ is designed using proportional (P) control as follows:

$$\boldsymbol{C_v}(\boldsymbol{s}) = K_{vp}, \tag{4.27}$$

where K_{vp} is a scalar parameter and represents the proportional gain for the velocity. The equivalent lateral disturbance is indirectly compensated by ensuring that the tracked vehicle's turning velocity follows the virtual turning velocity reference.

4.4.4 Driving Force Control

The acceleration reference in the world coordinates is obtained using the outputs of the position and virtual turning velocity controllers, as well as the translational direction disturbance as follows:

$$\ddot{\boldsymbol{x}}^{\boldsymbol{ref}} = \ddot{\boldsymbol{x}}_{\boldsymbol{p}}^{\boldsymbol{ref}} + \ddot{\boldsymbol{x}}_{\boldsymbol{v}}^{\boldsymbol{ref}} + {}^{\boldsymbol{v}}\boldsymbol{R}_{\boldsymbol{w}}\, {}^{\boldsymbol{v}}\ddot{\boldsymbol{x}}_{\boldsymbol{tr}}^{\boldsymbol{dis}}. \tag{4.28}$$

The acceleration reference in (4.28) is converted into the vehicle coordinates $\dot{\boldsymbol{v}}^{\boldsymbol{ref}}$ using the command conversion matrix $\boldsymbol{T}$. From this acceleration reference, the driving force reference $\boldsymbol{f}_{\boldsymbol{dr}}^{\boldsymbol{ref}}$ for each crawler is obtained using the distribution method described in Section 4.3. The force controller is designed to feedback the driving force estimated by the DFOB and to track the force reference as follows:

$$\boldsymbol{f}^{\boldsymbol{ref}} = \boldsymbol{C_f}(\boldsymbol{s})(\boldsymbol{f}_{\boldsymbol{dr}}^{\boldsymbol{ref}} - \hat{\boldsymbol{f}}_{\boldsymbol{dr}}). \tag{4.29}$$

The force controller $\boldsymbol{C_f}(\boldsymbol{s})$ is designed using proportional-integral (PI) control as follows:

$$\boldsymbol{C_f}(\boldsymbol{s}) = \boldsymbol{K_{fp}} + \frac{1}{s}\boldsymbol{K_{fi}}, \tag{4.30}$$

where $\boldsymbol{K_{fp}}$ and $\boldsymbol{K_{fi}}$ represent the proportional and integral gains for the driving force, respectively.

4.4.5 Experiments on Proposed Motion Control System

Experiments were conducted to verify (1) the effect of the driving force distribution on turning, (2) the effect of virtual turning velocity control on equivalent lateral disturbance suppression and position control, (3) the tracking and self-localization performance for different trajectories, (4) the stopping position performance in a slippery environment, and (5) the effect of the proposed control on driving on rough terrain.

(1) Effect of Driving Force Distribution on Turning Performance

An experiment was conducted to verify the effect of the driving force distribution on turning. The proposed driving force distribution was compared with the method in [92], which is described by a distribution matrix $\boldsymbol{D}$ consisting of a square Jacobian $\boldsymbol{J}$ and an equivalent inertia matrix $\boldsymbol{M_n}$ as follows:

$$\boldsymbol{D} = \frac{\boldsymbol{J}^{-1}\boldsymbol{M_n}}{R}, \tag{4.31}$$

$$\boldsymbol{M_n} = R^2 \begin{bmatrix} \frac{m}{4} + \frac{J}{W^2} + \frac{J_m}{R^2} & \frac{m}{4} - \frac{J}{W^2} \\ \frac{m}{4} - \frac{J}{W^2} & \frac{m}{4} + \frac{J}{W^2} + \frac{J_m}{R^2} \end{bmatrix} \tag{4.32}$$

The position command vector ($\boldsymbol{x^{cmd}} = \begin{bmatrix} x^{cmd} & y^{cmd} & \phi^{cmd} \end{bmatrix}^T$) is given as a function of time t, where $\boldsymbol{x^{cmd}} = [0 \text{ m } 0 \text{ m } \pi\text{t}/10 \text{ rad}]^T$. The control parameters are listed in Table 4.3. For comparison, the position response, including the turning angle response, was fed back directly instead of using virtual turning velocity control.

Figures 4-10 and 4-11 show the tracking performance along the turning direction using the distribution matrix in (4.31) and the proposed driving force distribution, respectively. In these figures, panels (a) and (b) represent the turning angle and driving force of the crawler, respectively. In Fig. 4-10 (a), poor turning performance is observed when using the distribution matrix. From Fig. 4-10 (b), the driving forces of the crawlers ($\hat{f}^{dr}_{x,r}$, $\hat{f}^{dr}_{x,l}$) follow the references ($f^{ref}_{x,r}$, $f^{ref}_{x,l}$). However, this result suggests that the changes in the driving forces coincide, interfering with each other and consequently hindering the generation of the moment necessary for turning. Conversely, the turning angle suitably follows the given command (Fig. 4-11 (a)). In Fig. 4-11 (b), the left and right driving forces are generated separately. This result indicates that the driving force is distributed to avoid interference. Therefore, turning can be improved by decoupling the driving forces of the crawlers using the proposed driving force distribution.

Table 4.3: Control parameters for the turning control evaluation.

Parameter	Value
Position P gain $\boldsymbol{K_{pp}}$	diag[100 100 9]
Position D gain $\boldsymbol{K_{pd}}$	diag[20 20 6]
Force P gain $\boldsymbol{K_{fp}}$	diag[0.2 0.2]
Force I gain $\boldsymbol{K_{fi}}$	diag[500 500]
Cutoff freq. of DOB g_d	188.4 rad/s
Cutoff freq. of DFOB g_{df}	188.4 rad/s
Cutoff freq. of WOB g_w	31.4 rad/s

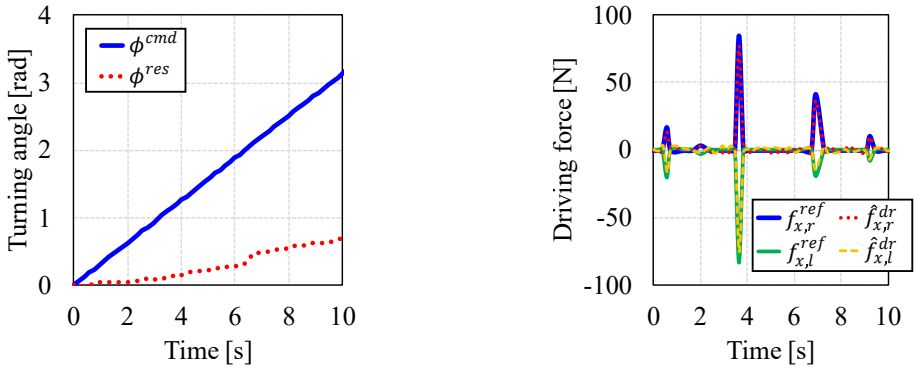

(a) Turning angle. (b) Driving force.

Fig. 4-10: Turning performance using the distribution matrix.

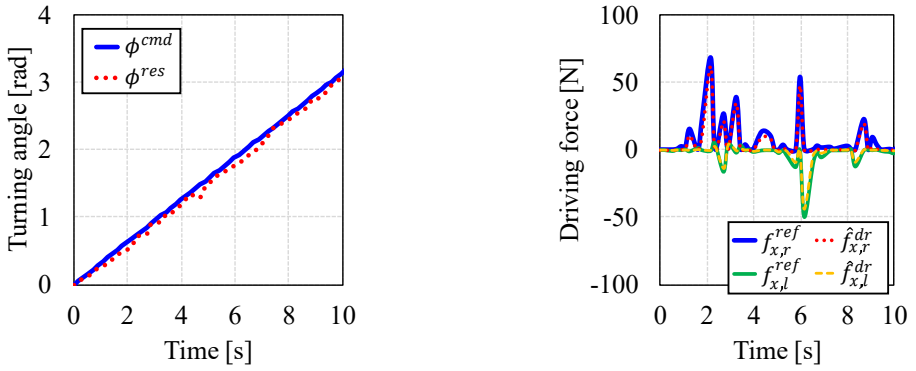

(a) Turning angle. (b) Driving force.

Fig. 4-11: Turning performance using the proposed driving force distribution.

(2) Effect of Virtual Turning Velocity Control on Equivalent Lateral Disturbance Suppression and Position Control

The position tracking performance and disturbance suppression of the proposed system were evaluated. To demonstrate the effectiveness of introducing virtual turning velocity control, cases with and without this control were compared and evaluated. The linear trajectory was given by $\boldsymbol{x^{cmd}} = [0.05 + 0.05t \ -0.025 + 0.025t \ *]^T$. The initial position vector ($\boldsymbol{x^{ini}} = \left[x^{ini} \ y^{ini} \ \phi^{ini}\right]^T$) differs from the initial position command $\boldsymbol{x^{ini}} = \left[0 \text{ m } 0 \text{ m } 0 \text{ rad}\right]^T$. In this experiment, the turning angle command was not considered to control the virtual turning velocity. The parameters that were used in this experiment are listed in Table 4.4. To determine the slippage of the tracked vehicle, the response coordinates (x^{res}, y^{res}), calculated from the crawler motor encoders and inertial measurement unit (IMU), were compared with the absolute coordinates (x^{meas}, y^{meas}) obtained from the detected augmented reality

Table 4.4: Control parameters for the position control evaluation.

Parameter	Value
Position P gain $\boldsymbol{K_{pp}}$	diag[100 100 0]
Position D gain $\boldsymbol{K_{pd}}$	diag[20 20 0]
Force P gain $\boldsymbol{K_{fp}}$	diag[0.2 0.2]
Force I gain $\boldsymbol{K_{fi}}$	diag[500 500]
Cutoff freq. of DOB g_d	188.4 rad/s
Cutoff freq. of DFOB g_{df}	188.4 rad/s
Cutoff freq. of WOB g_w	31.4 rad/s
Virtual turning velocity gain K_{vt}	0.1
Velocity P gain K_{vp}	1.0
Limit virtual turning velocity $\dot{\phi}_v^{lim}$	10 rad/s

(AR) marker position.

Figures 4-12 and 4-13 show the performance without and with virtual turning velocity control, respectively. In these figures, panels (a), (b), and (c) show the trajectory tracking, position response, and equivalent lateral disturbance, respectively. A comparison of Fig. 4-12 (a) and Fig. 4-13 (a) shows that virtual turning velocity control improved the trajectory tracking and reduced the error between the absolute and estimated coordinates. From Fig. 4-12 (b) and Fig. 4-13 (b), the tracking performance along the Y_w axis was improved using virtual turning velocity control. Furthermore, a comparison of Fig. 4-12 (c) and Fig. 4-13 (c) shows the effect of virtual turning velocity control on the equivalent lateral disturbance suppression. Without virtual turning velocity control, the influence of the equivalent lateral disturbance is apparent, particularly in terms of lateral positioning. Conversely, the positioning performance is likely improved by suppressing the equivalent lateral disturbance using virtual turning velocity control. Furthermore, the performance of self-localization can be improved by appropriately suppressing slippage because the difference between the absolute and response coordinates decreased with the introduction of virtual turning velocity control. These results confirm that the proposed control system improves the positioning performance of the tracked vehicle while appropriately allowing for slippage along the turning direction.

(3) Tracking and Self-localization Performance for Different Trajectories

The tracking and self-localization performance for various trajectories were evaluated. The position commands listed in Table 4.5 were given as trajectories for 20 s. In this evaluation, the same control

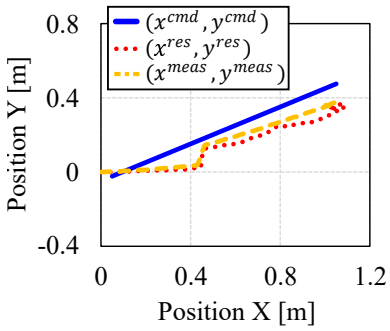

(a) Trajectory.

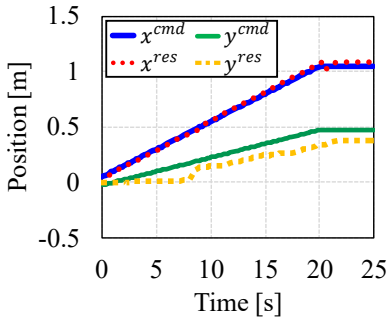

(b) Position.

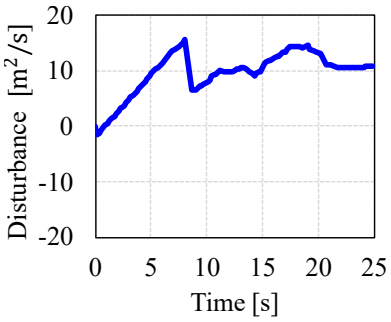

(c) Equivalent lateral disturbance.

Fig. 4-12: Tracking performance without virtual turning velocity control.

Table 4.5: Position command.

Trajectory	Position command vector ($\boldsymbol{x^{cmd}}$)
Quadratic curve	$[0.04t\ 0.008t^2\ *]^T$
Circle	$[0.4\sin(0.1\pi t)\ -0.4\cos(0.1\pi t)\ *]^T$

parameters that are summarized in Table 4.4 were used. The initial position vector $\boldsymbol{x^{ini}}$ was set to be the same as the initial value of the position command vector. Here, the norms between the absolute coordinates (x^{meas}, y^{meas}) and position command (x^{cmd}, y^{cmd}) at each sampling were treated as positioning errors. To evaluate the effect of slippage on the self-localization, the norms between the position response (x^{res}, y^{res}) and the absolute coordinates (x^{meas}, y^{meas}) at each sampling were treated as self-localization errors.

Table 4.6 and Table 4.7 summarize the statistics of the positioning errors and self-localization errors for each trajectory, respectively. Table 4.6 helps confirm that the performance of the proposed system is comparable for different trajectories. Furthermore, Table 4.6 indicates that the difference between the position response and the absolute coordinates is suppressed, regardless of the trajectory. The slight

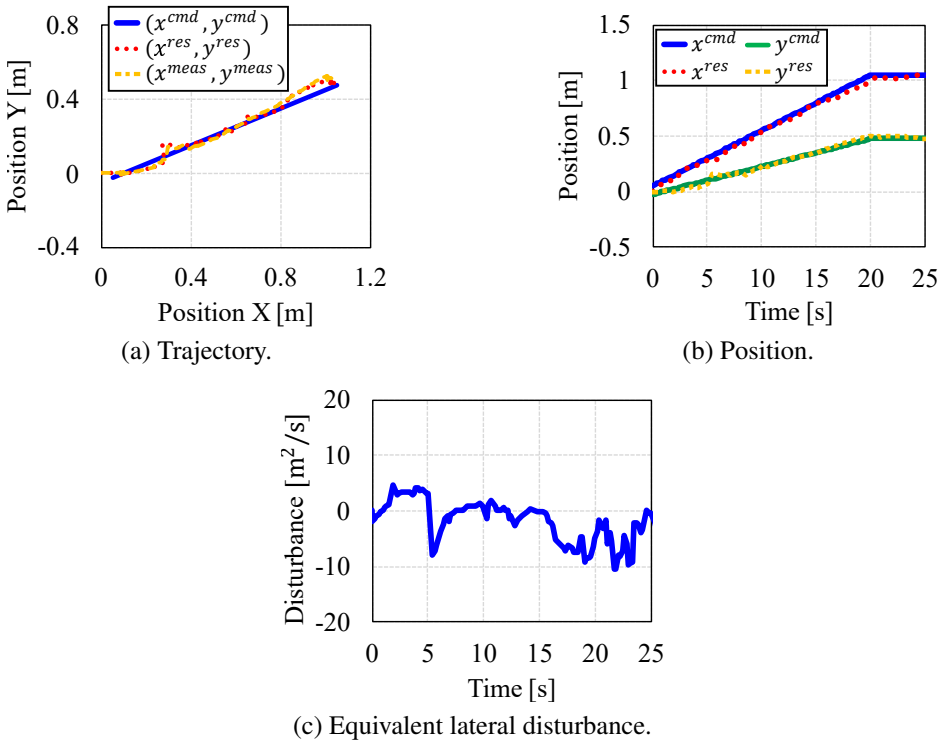

(a) Trajectory.

(b) Position.

(c) Equivalent lateral disturbance.

Fig. 4-13: Tracking performance with virtual turning velocity control.

Table 4.6: Positioning performance.

	Maximum error	Average error	Standard deviation
Quadratic curve	0.054 m	0.023 m	0.014 m
Circle	0.072 m	0.028 m	0.016 m

difference between the absolute and response coordinates suggests that the slippage was sufficiently suppressed.

(4) Stopping Position Performance in a Slippery Environment

Using the proposed positioning control system, the effects on positioning accuracy in a slippery environment were evaluated. This experiment was conducted in the environment shown in Fig. 4-14. Rubber was used at the start of the tracked vehicle's travel route, and slippery polytetrafluoroethylene (PTFE) was used at the stop position. In this experiment, the control system shown in Fig. 4-8 and the control parameters shown in Table 4.4 were used. The TVNN was already trained in the rubber and PTFE environments. The position command vector ($\boldsymbol{x^{cmd}} = \left[x^{cmd}\ y^{cmd}\ \phi^{cmd}\right]^T$) of the tracked vehicle was

Table 4.7: Self-localization performance.

	Maximum error	Average error	Standard deviation
Quadratic curve	0.031 m	0.017 m	0.007 m
Circle	0.032 m	0.017 m	0.008 m

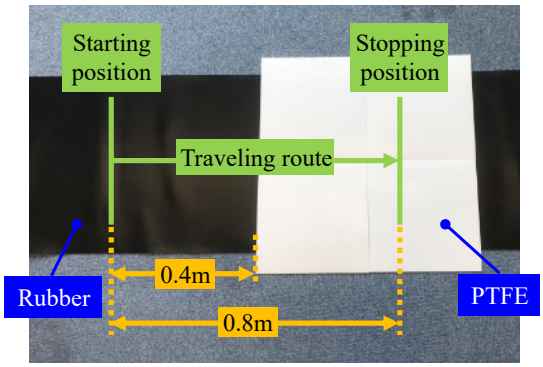

Fig. 4-14: Experimental setup.

given as follows:

$$x^{cmd} = \begin{cases} 0.4t & (t < 2.0) \\ 0.8 & (t \geq 2.0). \end{cases}, \tag{4.33}$$

$$y^{cmd} = 0, \tag{4.34}$$

$$\phi^{cmd} = 0. \tag{4.35}$$

The initial position vector is set as $\boldsymbol{x}^{\boldsymbol{ini}} = \left[0 \text{ m } 0 \text{ m } 0 \text{ rad}\right]^T$. For comparative evaluation, the crawler velocity calculated from the encoder value of the crawler motor and the estimated velocity by the TVNN and the inverse kinematics were used as inputs for the DFOB as shown in Table 4.8. In this experiment, as well as the position control evaluation, the norms between the absolute coordinates (x^{meas}, y^{meas}) were treated as positioning errors. To evaluate the stopping position accuracy, the data after 2 s, when the position command of the following vehicle became a constant value, was used. Figures 4-15 and 4-16 show the experimental results of each case. In the figures, panels (a) and (b) show the time response of the position in the X_w and Y_w directions, respectively. It switched from a rubber road to a PTFE road at approximately 1 s. From Fig. 4-15(a), it is confirmed that the response coordinates in the X_w direction follow the position command, although there is an error in the PTFE data. However, checking the absolute coordinates shows that there is a deviation from the command value, indicating that slippage

Table 4.8: Experimental conditions in positioning by suppressing translational slip.

Case No.	Velocity input to DFOB
case 1	Velocity estimated by motor encoder
case 2	Velocity estimated by TVNN

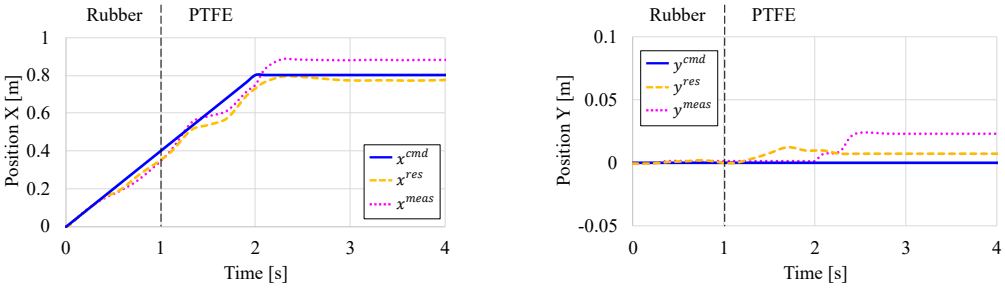

(a) Position X (b) Position Y

Fig. 4-15: Stopping position accuracy (case 1).

has occurred. This suggests that slippage cannot be sufficiently suppressed by the driving force when it is calculated based on the velocity without slippage obtained from the crawler motor encoder. The effect of slippage in the translational direction (X_w direction in this experiment) also affects the positioning accuracy in the lateral direction (Y_w direction in this experiment), as shown in Fig. 4-15(b). This is because the response coordinates of the crawler are calculated using the translation distance obtained from the crawler motor encoder and the attitude angle obtained using the IMU, and the error in the translation distance is considered to be reflected in the lateral direction.

On the other hand, Fig. 4-16(a) shows that both the response coordinates and absolute coordinates follow the position command even on the course, including the PTFE surface. At the stopping position, the error between the response coordinate and absolute coordinate is also reduced, indicating that the driving force control using the estimated vehicle velocity by the TVNN suppresses the slippage in the translational direction. Figure 4-16(b) also shows that the tracking to the position command has been improved in the lateral direction. Table 4.9 summarizes the statistics of the positioning errors. This table shows that the proposed position control system achieved high stopping positioning accuracy by suppressing slippage in the translational direction and suppressing lateral disturbance. Particularly, it is shown that the stopping positioning accuracy can effectively be improved by accurately determining the driving force to suppress the translational slippage from the vehicle velocity, including slippage.

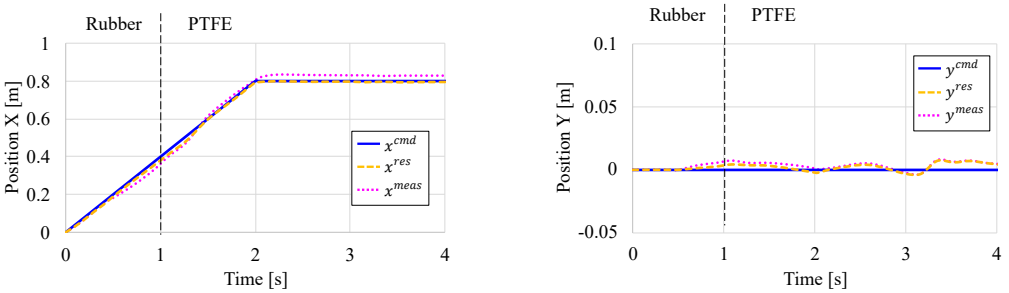

(a) Position X. (b) Position Y.

Fig. 4-16: Stopping position accuracy (case 2).

Table 4.9: Positioning performance.

	Maximum error	Average error	Standard deviation
case 1	0.114 m	0.061 m	0.026 m
case 2	0.032 m	0.025 m	0.008 m

(5) Effect of Proposed Control on Driving on Rough Terrain

The proposed position control performance was evaluated by driving tests on rough terrain. This experiment was conducted in the environment shown in Fig. 4-17. In the figure, panels (a) and (b) show the appearance of the rough terrain and environmental information of the driving surface, respectively. The rough terrain was created by combining different heights and friction coefficients, such as PTFE, rubber, and artificial grass. In this experiment, the position command vectors ($\boldsymbol{x^{cmd}} = \left[x^{cmd}\ y^{cmd}\ *\right]^T$) were applied to the tracked vehicle to achieve a straight-line or diagonal motion, as listed in Table 4.10. The initial position vector $\boldsymbol{x^{ini}}$ was set to the same as the initial value of the position command vector. The experiments were conducted under the conditions listed in Table 4.11 to confirm the effectiveness of the control elements (acceleration control, driving force control, driving force distribution, and virtual turning velocity control) that constitute the proposed position control system.

Figures 4-18∼4-21 show the experimental results when the straight-line motion command is given. In each figure, panels (a) and (b) show the position (x^{res}, y^{res}) and posture responses, respectively. The changes in roll angle (angle with a positive value around the right of the X_w axis) and pitch angle (angle with a positive value around the right of the Y_w axis), indicated by panel (b) in each figure, are caused by the change in the height of the driving surface. From Fig. 4-18 (a), the effect of the rough terrain, such as bumps between driving surface environments, affects the position control responsiveness in the straight

Table 4.10: Positioning command vector.

Motion	Time t	x^{cmd}	y^{cmd}
Straight-line motion	0∼3 s	0.4t m	0 m
	3 ∼ 4 s	1.2 m	0 m
Diagonal motion	0∼3 s	0.4t m	-0.04t m
	3 ∼ 4 s	1.2 m	-0.12 m

Table 4.11: Control conditions.

Case No.	Acceleration control	Driving force control	Driving force distribution	Virtual turning control
case 1	Enable	Disable	Disable	Disable
case 2	Enable	Enable	Disable	Disable
case 3	Enable	Enable	Enable	Disable
case 4	Enable	Enable	Enable	Enable

line direction based on acceleration control in case 1. On the other hand, from Fig. 4-19 (a), in case 2, it can be observed that the responsiveness in the straight-line direction is improved using driving force feedback. Comparing Figs. 4-19 (a) and 4-20 (a), there is no noticeable difference in the position in the straight-line direction (x^{res}); however, the lateral position (y^{res}) shifted. This is thought to be because the driving force is distributed based on the instantaneous center, which is calculated based on the yaw angle in the proposed position control system; however, the yaw angle changes when driving on rough terrain. Finally, comparing Figs. 4-20 (a) and 4-21 (a) confirmed that introducing the virtual turning velocity control reduced the lateral misalignment because the lateral slippage was properly compensated.

Figures 4-22∼4-25 show the experimental results when a diagonal command is given. When Figs. 4-22∼4-25 were compared, the response in the lateral direction could not be confirmed by the driving force feedback, while the response in the lateral direction could be observed by the driving force distribution. Furthermore, from Fig. 4-25, it was confirmed that the virtual turning velocity control improved the position response in the lateral direction. The aforementioned results confirm that the proposed position control algorithm can function even when driving on rough terrain.

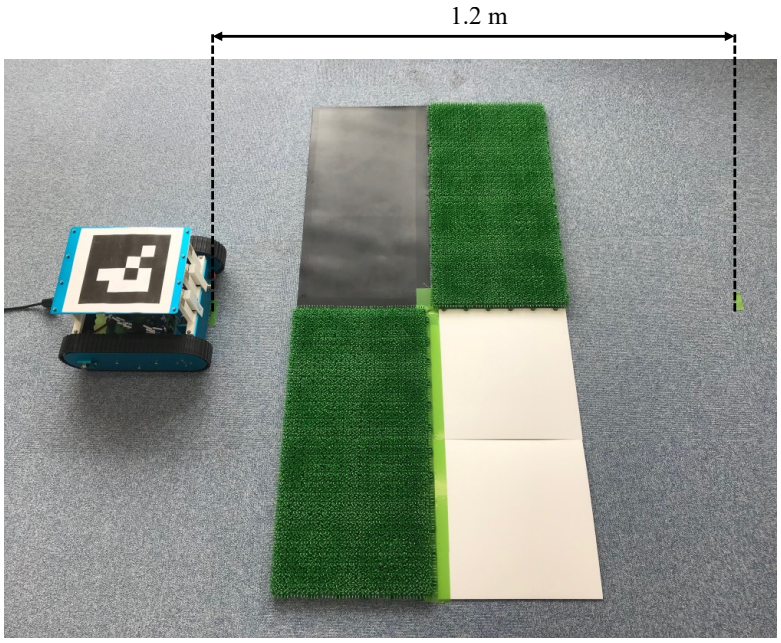

(a) Appearance.

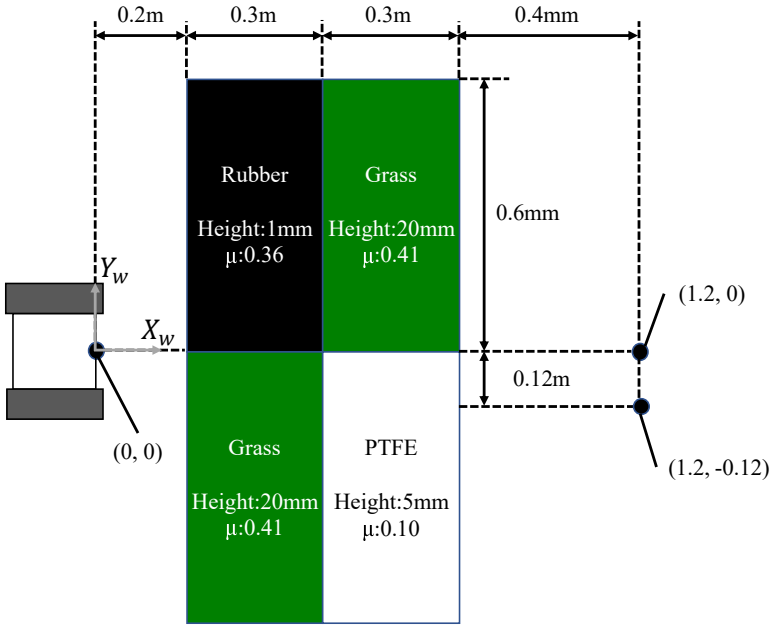

(b) Environmental information of the road surface.

Fig. 4-17: Experimental environment for driving on a rough terrain.

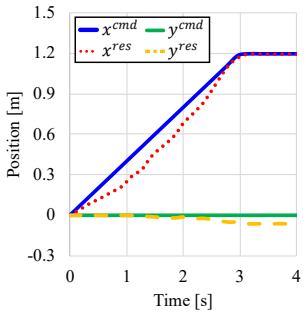

(a) Position.

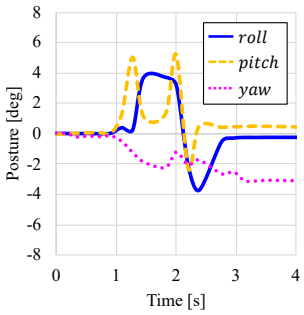

(b) Posture.

Fig. 4-18: Experimental result (straight-line motion, case 1).

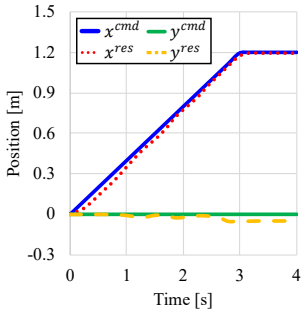

(a) Position.

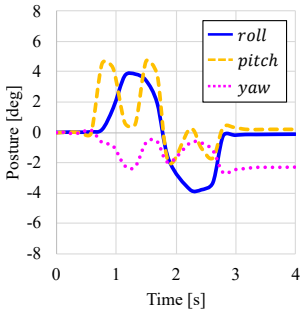

(b) Posture.

Fig. 4-19: Experimental result (straight-line motion, case 2).

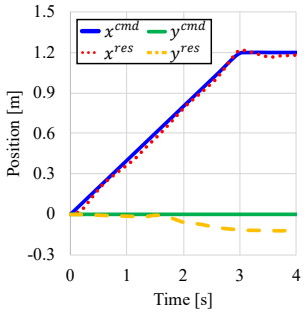

(a) Position.

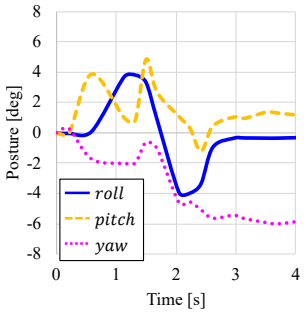

(b) Posture.

Fig. 4-20: Experimental result (straight-line motion, case 3).

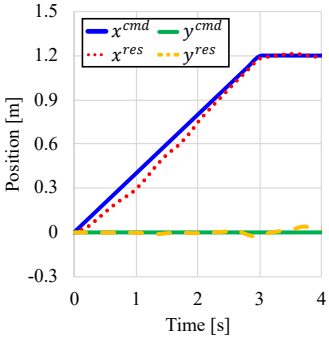

(a) Position.

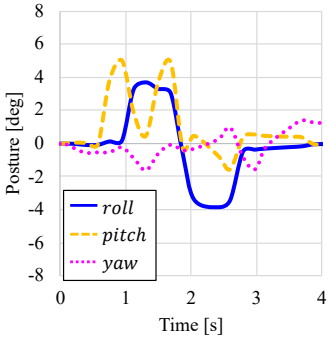

(b) Posture.

Fig. 4-21: Experimental result (straight-line motion, case 4).

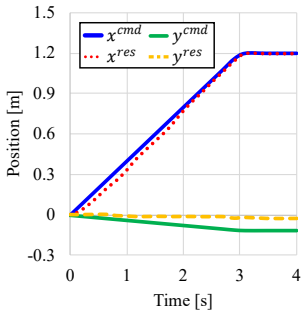

(a) Position.

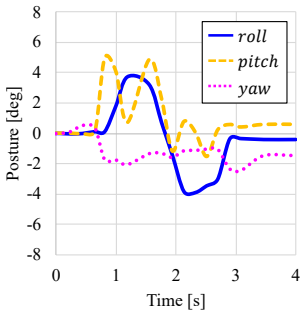

(b) Posture.

Fig. 4-22: Experimental result (diagonal motion, case 1).

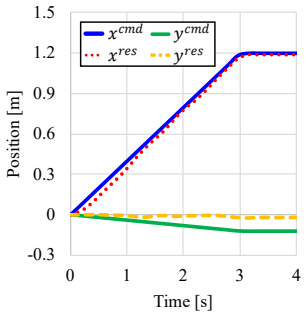

(a) Position.

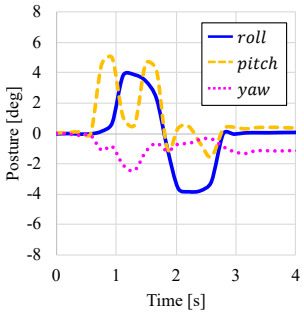

(b) Posture.

Fig. 4-23: Experimental result (diagonal motion, case 2).

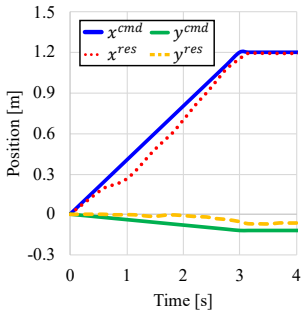

(a) Position.

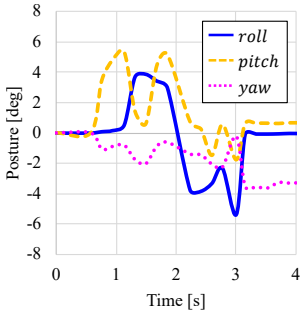

(b) Posture.

Fig. 4-24: Experimental result (diagonal motion, case 3).

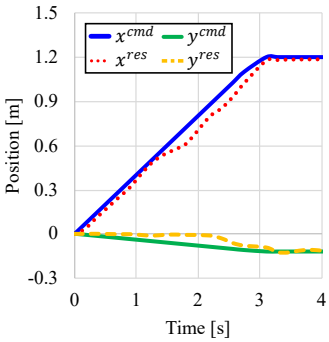

(a) Position.

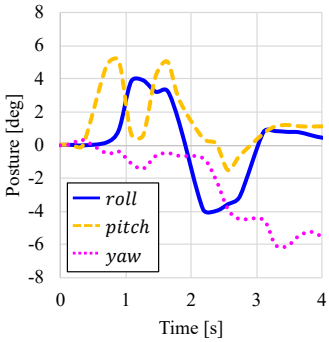

(b) Posture.

Fig. 4-25: Experimental result (diagonal, case 4).

4.5 Discussion of Proposed Control System Stability Based on Passivity

This section discusses the stability of the proposed position control system based on the passivity theory. Passivity is a concept initially used to describe the energy depletion characteristics of a system in which multiple conversion circuits are coupled[93]. This concept can be used to evaluate the stability of the energy dissipation characteristics of the entire system. In addition, motion control has been proposed by focusing on the passivity of nonlinear mechanical systems such as robot manipulators and mobile manipulators, which are represented by the Euler–Lagrange equations[94–96].

In this chapter, the Lagrange equations for a mobile robot subject to nonholonomic constraints are first formulated and discussed based on passivity. In this study, it is assumed that slippage is properly suppressed by driving force control and virtual turning velocity control, and that the tracked vehicle has dynamics dynamics that are equivalent to a general two-wheeled mobile robot. For discussion, defining the generalized coordinates as $\boldsymbol{q} = \begin{bmatrix} \boldsymbol{x} \ \boldsymbol{\theta} \end{bmatrix}^T$, the position vector in the vehicle coordinates $\boldsymbol{x} = \begin{bmatrix} x \ y \ \phi \end{bmatrix}^T$, and the crawler motor angle vector $\boldsymbol{\theta} = \begin{bmatrix} \theta_r \ \theta_l \end{bmatrix}^T$, the dynamics can be expressed by the Lagrange equations as follows:

$$\boldsymbol{M}(\boldsymbol{q})\ddot{\boldsymbol{q}} + \boldsymbol{V}(\boldsymbol{q}, \dot{\boldsymbol{q}})\dot{\boldsymbol{q}} + \boldsymbol{G}(\boldsymbol{q}) = \boldsymbol{E}(\boldsymbol{q})\boldsymbol{u} + \boldsymbol{A}^{\boldsymbol{T}}(\boldsymbol{q})\boldsymbol{\lambda}, \tag{4.36}$$

where $\boldsymbol{u}$ is an input vector, $\boldsymbol{M}(\boldsymbol{q})$ is a symmetric and positive definite inertia matrix, $\boldsymbol{V}(\boldsymbol{q}, \dot{\boldsymbol{q}})$ is the centripetal and Coriolis matrix, $\boldsymbol{G}(\boldsymbol{q})$ is the gravitational vector, $\boldsymbol{E}(\boldsymbol{q})$ is an input transformation matrix, $\boldsymbol{A}(\boldsymbol{q})$ is a matrix associated with nonholonomic constraints, and $\boldsymbol{\lambda}$ is a vector of constraint forces. The kinematic relationship between the generalized velocity and the crawler motor velocity is represented by a Jacobian matrix as follows:

$$\dot{\boldsymbol{x}} = \boldsymbol{J}\dot{\boldsymbol{\theta}}, \tag{4.37}$$

Using this time differentiation, the generalized acceleration and crawler motor acceleration are expressed as follows:

$$\begin{aligned} \ddot{\boldsymbol{x}} &= \boldsymbol{J}\ddot{\boldsymbol{\theta}} + \dot{\boldsymbol{J}}\dot{\boldsymbol{\theta}}, \\ &\simeq \boldsymbol{J}\ddot{\boldsymbol{\theta}} \end{aligned} \tag{4.38}$$

The matrix $\boldsymbol{A}$, which represents the nonholonomic constraint in (4.36), satisfies $\boldsymbol{A}(\boldsymbol{q})\dot{\boldsymbol{q}} = \boldsymbol{0}$ by definition. The null space of matrix $\boldsymbol{A}$ is represented by the matrix $\boldsymbol{S}(\boldsymbol{q})$. This matrix satisfies as follows:

$$\boldsymbol{A}(\boldsymbol{q})\boldsymbol{S}(\boldsymbol{q}) = \boldsymbol{0}. \tag{4.39}$$

In a two-wheeled mobile robot, this matrix $\boldsymbol{S}$ shows the relationship between the generalized velocity and the vehicle velocity vector $\boldsymbol{v} = \left[v_x \ \dot{\phi}\right]^T$ as follows:

$$\dot{\boldsymbol{q}} = \boldsymbol{S}(\boldsymbol{q})\boldsymbol{v}. \tag{4.40}$$

Similarly, the relationship between the generalized acceleration and vehicle acceleration can be represented as follows:

$$\begin{aligned} \ddot{\boldsymbol{q}} &= \boldsymbol{S}(\boldsymbol{q})\dot{\boldsymbol{v}} + \dot{\boldsymbol{S}}(\boldsymbol{q})\boldsymbol{v}, \\ &\simeq \boldsymbol{S}(\boldsymbol{q})\dot{\boldsymbol{v}}. \end{aligned} \tag{4.41}$$

The dynamics in (4.36) can be reduced to a lower dimension by using (4.40) and (4.41) as follows:

$$\begin{aligned} &\bar{\boldsymbol{M}}(\boldsymbol{q})\dot{\boldsymbol{v}} + \bar{\boldsymbol{V}}(\boldsymbol{q}, \dot{\boldsymbol{q}})\boldsymbol{v} + \bar{\boldsymbol{G}}(\boldsymbol{q}) = \bar{\boldsymbol{E}}(\boldsymbol{q})\boldsymbol{u} = \boldsymbol{f}, \\ &\bar{\boldsymbol{M}}(\boldsymbol{q}) = \boldsymbol{S}^{\boldsymbol{T}}(\boldsymbol{q})\boldsymbol{M}(\boldsymbol{q})\boldsymbol{S}(\boldsymbol{q}), \\ &\bar{\boldsymbol{V}}(\boldsymbol{q}, \dot{\boldsymbol{q}}) = \boldsymbol{S}^{\boldsymbol{T}}(\boldsymbol{q})(\boldsymbol{M}(\boldsymbol{q})\dot{\boldsymbol{S}}(\boldsymbol{q}) + \dot{\boldsymbol{M}}(\boldsymbol{q})\boldsymbol{S}(\boldsymbol{q})), \\ &\bar{\boldsymbol{G}}(\boldsymbol{q}) = \boldsymbol{S}^{\boldsymbol{T}}(\boldsymbol{q})\boldsymbol{G}(\boldsymbol{q}), \\ &\bar{\boldsymbol{E}}(\boldsymbol{q}) = \boldsymbol{S}^{\boldsymbol{T}}(\boldsymbol{q})\boldsymbol{E}(\boldsymbol{q}), \\ &\boldsymbol{f} = \left[f_x \ \tau_z\right]^T, \end{aligned} \tag{4.42}$$

where $\boldsymbol{f}$, f_x, and τ_z denote the input force vector to the dynamics, sum of the driving force in the translational direction, and the moment in the turning direction in the vehicle coordinates, respectively. For convenience, the relationship between the vehicle and crawler motor velocities is assumed to be represented by the Jacobian matrix $\boldsymbol{J_v}$ as follows:

$$\boldsymbol{v} = \boldsymbol{J_v}\dot{\boldsymbol{\theta}}. \tag{4.43}$$

The relationship between the vehicle and crawler motor accelerations is expressed as follows:

$$\begin{aligned} \dot{\boldsymbol{v}} &= \boldsymbol{J_v}\ddot{\boldsymbol{\theta}} + \dot{\boldsymbol{J}}_{\boldsymbol{v}}\dot{\boldsymbol{\theta}}, \\ &\simeq \boldsymbol{J_v}\ddot{\boldsymbol{\theta}}. \end{aligned} \tag{4.44}$$

The passivity of the proposed position control system is investigated using the aforementioned kinematic and dynamic relationships. First, let us consider a candidate Lyapunov function $\boldsymbol{V}$ as follows:

$$\boldsymbol{V} = \frac{1}{2}\dot{\boldsymbol{q}}^{\boldsymbol{T}}\boldsymbol{M}(\boldsymbol{q})\dot{\boldsymbol{q}} + \frac{1}{2}(\boldsymbol{x}^{\boldsymbol{cmd}} - \boldsymbol{x}^{\boldsymbol{res}})^{\boldsymbol{T}}\boldsymbol{K_x}(\boldsymbol{x}^{\boldsymbol{cmd}} - \boldsymbol{x}^{\boldsymbol{res}}) + \frac{1}{2}\boldsymbol{v}^{\boldsymbol{T}}\boldsymbol{K_v}\boldsymbol{v}, \tag{4.45}$$

where $\boldsymbol{K_x}$ and $\boldsymbol{K_v}$ are arbitrary positive definite matrices. Thus, the function $\boldsymbol{V}$ is a positive definite function for $\dot{\boldsymbol{q}}$, $\boldsymbol{x}$, and $\boldsymbol{v}$. The time derivative of the function using (4.42), (4.37), (4.40), and (4.43) is calculated as follows:

$$\dot{\boldsymbol{V}} = \boldsymbol{v}^{\boldsymbol{T}} \boldsymbol{S}^{\boldsymbol{T}}(\boldsymbol{q}) \left(\boldsymbol{f} - \boldsymbol{J}_{\boldsymbol{v}}^{-\boldsymbol{T}} \boldsymbol{J}^{-\boldsymbol{T}} \boldsymbol{K}_{\boldsymbol{x}} (\boldsymbol{x}^{\boldsymbol{cmd}} - \boldsymbol{x}^{\boldsymbol{res}}) + \boldsymbol{K}_{\boldsymbol{v}} \bar{\boldsymbol{M}}^{-\boldsymbol{1}}(\boldsymbol{q}) \boldsymbol{f} \right). \tag{4.46}$$

By determining the input force vector $\boldsymbol{f}$ using an arbitrary positive definite diagonal matrix $\boldsymbol{K_s}$ as

$$\boldsymbol{f} = (\boldsymbol{I} + \boldsymbol{K}_{\boldsymbol{v}} \bar{\boldsymbol{M}}^{-\boldsymbol{1}}(\boldsymbol{q}))^{-\boldsymbol{1}} \left(\boldsymbol{J}_{\boldsymbol{v}}^{-\boldsymbol{T}} \boldsymbol{J}^{-\boldsymbol{T}} \boldsymbol{K}_{\boldsymbol{x}} (\boldsymbol{x}^{\boldsymbol{cmd}} - \boldsymbol{x}^{\boldsymbol{res}}) - \boldsymbol{K}_{\boldsymbol{s}} \boldsymbol{v} \right), \tag{4.47}$$

(4.46) becomes

$$\dot{\boldsymbol{V}} = -\boldsymbol{v}^{\boldsymbol{T}} \boldsymbol{S}^{\boldsymbol{T}}(\boldsymbol{q}) \boldsymbol{K}_{\boldsymbol{v}} \boldsymbol{v} \leq \boldsymbol{0}. \tag{4.48}$$

Therefore, the equilibrium point of the system ($\dot{\boldsymbol{q}}$, $\boldsymbol{x}$, and $\boldsymbol{v}$) = ($\boldsymbol{0}$, $\boldsymbol{x}^{\boldsymbol{cmd}}$, $\boldsymbol{0}$) is is stabilized. Thus, the function $\boldsymbol{V}$ is a Lyapunov function for $\dot{\boldsymbol{q}}$, $\boldsymbol{x}$, and $\boldsymbol{v}$. When comparing the input force vector in (4.47) with the block diagram of the proposed position control system shown in Fig. 4-8, it can be interpreted that the first term is a position controller (proportional control) in the world coordinates, the second term is the driving force feedback to the vehicle, and the third term is the damping injection by velocity feedback.

Next, to add velocity control in the world coordinates to the input force vector designed for stability, (4.42) is redefined using an arbitrary positive definite matrix $\boldsymbol{K_{xd}}$ as follows:

$$\bar{\boldsymbol{M}}(\boldsymbol{q}) \dot{\boldsymbol{v}} + \bar{\boldsymbol{V}}(\boldsymbol{q}, \dot{\boldsymbol{q}}) \boldsymbol{v} + \bar{\boldsymbol{G}}(\boldsymbol{q}) = \bar{\boldsymbol{E}}(\boldsymbol{q}) \boldsymbol{u} = \boldsymbol{f} + \boldsymbol{f_d}, \tag{4.49}$$

$$\boldsymbol{f_d} = \boldsymbol{J}_{\boldsymbol{v}}^{-\boldsymbol{T}} \boldsymbol{J}^{-\boldsymbol{T}} \boldsymbol{K}_{\boldsymbol{xd}} (\dot{\boldsymbol{x}}^{\boldsymbol{cmd}} - \dot{\boldsymbol{x}}^{\boldsymbol{res}}). \tag{4.50}$$

Thus, the time derivative of the function using (4.49), (4.37), (4.40), and (4.43) is calculated as follows:

$$\dot{\boldsymbol{V}} = \boldsymbol{v}^{\boldsymbol{T}} \boldsymbol{S}^{\boldsymbol{T}}(\boldsymbol{q}) \boldsymbol{f_d} - \boldsymbol{v}^{\boldsymbol{T}} \boldsymbol{S}^{\boldsymbol{T}}(\boldsymbol{q}) \boldsymbol{K}_{\boldsymbol{v}} \boldsymbol{v} \leq \boldsymbol{v}^{\boldsymbol{T}} \boldsymbol{S}^{\boldsymbol{T}}(\boldsymbol{q}) \boldsymbol{f_d}. \tag{4.51}$$

From (4.51), the system in (4.49) is passive when $\boldsymbol{v}$ is the output. Additionally, the system in (4.49) converges to the points $(\dot{\boldsymbol{q}}, \boldsymbol{x}, \boldsymbol{v}) = (\boldsymbol{0}, \boldsymbol{x}^{\boldsymbol{cmd}}, \boldsymbol{0})$ because it is zero-state detectable. Therefore, it can be said that the system in (4.49) is asymptotically stable. Thus, the input force vector can be updated as follows:

$$\boldsymbol{f} = (\boldsymbol{I} + \boldsymbol{K}_{\boldsymbol{v}} \bar{\boldsymbol{M}}^{-\boldsymbol{1}}(\boldsymbol{q}))^{-\boldsymbol{1}} \left(\boldsymbol{J}_{\boldsymbol{v}}^{-\boldsymbol{T}} \boldsymbol{J}^{-\boldsymbol{T}} (\boldsymbol{K}_{\boldsymbol{x}} (\boldsymbol{x}^{\boldsymbol{cmd}} - \boldsymbol{x}^{\boldsymbol{res}}) + \boldsymbol{K}_{\boldsymbol{xd}} (\dot{\boldsymbol{x}}^{\boldsymbol{cmd}} - \dot{\boldsymbol{x}}^{\boldsymbol{res}})) - \boldsymbol{K}_{\boldsymbol{s}} \boldsymbol{v} \right), \tag{4.52}$$

Finally, to include the driving force distribution explicitly, the input force vector in (4.52) is set using the weight matrix $\boldsymbol{w} = diag\left[w_r\ w_l\right]^T$ as follows:

$$\boldsymbol{f} = \bar{\boldsymbol{E}}^{-\boldsymbol{1}}\boldsymbol{w}\boldsymbol{u} = \boldsymbol{J}_{\boldsymbol{v}}^{-\boldsymbol{T}}\boldsymbol{w}\boldsymbol{u}. \tag{4.53}$$

Substituting (4.53) into (4.52), the control input to the crawler motor $\boldsymbol{u}$ is obtained as follows:

$$\begin{aligned}\boldsymbol{u} = &(\boldsymbol{J}_{\boldsymbol{v}}^{-\boldsymbol{T}}\boldsymbol{w})^{-\boldsymbol{1}}(\boldsymbol{I} + \boldsymbol{K}_{\boldsymbol{v}}\bar{\boldsymbol{M}}^{-\boldsymbol{1}}(\boldsymbol{q}))^{-\boldsymbol{1}} \\ &\Big(\boldsymbol{J}_{\boldsymbol{v}}^{-\boldsymbol{T}}\boldsymbol{J}^{-\boldsymbol{T}}(\boldsymbol{K}_{\boldsymbol{x}}(\boldsymbol{x}^{\boldsymbol{cmd}} - \boldsymbol{x}^{\boldsymbol{res}}) + \boldsymbol{K}_{\boldsymbol{xd}}(\dot{\boldsymbol{x}}^{\boldsymbol{cmd}} - \dot{\boldsymbol{x}}^{\boldsymbol{res}})) - \boldsymbol{K}_{\boldsymbol{s}}\boldsymbol{v}\Big).\end{aligned} \tag{4.54}$$

By comparing (4.54) and the block diagram of the proposed position control shown in Fig. 4-8, it can be observed that the position controller (proportional and derivative) generates an acceleration control reference, driving force feedback, and driving force distribution is expressed explicitly. Additionally, (4.54) shows that it is necessary to feed back the vehicle velocity to stabilize the system. On the other hand, the driving force controller and disturbance suppression by the DOB, WOB, and virtual turning velocity control in the proposed method cannot be expressed by (4.54). Therefore, under the assumption that the driving force controller operates stably and that the disturbance suppression by the DOB, WOB, and virtual turning velocity control is high enough not to affect the dynamics, the conditions for the control system to satisfy passivity are listed as follows:

(1) $\boldsymbol{I} + \boldsymbol{K}_{\boldsymbol{v}}\bar{\boldsymbol{M}}^{-\boldsymbol{1}}(\boldsymbol{q})$ is a regular matrix.

(2) $\boldsymbol{J}_{\boldsymbol{v}}^{-\boldsymbol{T}}\boldsymbol{w}$ is a regular matrix.

(3) The vehicle velocity is fed back.

Condition (1) is always satisfied because $\boldsymbol{K}_{\boldsymbol{v}}$ and $\bar{\boldsymbol{M}}(\boldsymbol{q})$ are positive definite symmetric matrices. As for condition (2), because $\boldsymbol{J}_{\boldsymbol{v}}$ is regular, the equivalent condition is that $\boldsymbol{w}$ is regular. As described in Section 4.3, $\boldsymbol{w}$ is determined by the instantaneous turning center and takes the value $\boldsymbol{0} < \boldsymbol{w} < \dfrac{W}{2}\boldsymbol{I}$. However, when the weight of the driving force of either the right or left crawler (w_r or w_l) is zero, the rank number of $\boldsymbol{w}$ decreases. Therefore, it is necessary to use a threshold value to make $w_r \neq 0$ or $w_l \neq 0$). As for condition (3), because the proposed position control system is based on acceleration control, it is not easy to feed back the vehicle velocity directly to the control system. To feedback the vehicle velocity, it is necessary to feed back the vehicle acceleration, which is the time derivative of the vehicle velocity. In the actual design, the time derivative of the vehicle velocity should be realized by pseudo-differentiation using a low-pass filter while considering noise sensitivity. As previously mentioned, the stability of the

proposed position control is discussed based on passivity. The method of feeding back vehicle velocity to ensure stability is a future issue.

4.6 Summary

This chapter proposes a method to estimate the driving force of a tracked vehicle and a motion control system based on driving force. First, a driving force observer was designed based on the velocity estimated by the method discussed in Chapter 3. Next, a driving control system was constructed to suppress slippage by connecting it to the velocity control system. The validity of the proposed driving force control was verified through an experimental evaluation of the slip suppression performance. Conventional driving force control uses a velocity that is based on the motor encoder and does not include slippage; however, the application effect of the proposed method for estimating and controlling the driving force based on an estimate of the correct velocity including slippage is demonstrated. This chapter also proposed driving force distribution to control the tracked vehicle and virtual turning velocity control to suppress the equivalent lateral disturbance. The proposed driving force distribution uses the instantaneous turning center of the vehicle to enable crawler decoupling and induce proper slip along the turning direction. Furthermore, the virtual turning velocity control suppressed the equivalent lateral disturbance extracted by the WOB. The experimental results show that the position tracking performance can be improved by appropriately slipping the tracked vehicle while suppressing the lateral disturbance. Finally, based on passivity, the stability of the proposed position control system was discussed.

The proposed velocity estimation and driving force control methods can be applied to all mobile robots traveling in places where the slippage environment cannot be ignored. The driving force control proposed in this chapter suppresses the occurrence of slippage; however, it may become saturated depending on the driving force criterion. In such cases, countermeasures such as adjusting the driving force criterion are necessary. Future work will include consideration of countermeasures such as the prevention of hoisting in the event of extreme slippage.

Chapter 5

Force Control Mechanism Adaptable to Environment

5.1 Introduction

This chapter presents a force control mechanism and a control method for inspection robots in narrow spaces. As a concrete example, the chapter describes a pushing force control mechanism for an inspection robot that travels between the rotor and stator of a generator.

Turbine generators installed in power plants are generally maintained through periodic inspections. To improve the availability of generators, reducing the inspection time and extending the inspection interval are essential. Conventional generator inspections require that the rotor be removed from the stator and inspected by certified inspectors. Removing the rotor before the inspection and replacing the rotor after the inspection takes a lot of time[88]. In recent years, robotic inspection technology for generators has advanced to streamline the process. The inspection robot is inserted into the gap between the rotor and stator. While moving through the gap, the inspection is performed by a device mounted on the robot. The introduction of the inspection robot eliminates the processes of removing and replacing the rotor, which is expected to significantly reduce inspection time and cost.

The inspection robot must reach any position in the circumferential and axial directions of the generator; however, the gravity on the robot varies with its position. To prevent the inspection robots from falling in a narrow space, the mechanisms of the robots can be classified into two main types. One is a magnet type model, which moves on the inner surface of the stator while sticking to the stator by magnetic force[59–62]. The other is a pushing type model, which moves over the rotor while pushing the

stator with its arm. The magnet type mechanism utilizes a permanent magnet, and the magnetic force generated between the magnet and stator iron core is used to prevent dropping. A permanent magnet can produce a large force although its size is small; however, it is difficult to control the magnetic force according to the robot's position in the generator. The problem may be that once the adsorption force is lost, it is difficult to return to the posture. For example, in large generators, a rectifying plate for the cooling gas, referred to as a segregating baffle, is often installed on the stator side. This segregating baffle is an obstacle for a magnet-type robot that runs on the stator side. The inspection robot must move away from the stator surface to avoid the segregating baffle; however, the adsorption force by the magnet cannot be controlled, making it difficult for the inspection robot to return to its posture. Therefore, it is difficult for the magnet-type model to inspect a generator with a segregating baffle. However, the pushing model uses an air cylinder-driven arm to the stator[63]. Therefore, it can flexibly respond to changes in gravity by controlling the pushing force. However, active mechanical elements such as motors and air cylinders stop working and cause the inspection robot to fall if their power (electric power and air) supply is interrupted by an unexpected event, such as an emergency. To overcome the disadvantages, a passive mechanism, such as a spring, must be employed to generate a pushing force even when there is no power. However, it should be noted that the pushing force of a passive system alone varies depending on the structure of the moving object.

Therefore, this chapter proposes a pushing force control mechanism and control method that combines an actuator and a spring, a passive mechanical element. First, two types of pushing force control mechanisms (motor-driven arm and pneumatic-driven arm) were developed, consisting of an arm with a motor and air cylinder and a torsion spring. Next, the pushing force control method for each arm is described. The experimental results demonstrate the force control performance of the proposed pushing force control mechanisms.

This chapter is organized as follows: Section 5.2 presents the turbine generator inspection robot, which is the subject of this chapter. Section 5.3 presents the extrusion control mechanism and control method of the inspection robot. The experiments in Section 5.4 demonstrate the effectiveness of the proposed pushing force control mechanism. This chapter is summarized in Section 5.5.

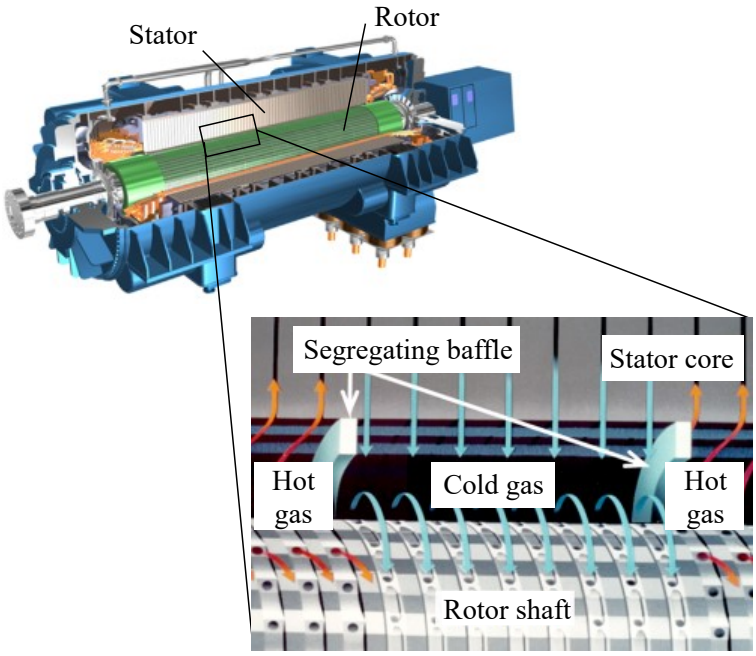

Fig. 5-1: Inner structure of turbine generator.

5.2 Turbine Generator Inspection Robot with Pushing Force Control Mechanisms

5.2.1 Gap Inspection Robot for Turbine Generators

Figure 5-1[1] shows the internal structure of the turbine generator. Because the rotor rotates at a high speed during the generator operation, considerable heat is generated in the narrow gap between the rotor and stator. To maintain the temperature of the generator, the cooling gas flows through the generator. The rotor has many ventilation holes. Cold gas is supplied to the rotor through the ventilation holes. The hot gas is discharged into the stator. To further improve the cooling efficiency, a “segregating baffle” is installed on the inner surface of the stator. The segregating baffle works to regulate the flow of the gas.

The inspection items for the generator are listed in Table 5.1. In the visual inspection, the appearance of the rotor and stator is monitored using images and a video taken by a camera mounted on an inspection robot. Most conventional generator inspection robots are equipped with a camera for visual inspection. Ultrasonic inspection is necessary for the inspection robots to detect cracks in the rotor teeth and wedges that support the rotor coils, which are difficult to find by visual inspection using a camera alone without

[1] Based on reference [89].

Table 5.1: Generator inspection items.

Rotor/Stator	Target	Method	Abnormal case
Rotor	Surface	Visual Test	Burnt deposit
	Ventilating hole	Visual Test	Substances
	Wedge	Ultrasonic Test	Inner defect
Stator	Surface	Visual Test	Burnt deposit
	Wedge	Hammering	Inner defect
	Iron core	EL CID	Break down

removing the rotor. The stator slot wedge tightness is checked by the hammer tapping method. In this method, the inspector checks by listening to the tapping sound of the inspection robot. Electromagnetic core impulse detection (EL CID) is performed to check for interlaminar insulation breakdown in the stator core. In this test, the inspection robot has to press the coil against the stator while a weak current is applied to the stator to measure the leakage current.

Figure 5-2 shows a generator inspection robot equipped with pushing force control mechanisms. As shown in Fig. 5-2 (a), the developed robot consists of a tracking vehicle, sensors to detect the segregating baffle, inspection devices, and pushing force control mechanisms. The pushing force control mechanisms are classified into two types of arms: motor-driven arms and pneumatic-driven arms. The robot moves on the rotor while supporting the body with each arm. Figure 5-2 (b) shows a scene in which the robot moves through the gap between the rotor and stator. When the sensor detects the segregating baffle, the robot folds and unfolds its arms to avoid it. This drive system allows the inspection of generators with separate baffles. The motor-driven arm is spring-loaded to push against the stator even when it is not powered, thus, it will not fall into the generator even if the power is lost. Another mechanism transports the inspection robot. This mechanism moves in the circumferential direction of the rotor and is mounted on the rotor surface. The robot moves while controlling its posture and the lateral displacement during the forward and backward motion using an algorithm that detects the slots in which coils are embedded in the iron core on the stator side. Therefore, the robot can move along the slot at any position in the gap.

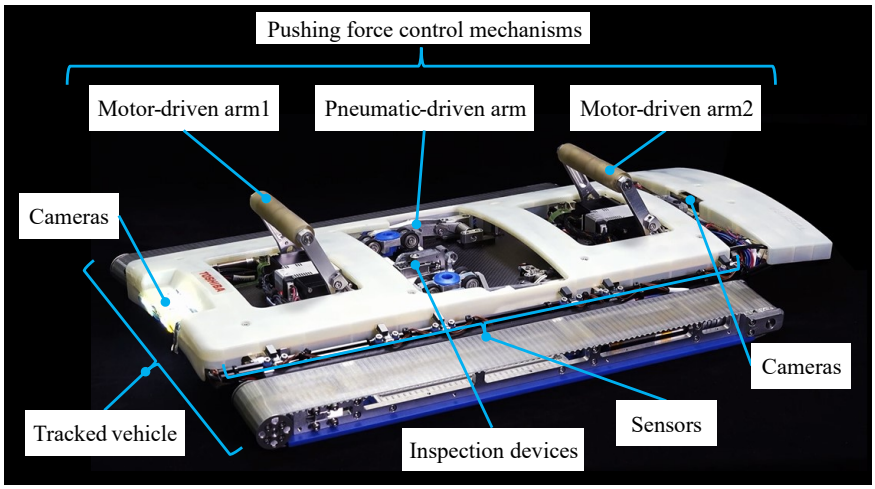

(a) Appearance.

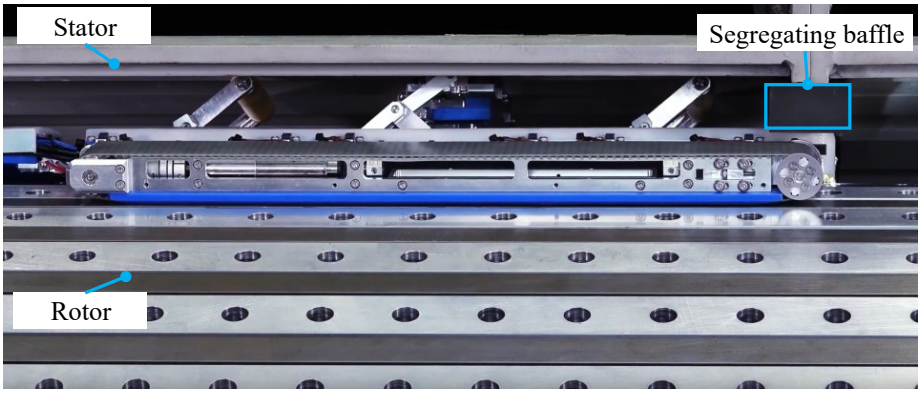

(b) Situation in the gap.

Fig. 5-2: Generator inspection robot with pushing force control mechanisms.

5.3 Pushing Force Control Mechanisms and Control Methods

5.3.1 Pushing Force Control Mechanisms

The motor- and pneumatic-driven arms are essentially used to push and follow the inner surface of the stator to support the robot. Additionally, the pneumatic-driven arm plays a role in transferring the inspection device. For example, the inspector checks the appearance of the stator surface using images captured by the camera. The stator slot wedge tightness is inspected by hitting the wedge with a hammer and checking the sound collected by the microphone. EL CID is performed to detect interlayer insulation breakdown in the stator coil. The pneumatic-driven arm pushes the inspection equipment, such as the tapping hammer and EL CID coil, against the inner surface of the stator. The pushing force on the stator by each arm needs to be controlled. In this chapter, a force control system is designed based on the model of each arm.

5.3.2 Modeling of Pushing Force Control Mechanisms

Figure 5-3 shows the model of the robot with the pushing force control mechanisms. The parameters of Fig. 5-3 are listed in Table 5.2. In this model, each arm is a quality point model. The motor-driven arm is configured using a torsion spring to automatically unfold the arm when the power supply to the robot is interrupted. On the other hand, the pneumatic-driven arm is set using a torsion spring to fold the arm to prevent damage to the inspection system in case of power loss. From Fig. 5-3 (a) and (b), the equation of motion of the robot in the x-direction is expressed as follows:

$$m\ddot{x} = f_d - \mu_1 N_0 - \mu_2(N_1 + N_2 + N_3). \tag{5.1}$$

The relationship between the normal force from the rotor and that from the stator is expressed as follows:

$$N_0 = N_1 + N_2 + N_3 + mg\cos\alpha. \tag{5.2}$$

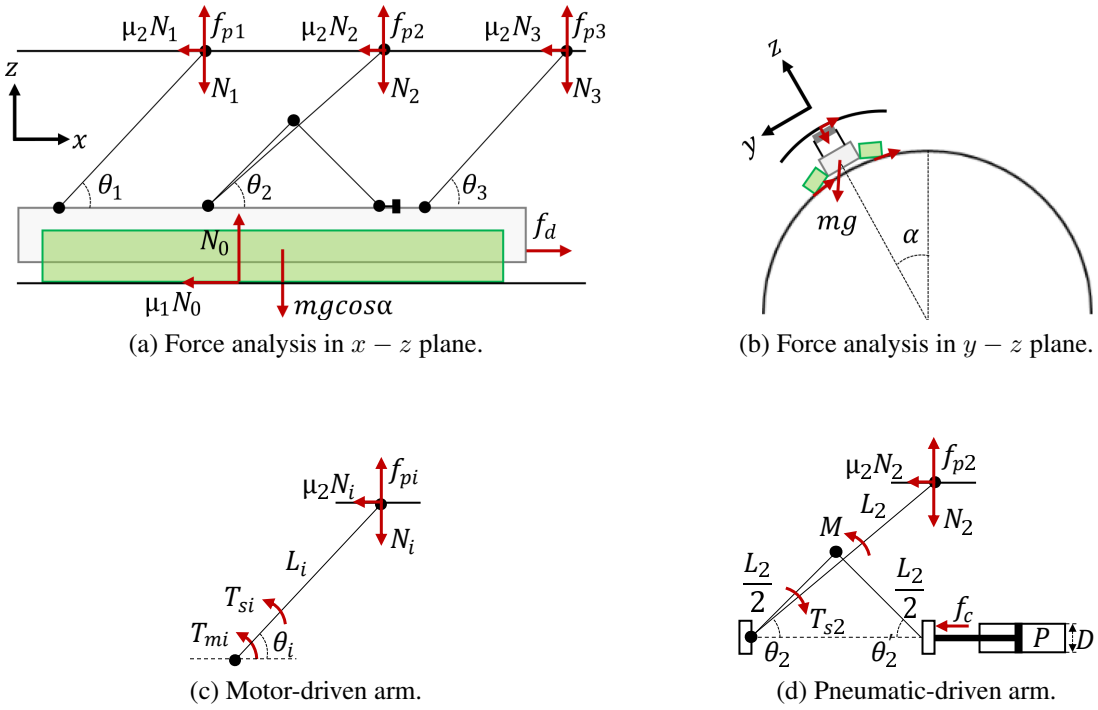

(a) Force analysis in $x - z$ plane.

(b) Force analysis in $y - z$ plane.

(c) Motor-driven arm.

(d) Pneumatic-driven arm.

Fig. 5-3: Model of generator inspection robot.

5.3.3 Force Control of Pushing Force Control Mechanisms

Force Control of Motor-driven Arm

Figure 5-3 (c) shows a model of the motor-driven arm. The pushing force on the stator by the motor-driven arm, $f_{pi}(i = 1, 3)$, is expressed as follows:

$$\begin{aligned} f_{pi} &= \frac{T_i}{L_i \cos\theta_i}, \\ &= \frac{T_{si}(\theta_i) - T_{mi}}{L_i \cos\theta_i}. \end{aligned} \tag{5.3}$$

The elastic torque $T_{si}(\theta_i)$ by the spring depends on the angle θ_i of the arm. To control the pushing force so that it follows the force command f_{pi}^{cmd}, the torque control reference T_{mi}^{ref} of the motor is calculated as follows:

$$T_{mi}^{ref} = T_{si}(\theta_i) - f_{pi}^{cmd} L_i \cos\theta_i. \tag{5.4}$$

Table 5.2: Parameters in Fig. 5-3.

Parameter	Description
f_d	Driving force by the tracked vehicle
m	Mass of the robot
g	Gravitational acceleration
α	Angle from the top of the rotor to the robot position
N_0	Normal force from the rotor to the robot
N_1	Normal force from the stator to the motor-driven arm1
N_2	Normal force from the stator to the pneumatic-driven arm
N_3	Normal force from the stator to the motor-driven arm2
L_1	Length of the motor-driven arm1
L_2	Length of the pneumatic-driven arm
L_3	Length of the motor-driven arm2
θ_1	Angle of the motor-driven arm1
θ_2	Angle of the pneumatic-driven arm
θ_3	Angle of the motor-driven arm2
T_{m1}	Motor torque of the motor-driven arm1
T_{m2}	Motor torque of the motor-driven arm2
T_{s1}	Elastic torque by the spring to the motor-driven arm1
T_{s2}	Elastic torque by the spring to the pneumatic-driven arm
T_{s3}	Elastic torque by the spring to the motor-driven arm2
μ_1	Friction coefficient of the rotor surface
μ_2	Friction coefficient of the inner surface of the stator
P	Internal pressure of the pneumatic cylinder
D	Inner diameter of the pneumatic cylinder
f_c	Thrust force by the pneumatic cylinder
f_{p1}	Pushing force by the motor-driven arm1
f_{p2}	Pushing force by the pneumatic-driven arm
f_{p3}	Pushing force by the motor-driven arm2
M	Moment generated by the thrust force

Force Control of Pneumatic-driven Arm

Figure 5-3 (d) is a model of the pneumatic-driven arm. The relationship between θ_2 and θ_2' is geometrically $\theta_2' = \theta_2 + 2.0$ degrees from the design drawing. The electro-pneumatic regulator controls the

internal pressure P, and the thrust force f_c in the extrusion direction is expressed as follows:

$$f_c = \frac{\pi D^2}{4} P. \tag{5.5}$$

When the pushing force by the cylinder is defined as f_2, it is expressed with the moment caused by the cylinder M as follows:

$$f_2 = \frac{M \cos\theta_2}{L_2}. \tag{5.6}$$

From the law of action-reaction, the moment M is expressed using the thrust force f_c as follows:

$$M = \frac{L_2 f_c}{2 \sin\theta_2'}. \tag{5.7}$$

By substituting (5.7) into (5.6), the relation between the pushing force by the cylinder f_2 and thrust force f_c is obtained as follows:

$$f_2 = \frac{f_c \cos\theta_2}{2 \sin\theta_2'}. \tag{5.8}$$

The torque generated by the spring is converted to the pulling force at the top of the pneumatic-driven arm. When the pulling force is defined as f_{s2}, it is computed as follows:

$$f_{s2} = \frac{T_{s2}(\theta_2)}{L_2 \cos\theta_2}. \tag{5.9}$$

Therefore, when the pneumatic-driven arm contacts the inner surface of the stator, the pushing force by the pneumatic-driven arm to the stator is expressed as follows:

$$\begin{aligned} f_{p2} &= f_2 - f_{s2}, \\ &= \frac{f_c \cos\theta_2}{2 \sin\theta_2'} - \frac{T_{s2}(\theta_2)}{L_2 \cos\theta_2}. \end{aligned} \tag{5.10}$$

From (5.10), it can be inferred that the pushing force depends on the angle of the arm, and it changes non-linearly. To mitigate the effect of the non-linearity, the control reference of the thrust force f_c^{ref} is computed using the pushing force command f_{p2}^{cmd} as follows:

$$f_c^{ref} = \frac{2 \sin\theta_2'}{\cos\theta_2} \left(f_{p2}^{cmd} + \frac{T_{s2}(\theta_2)}{L_2 \cos\theta_2} \right). \tag{5.11}$$

When the controller is designed based on the model, it should be considered that the control performance deteriorates by the modeling error and other disturbances such as the friction force inside the cylinder.

Table 5.3: Procedures for identification of the disturbance model.

No.	Procedure
1	Compute Δf_{p2} using the difference between the experimental value and the theoretical of f_{p2}
2	Provided that Δf_{p2} as a formula of $a(\theta_2)$, compute Δf_c from the inclination of the approximation straight line.
3	Provided that the difference between the experimental value of f_{p2} and $\Delta f_c a(\theta_2)$ as a formula of $f_c + \Delta f_c$, compute $\Delta a(\theta_2)$ and $\Delta b(\theta_2)$ from the inclination and the intercept of the approximation straight line, respectively.

Therefore, in this chapter, the disturbance model is designed. The identified parameters of the model are then used to compensate for the disturbance. To simplify the discussion, (5.10) is redefined as follows:

$$\begin{aligned} f_{p2} &= a(\theta_2) f_c + b(\theta_2), \\ a(\theta_2) &\triangleq \frac{\cos\theta_2}{2\sin\theta_2'}, \\ b(\theta_2) &\triangleq -\frac{T_{s2}(\theta_2)}{L_2\cos\theta_2}. \end{aligned} \tag{5.12}$$

Considering the disturbance to the pushing force f^{dis}, (5.12) is updated as follows:

$$\begin{aligned} f_{p2} + f^{dis} = (a(\theta_2) + \Delta a(\theta_2))(f_c + \Delta f_c) \\ + b(\theta_2) + \Delta b(\theta_2). \end{aligned} \tag{5.13}$$

Here, it is assumed that θ_2 is measured with enough precision, and the arm length L_2 and torque coefficient of the spring are equal to the design values. In (5.13), f^{dis}, $\Delta a(\theta_2)$, Δf_c, and $b(\theta_2)$ denote the disturbance to the pushing force, the disturbance which changes owing to the angle of the arm, the disturbance regarding the cylinder such as the inner friction, and the other disturbance, respectively. From (5.12) and (5.13), the disturbance model is obtained as follows:

$$f^{dis} = \Delta f_c a(\theta_2) + \Delta a(\theta_2)(f_c + \Delta f_c) + \Delta b(\theta_2) \tag{5.14}$$

Each parameter of the disturbance model is identified by the procedures listed in Table 5.3. Based on the identified parameters of the disturbance model, the estimated disturbance $\hat{f}^{dis}$ is obtained as follows:

$$\hat{f}^{dis} = \Delta a(\theta_2)(f_c + \Delta f_c) + \Delta b(\theta_2). \tag{5.15}$$

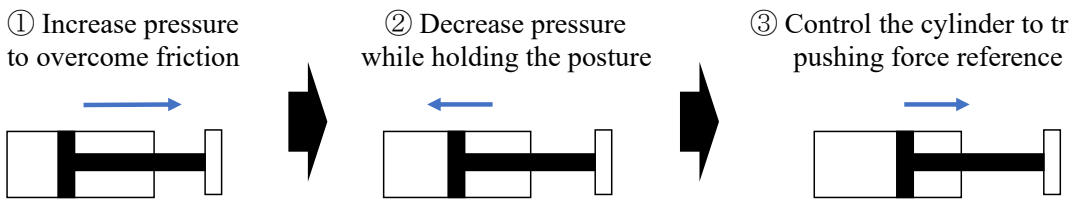

Fig. 5-4: Flow of the initial motion control process.

With the compensation of the estimated disturbance, the force control reference is obtained as follows:

$$f_c^{ref} = \frac{2\sin\theta_2'}{\cos\theta_2}\left(f_{p2}^{cmd} + \frac{T_{s2}(\theta_2)}{L_2\cos\theta_2} - \hat{f}^{dis}\right). \tag{5.16}$$

From (5.16), it can be inferred that the larger the angle of the pneumatic-driven arm θ_2, the smaller the control reference f_c^{ref}. In other words, when the angle of the arm is large, it can be expected that the thrust force is not large enough to overcome the static friction inside the cylinder. As a countermeasure for this issue, an initial motion control process is added to the control system. The flow of the initial motion control process is shown in Fig. 5-4. In the initial motion control process, a feed-forward pressure input is first added to the control reference before the cylinder moves. The pressure of the cylinder is then decreased to exhaust the inner pressure of the cylinder while holding the posture of the arm. Finally, the pushing force control reference in (5.16) is applied. By the initial motion control process, the direction of the thrust force can always be controlled to be constant.

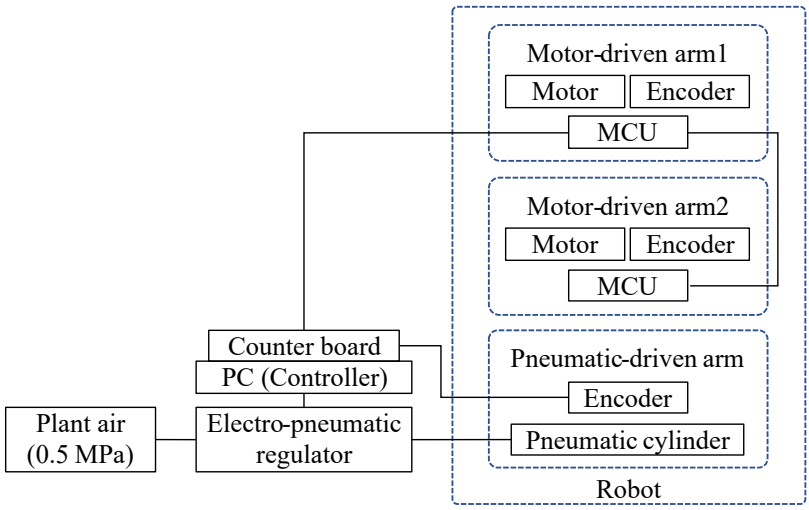

Fig. 5-5: Control system configuration of the pushing control mechanisms.

5.4 Experimental Evaluation of Pushing Force Control Mechanisms

In this section, the experimental results confirm the pushing force control performance of each arm.

5.4.1 Experimental Conditions

In the experiments, the arms installed on the developed robot were used. The control system configuration of the arms is shown in Fig. 5-5. In the experiments, the force command is set to the controller; the computed control references are then transferred to the motors' micro controller units (MCUS) and the electro-pneumatic regulator. Figure 5-6 shows the experimental setup. A force gauge was used to measure the pushing force by each arm. The equipment specifications of the experimental setup are listed in Table 5.4.

Experimental Conditions of Motor-driven Arm

For the motor-driven arms, while the angle of the arm (θ_1 or θ_3) is fixed to 45 deg, the force command was changed by 5 N to increase the pushing force.

Experimental Conditions of Pneumatic-driven Arm

For the pneumatic-driven arm, the force command was applied when the pneumatic-driven arm was folded. By the thrust force by the cylinder, the pneumatic-driven arm was unfolded and it pushed the

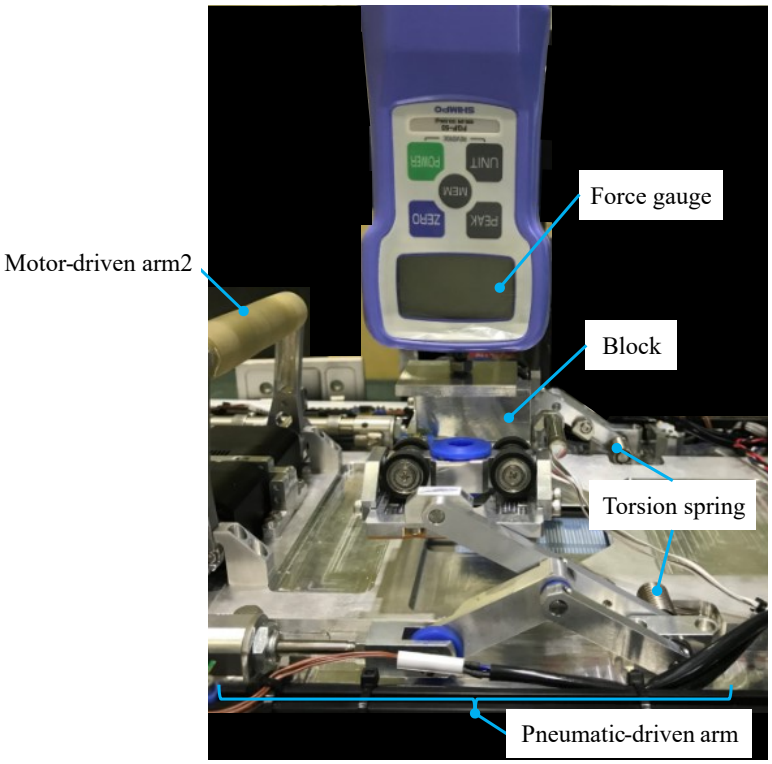

Fig. 5-6: Experimental setup.

force gauge. The experiments were conducted with different arm angles ($\theta_2 = 13$, 28, and 53 deg). The angles were adjusted by placing a block between the force gauge and pneumatic-driven arm. The force command was between 10 to 30 N by 1 N. From the experimental results, the effects of the disturbance compensation and initial motion control process were observed.

5.4.2 Experimental Results

Experimental Results of Motor-driven Arm

Figure 5-7 shows the experimental results of the motor-driven arms. In Fig. 5-7, the circle dots and dashed lines denote the measured data and ideal lines, respectively. From Fig. 5-7, in both motor-driven arms, the measured pushing force seems to follow the ideal line. Therefore, the validity of the pushing control method for the motor-driven arm was confirmed.

Table 5.4: Specifications of the experimental setup.

Specification	Value
Measurement range of force gauge	± 500 N
Resolution of force gauge	0.1 N
Resolution of electro-pneumatic regulator	10 bit
Inner diameter of the pneumatic cylinder D	16 mm
Torsion spring constant of the motor-driven arm	10.7 Nmm/deg
Torsion spring constant of the pneumatic-driven arm	2.5 Nmm/deg
Initial angle of the motor-driven arm	114 deg
Initial angle of the pneumatic-driven arm	-70 deg
Length of the motor-driven arm L_1, L_3	40 mm
Half the length of the pneumatic-driven arm L_2	43 mm

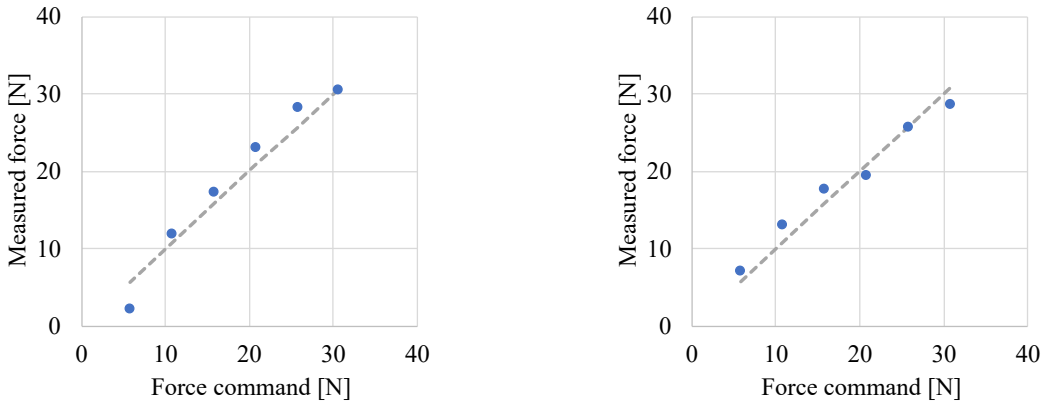

(a) Motor-driven arm1. (b) Motor-driven arm2.

Fig. 5-7: Experimental results of the motor-driven arms.

Experimental Results of Pneumatic-driven Arm

Figure 5-8 shows the experimental results of the pneumatic-driven arm to evaluate the disturbance compensation. In Fig. 5-8, the circle markers represent the results without the disturbance compensation, and the square markers represent the results with the disturbance compensation. The dashed lines represent the ideal force response. From this figure, the force response became close to the ideal response by the disturbance compensation. However, it should be noted that the force response was 0 when the force input was small because the thrust force did not overcome the static friction inside the cylinder.

Figure 5-9 shows the experimental results of the pneumatic-driven arm to evaluate the initial motion control process. In Fig. 5-9, the circle markers represent the results without the initial motion control

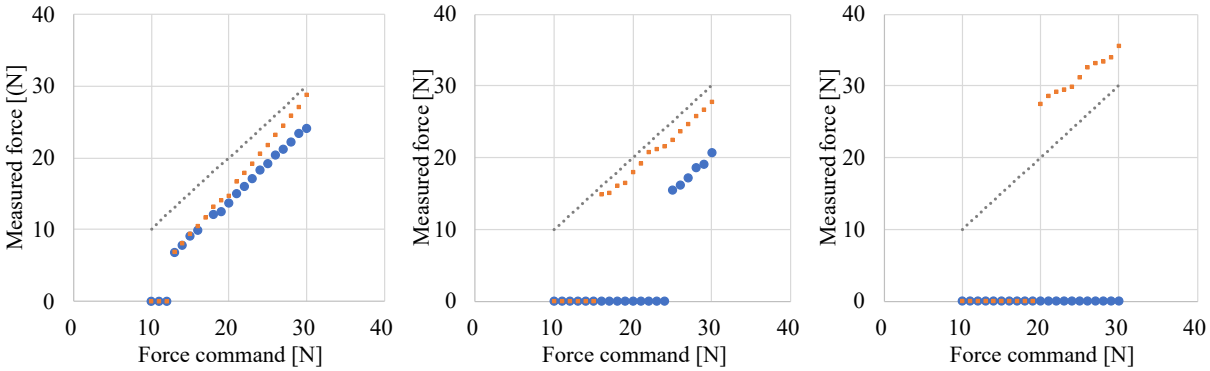

(a) 13 deg. (b) 28 deg. (c) 53 deg.

Fig. 5-8: Experimental results to confirm the effects of the disturbance compensation

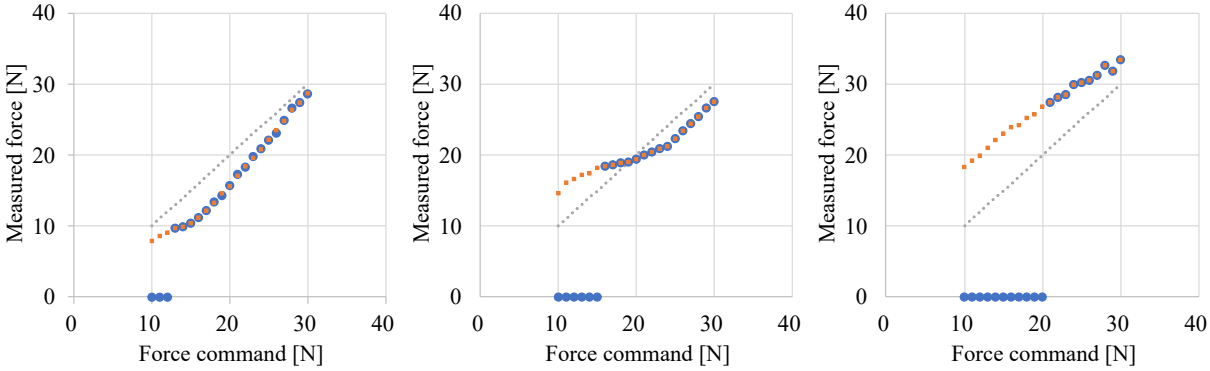

(a) 13 deg. (b) 28 deg. (c) 53 deg.

Fig. 5-9: Experimental results to confirm the effects of the initial motion control process.

process, and the square markers represent the results with the initial motion control process, respectively. From Fig. 5-9, it can be inferred that the initial motion control process improved the force response. From these results, the validities of the pushing control methods for the pneumatic-driven arm were confirmed.

5.5 Summary

This chapter presents the pushing force control mechanisms to maintain the posture in a narrow space. The proposed pushing force control mechanism consists of an actuator such as a motor or air cylinder and a passive mechanical element. Model-based control methods were proposed for the motor- and pneumatic-driven arms, respectively. Particularly, because the force control using a general air cylinder is significantly affected by external disturbances, the proposed method uses a pre-estimated disturbance model for compensation. The pushing force control performance of the motor- and pneumatic-driven arms was confirmed through experiments.

This chapter discusses a specific example of an inspection robot that travels and inspects the gap between the rotor and stator of a turbine generator. With the proposed pushing force control mechanisms, the inspection robot can support its body inside the generator and maintain its posture without falling even in an emergency. Additionally, by folding and unfolding the arms in sequence while changing the pushing force, the inspection robot can pass through the segregating baffle. In this chapter, the pushing force control was considered for the primary purpose of the posture maintenance, but in practice, the pushing force is often related to the driving force of the moving mechanism. Therefore, it is necessary to consider the driving force in setting the actual pushing force. The proposed pushing force control mechanism is applicable not only to robots for inspecting power generators but also to all robots that move in a narrow space while restraining themselves by pushing.

Chapter 6

Force-based Diagnosis of Structural Internal State

6.1 Introduction

This chapter presents a device and method for the percussion inspection of the internal state of a structure using reaction forces from the structure. The chapter takes the wedge loosening inspection of a generator stator as a concrete example to illustrate the application of the proposed device and inspection method.

Inspection methods for generators include the visual inspection of the rotor and stator by expert inspectors and percussion inspection, which detect internal defects in the stator by striking the stator surface with a hammer or other striking devices and evaluating the reverberation vibration such as the sound, acceleration, and force from the inside[64]. However, because the gap between the rotor and stator of a regular turbine generator is approximately 40 to 200 mm, the inspection robot must be thin to move through the gap. Therefore, the camera for visual inspection and the device for percussion inspection mounted on the inspection robot must meet the constraints of the robot's portable size, payload, and layout. Generally, inspection robots that perform percussion inspection use separate devices, such as a hammer and microphone, to conduct the sensing functions of percussion and reverberation[65]. If a single device can achieve the striking and reverberation sensing functions, the percussion inspection device can be compacted to a size mountable on the inspection robot, and the restriction on the sensor placement can be solved. Therefore, this chapter first proposes a percussion inspection device that considers the reaction force given to the striking device when the stator surface is struck as a form of reverberant

vibration and realizes the striking function and sensing function of reverberant vibration with a single device. In the past, a mechanism using electromagnets was reported. It is helpful from the viewpoint of compactness and high power to realize the striking function[66]. However, electromagnets generate heat owing to long-term operation, and it is difficult to control the impact force even when a constant current is applied. In the proposed percussion inspection device, a small motor is controlled by force to ensure a constant percussion force. When striking using a force-controlled motor, the reaction force from the struck object becomes a disturbance to the motor. Therefore, by applying the disturbance observer (DOB)[48, 49], a robust force control system can be achieved, and the necessary striking force can be generated. Additionally, the reaction force observer (RFOB) [71] is applied to the proposed percussion inspection device to implement the reaction force-sensing function without using additional sensors such as load cells. As examples of the use of the RFOB, a method to estimate the position where the flexible arm contacts the environment[97] and a method to detect chattering vibration during end milling were reported[98, 99]. A case study was also conducted applying the estimated force information to the leak inspection of packaging materials[100, 101]. However, estimated force information has not been used as an index for inspecting structures as in this dissertation.

Additionally, this chapter proposes a method for detecting wedge loosening in a generator stator by estimating the internal structure model parameters of the stator based on the input/output characteristics of the percussion inspection device and evaluating the fixation of the internal components of the stator. Basic experiments are conducted to evaluate the feasibility of the reaction force estimation function and the inspection method of the proposed percussion inspection device.

This chapter is organized as follows: In Section 6.2, the outline and issues of wedge loosening inspection in generators, which are the specific targets of this research are presented. Section 6.3 describes the structure of the proposed percussion inspection device, control method, and proposed method of detecting wedge loosening using the device. The experimental results of the proposed percussive inspection device are presented in Section 6.4. Finally, the conclusion of this chapter is presented in Section 6.5.

6.2 Issues in Rationalization of Generator Stator Wedge Loosening Inspection

Figure 6-1 shows a cross-sectional schematic diagram of the generator stator perpendicular to the axial direction. As shown in Fig. 6-1(a), the stator is arranged concentrically with the rotor. The stator iron core has a plurality of slots along the inner circumference of the iron core; a wedge seals each slot. Figure 6-1(b) shows a cross-sectional view of one slot of the iron core. Coils are inserted into each slot, and a wedge is pressed into the top of the coil. In many generators, spacers made of corrugated springs are laminated between the iron core, coil, and wedge. The coil is firmly fixed by the elastic force of the corrugated spring generated by the press-fitted wedge. By fixing the coil to the iron core with the wedge, the coil's vibration during operation is suppressed, and the heat generated by the coil is transmitted to the iron core for dissipation. When the wedge loosens because of the long-term operation of the generator, the vibration of the wire forming the coil causes insulation breakdown between the coil surface and iron core. It also degrades the thermal radiation performance of the coil[102]. Therefore, the inspection of the stator wedge looseness is an essential item to maintain and control the generator's performance from the viewpoint of electrical and thermal radiation.

In the conventional wedge loosening inspection, a specialist inspector strikes the wedge by a hammer with a force of several N orders and perceives the sound and vibration by hearing and force, respectively. The wedge loosening was detected by the relative evaluation of the information from multiple locations. However, from the viewpoint of the automation of percussion and vibration inspection of infrastructure facilities such as bridges, the main focus has only been on information processing methods for reverberant vibration, such as sound[25, 26, 103] and acceleration[104] obtained by striking and eddy currents

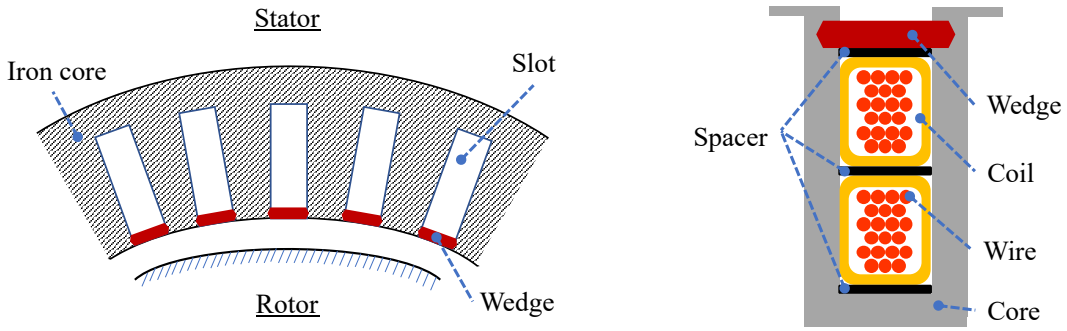

(a) Stator iron core. (b) Stator slot.

Fig. 6-1: Cross-sectional schematic diagram of a generator.

during magnetic field irradiation[105]. Practically, the excitation of reverberation depends on the striking method and striking force, thus, the striking force should be controlled quantitatively for consistent inspection. Additionally, sound, which is information in the high-frequency band, is used to inspect large structures such as infrastructure facilities, but requires additional microphones.

The force can be detected in a lower frequency band than sound, but the target wedge is maximum of a few hundred millimeters. Additionally, the force information in the frequency range of 0 to 400 Hz is similar to that of human force perception. The force information in the frequency range of 0∼400 Hz can be perceived more sensitively by the mechanoreceptors of human force perception; thus, it may be possible to identify wedge loosening based on the force information below 400 Hz. Furthermore, because the force is generated at the point of contact between the hammer and wedge, there is no need to consider disturbances from the surroundings. Therefore, to achieve the same level of wedge loosening inspection as the conventional ones, the proposed device is designed to acquire force information with a frequency band of 400 Hz or higher without controlling the impact force on the order of several N and without requiring additional sensors. Additionally, a method of detecting stator wedge loosening using the acquired force information is evaluated.

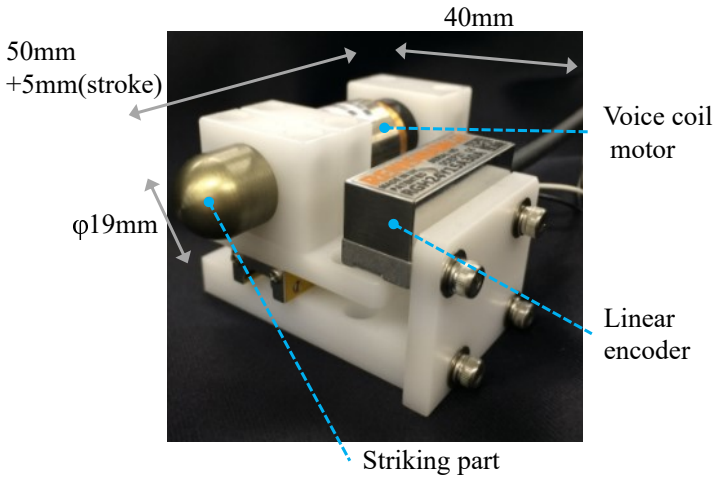

Fig. 6-2: Structure of force sensor less percussion inspection device.

Table 6.1: Components of proposed percussion inspection device.

Component	Type	Manufacturer
Voice coil motor	AVM19-5	Akribis Systems Pte Ltd, Singapore
Linear encoder	RGH24Y15A30A	Renishaw plc, England

6.3 Proposed Percussion Inspection Devices

6.3.1 Configuration of Percussion Inspection Device

Figure 6-2 shows the configuration of the proposed percussion inspection device. Table 6.1 lists the components of the percussion inspection device. In the proposed percussion inspection device, a small voice coil motor is used as the actuator. The motor is driven according to the applied current, and a linear encoder measures the motor displacement. The motor displacement is used to calculate the velocity input of the DOB and RFOB, briefly described in Chapter 2.

In the proposed percussion inspection device, the percussion function is achieved by controlling the force so that the motor can provide the intended action force to the object. When the motor is in contact with the object, the action-reaction relationship is established, and the motor is subjected to the object's reaction force. The reaction force reflects the characteristics of the object, and the proposed percussion inspection device is characterized by its ability to estimate the reaction force as information on the reverberation vibration without a force sensor.

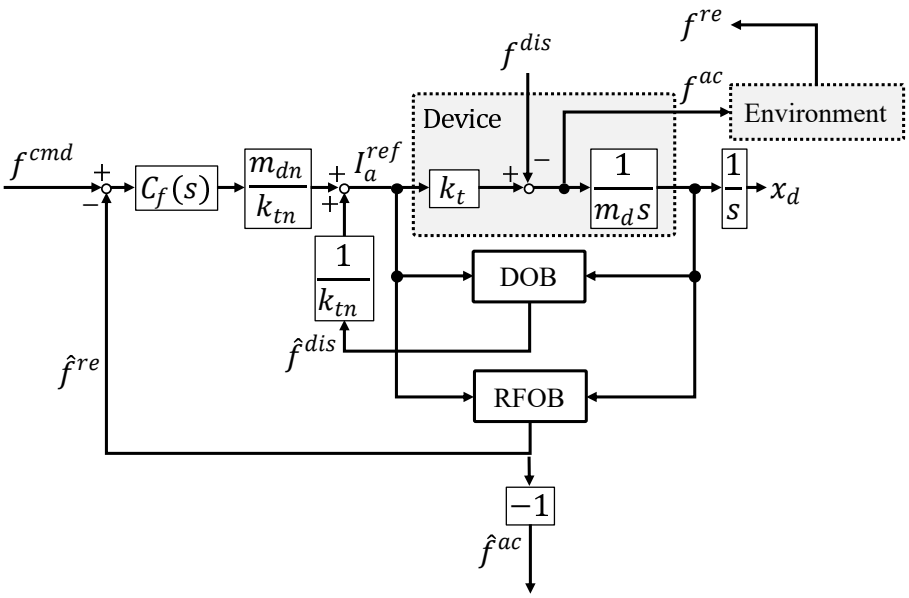

Fig. 6-3: Force control system for percussion inspection device.

Table 6.2: Parameters of force control system

Parameter	Description
f^{cmd}	Force command
f^{dis}	Disturbance force
f^{ac}	Action force
f^{re}	Reaction force
I_a^{ref}	Current reference
x_d	Position of device
m_d	Mass of devicer
k_t	Thrust coefficient
$C_f(s)$	Force controller
$\hat{}$	Estimated value
$_n$	Nominal value

6.3.2 Control system for Percussion Inspection Device

Figure 6-3 shows the control system of the proposed percussion inspection system. The symbols in Fig. 6-3 are listed in Table 6.2. The control system of the proposed percussion inspection device consists of the force controller $C_f(s)$ to control the impact force, the DOB to make the force control system robust, and the RFOB to estimate the reaction force. By compensating using the DOB, disturbances

below the cutoff frequency of the DOB can be suppressed among the disturbances given to the motor during strikes, making the control system more robust. Similarly, it is possible to estimate the reaction force below the cutoff frequency of the RFOB. Therefore, it is a prerequisite for the inspection method using the estimated reaction force that the virtual model inside the slot described below is a system with the following resonance frequencies. In Chapter 2, it was mentioned that disturbances other than the reaction force, such as friction and interaction forces, must be identified to use the RFOB. However, because the proposed percussion inspection device uses a low sliding voice coil motor, the modeling error and kinetic friction force can be sufficiently ignored. From the action-reaction relationship, the estimated striking force $\hat{f}^{ac}$ is obtained as follows:

$$\hat{f}^{ac} = -\hat{f}^{re}. \tag{6.1}$$

In the proposed percussion inspection device, the force controller $C_f(s)$ is designed with the proportional (P) gain K_{fp} as follows:

$$C_f(s) = K_{fp}. \tag{6.2}$$

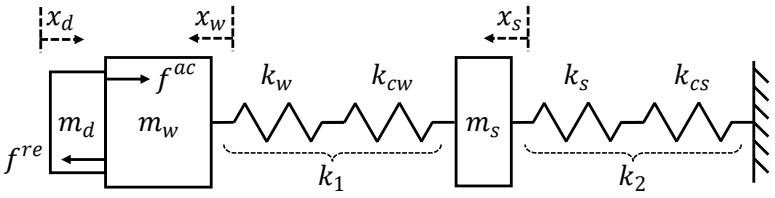

Fig. 6-4: Slot state model.

Table 6.3: Parameter of slot state model.

Parameter	Description
m_w	Mass of wedge
k_w	Stiffness of wedge
x_w	Position of wedge
m_s	Mass of spacer
k_s	Stiffness of spacer
x_s	Position of spacer
k_{ws}	Connectivity of wedge
k_{cs}	Connectivity spacer
k_1	Synthetic stiffness of k_w and k_{cw}
k_2	Synthetic stiffness of k_s and k_{cs}

6.3.3 Wedge Looseness Inspection Method Using Percussion Inspection Device

The information inside the wedge and slot is modeled, and the wedge loosening inspection method based on the input/output characteristics of the vibration inspection device is discussed.

Modeling of Inner Slot State

Generally, wedges and spacers are designed to increase their stiffness to secure the high-weight stator coils in the slots. Hence, the stiffness and inertia are dominant when considering the representation of the wedge and spacer as mechanical elements. Therefore, it is supposed that both the wedge and spacer can be represented by a spring-mass model, which is a linearly coupled vibration model as shown in Fig. 6-4. The symbols in the figure are listed in Table 6.3. In the coupled vibration model shown in the figure, k_{cw} and k_{cs} represent the virtual stiffness of the wedge and spacer connections (fixity), respectively. The mass of the coil connected to the spacer is assumed to be sufficiently large and is treated as a fixed end. Conversely, the mass of the air is assumed to be sufficiently small.

The equation of motion for the coupled vibration model in Fig. 6-4 is as follows:

$$m_s\ddot{x}_s + k_2x_s + k_1(x_s - x_w) = 0, \tag{6.3}$$

$$m_w\ddot{x}_w + k_1(x_w - x_s) = -f^{ac}, \tag{6.4}$$

$$m_d\ddot{x}_d = -f^{re}. \tag{6.5}$$

When the wedge loosens, a void is generated. The displacement of the wedge or spacer against external forces is then expected to increase. Particularly, the virtual stiffnesses k_{cw} and k_{cs} reduce owing to the displacement. Let k be the virtual stiffness obtained by synthesizing the spring models in Fig. 6-4, the virtual stiffness k can be expressed as follows:

$$\begin{aligned} k &= k_1 + k_2 \\ &= \frac{k_w k_{cw}}{k_w + k_{cw}} + \frac{k_s k_{cs}}{k_s + k_{cs}}. \end{aligned} \tag{6.6}$$

The virtual stiffness k determines the magnitude of the elastic force when the coupled vibration model components are displaced. Therefore, it can be inferred that there is a correlation between the virtual stiffness k and loosening of the wedge due to the generation of voids. Based on the considerations, this chapter treats the virtual stiffness k as an index to show how well the wedge fixes the slot. In this chapter, the virtual stiffness k is treated as an index of the slot fixation by the wedge. The policy of the inspection method using the vibration inspection device is to detect the wedge loosening by evaluating the virtual stiffness k.

Transfer Function of Percussion Inspection Device

When the percussion inspection device strikes the wedge and makes contact, the following relationship is established:

$$x_d = -x_w \tag{6.7}$$

When the cutoff frequencies of DOB and RFOB are sufficiently high, the transfer function $G(s)$ from the input f^{cmd} to the percussion inspection device to the estimated reaction force $\hat{f}^{re}$ using the coupled vibration model is expressed by the following equation:

$$\begin{aligned} G(s) &= \frac{\hat{f}^{re}}{f^{cmd}} \\ &= -\frac{C_f(s)k_{tn}}{1 + C_f(s)k_{tn}} \cdot \frac{m_d s^2(m_s s^2 + k_1 + k_2)}{m_w m_s s^4 + (m_w k_1 + m_s k_1 + m_w k_2)s^2 + k_1 k_2}. \end{aligned} \tag{6.8}$$

Table 6.4: Simulation parameters.

Parameter	Value
Nominal thrust coefficient k_{tn}	1.75 N/A
Nominal mass of device m_{dn}	0.243 kg
Force control gain K_p	1.0
Mass of wedge m_w	0.4 kg
Stiffness of wedge k_w	50000 N/m
Mass of spacer m_s	0.03 kg

Table 6.5: Simulation conditions.

Case No.	k_1 [N/m]	k_2 [N/m]	k [N/m]
case1	1000000	1000000	2000000
case2	1000000	10000	1010000
case3	10000	1000000	1010000
case4	10000	10000	20000

The gain characteristics can be obtained by providing the percussion inspection device with force inputs containing multiple frequencies such as step and sweep signals and comparing them to the reaction force. By fitting the gain characteristics of the estimated reaction force to the transfer function $G(s)$ in (6.8), the coupled vibration model parameters can be estimated. This chapter examines the possibility of detecting wedge loosening by evaluating the virtual stiffness k from the estimated parameters.

Simulation of Input/Output Characteristics of Percussion Inspection Devices

For the transfer function $G(s)$ in (6.8), the model parameters were varied to evaluate the gain characteristics in the frequency range of $1 \sim 400$Hz. The parameters used in the simulation and simulation conditions are listed in Tables 6.4 and 6.5, respectively.

Figure 6-5 shows the simulation results. First, when the value of the virtual stiffness k is significant, as in case 1, the peak occurs at a high frequency (approximately 200 Hz). Subsequently, when the value of k_1 or k_2 decreases, as in case 2 or case 3, the value of the virtual stiffness k decreases. Consequently, the resonance frequency shifts to a lower frequency range, and the peak value decreases. Additionally, when the value of the virtual stiffness k is small, as in case 4, two peaks appear at the low and high frequencies. The increase in the void volume affects k_1 or k_2 and decreases the value of the virtual stiffness k. The simulation results suggest that wedge loosening can be detected by evaluating the force

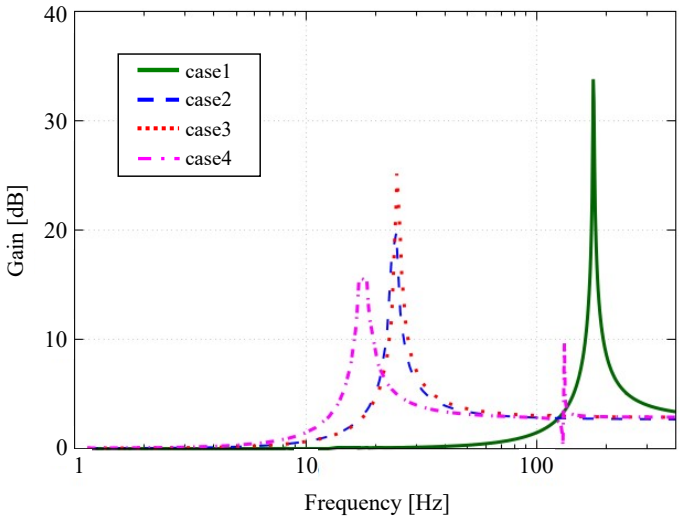

Fig. 6-5: Simulation result.

input-output characteristics and the value of the virtual stiffness k of the percussion inspection device.

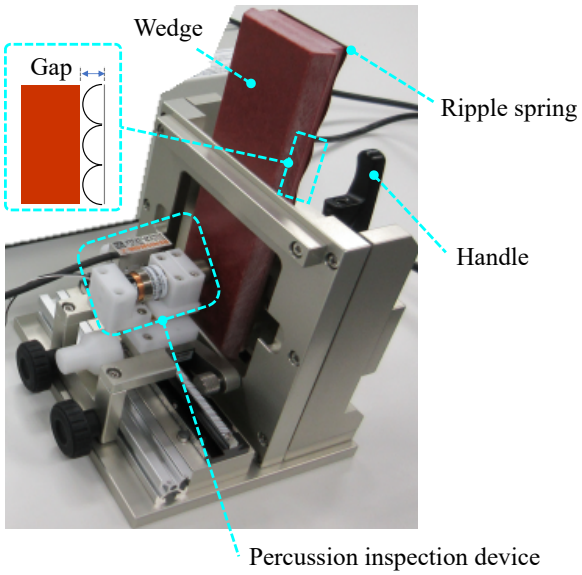

Fig. 6-6: Experimental setup.

6.4 Basic Experimental Evaluation of Proposed Percussion Inspection Device

The validity of the proposed method for inspecting wedge loosening using a percussion inspection device was evaluated through experiments.

6.4.1 Experimental Setup

Figure 6-6 shows the configuration of the experimental apparatus. The inputs to the DOB and RFOB are the current applied to the voice coil motor and motor velocity calculated from its displacement measured by the encoder. In the experimental setup shown in Fig. 6-6, the percussion inspection device is fixed to the table and operates in the direction perpendicular to gravity, thus, the effect of gravity is assumed to be negligible. In this experiment, the stator wedge and spacer (corrugated plate spring) were stacked on top of each other. The tightness of the corrugated plate spring was adjusted by a handle. The wedge was loosened to simulate the gap inside the stator. The control software was written in the C language and operated by RTAI 3.6.1, which is a real-time OS. The control parameters used in the experiment are listed in Table 6.6.

Table 6.6: Experimental parameters.

Descriptions	Value
Nominal torque coefficient k_{tn}	1.75 N/A
Nominal mass of device m_{dn}	0.243 kg
Force control gain K_p	1.0
Cutoff freq. of DOB g_d	3000 ($\simeq 477$) rad/s (Hz)
Cutoff freq. of RFOB g_{rf}	3000 ($\simeq 477$) rad/s (Hz)
Mass of wedge m_w	0.4 kg
Mass of spacer m_s	0.03 kg
Resolution of encoder	0.1 μm
Sampling time	0.5 ms

6.4.2 Functional Evaluation of Percussion Inspection Device

To evaluate the striking and sensing functions of the reverberation vibration of the proposed percussion inspection device, the wedge was struck with the force command f^{cmd} set as follows:

$$f^{cmd} = \begin{cases} 3.0 \text{ N} & (\text{Time} = 1.0 \sim 1.5 \text{ s}) \\ 0 & (\text{otherwise}) \end{cases} \tag{6.9}$$

The force command f^{cmd} and estimated reaction force $\hat{f}^{re}$ were compared.

Figure 6-7 shows the results of the impact experiment. In Fig. 6-7, the dotted and solid lines represent the force command value f^{cmd} and estimated reaction force $\hat{f}^{re}$, respectively. The shaded area represents the time period when the inspection target is being struck. It should be noted that the sign of the estimated reaction force is reversed to simplify the comparison between the force command value and estimated reaction force. From Fig. 6-7, it can be observed that the force command value corresponds to the estimated reaction force, indicating that the intended action force can be applied based on the law of action-reaction. The sudden reaction of the estimated reaction force in the vicinity of 1 s in Fig. 6-7 indicates the impact force at the time of contact. It indicates that sensing in a high-frequency range, including the impact force at the moment of contact, is possible. In conclusion, it was verified that the proposed percussion inspection device could achieve the desired function of striking with the intended action force and sensing the reaction force.

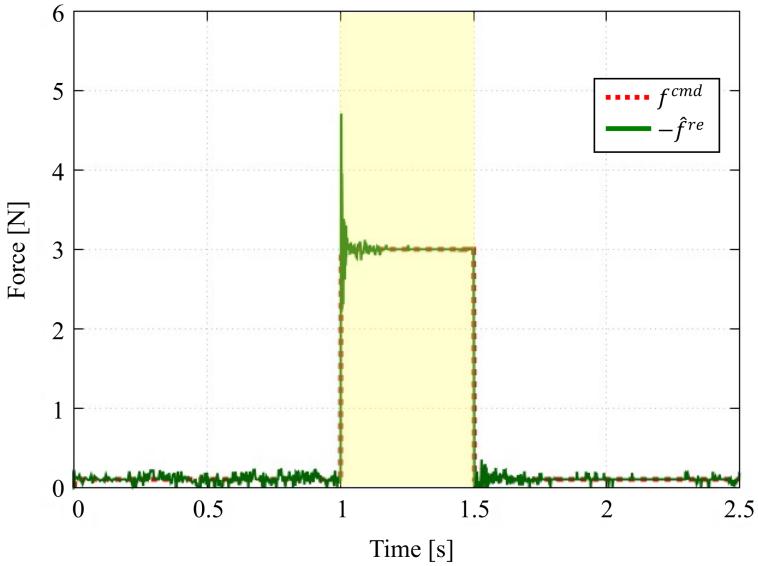

Fig. 6-7: Experimental results for functional verification.

Table 6.7: Force command parameters.

Parameter	Value
Amplitude of f^{cmd} A	1.0 N
Initial value of force command f^{cmd} B	1.5 N
Initial phase ϕ	0 rad
Initial frequency f	0 Hz
Increase rate of frequency k	2.0 Hz
Time t	$0 \sim 200$ s

6.4.3 Experimental Validation of Wedge Loosening Detection Using Percussion Inspection Device

For the validation of the wedge loosening detection method using the percussion inspection device, the test object was vibrated, and the gain characteristics of the action force and estimated reaction force were evaluated. In this experiment, the force command value f^{cmd} shown in the following equation was given to the percussion inspection device:

$$f^{cmd} = A \sin\left[\phi + 2\pi(ft + \frac{k}{2}t^2)\right] + B. \tag{6.10}$$

The values of each parameter in (6.10) are listed in Table 6.7. Table 6.8 lists the amount of void space measured after adjusting the fixed condition of the wedge by the handle.

Table 6.8: Experimental conditions.

Gap [mm]
1.7
1.9
2.2

Figure 6-8 shows the results of the estimated reaction forces obtained from the experiment. From Figs. 6-8(a) and (b), it is confirmed that the estimated reaction force increases slowly, and the peak value decreases as the void becomes larger. Figure 6-8(c) shows that a new peak occurs at approximately 10 s.

Figure 6-9 shows the gain characteristics obtained from the time series data in Fig. 6-8. From Fig. 6-9, it can be observed that the peak value in the high-frequency range (approximately 300 Hz) decreases as the air gap increases. Additionally, a new peak occurs in the low-frequency range (approximately 10 Hz) as the air gap further increases.

Next, the experiments were repeated five times each under the conditions listed in Table 6.8. The values of the coupled vibration model parameters were estimated by fitting the obtained gain characteristics to the transfer function $G(s)$ in (6.8) using the least-squares method. Figure 6-10 shows the relationship between the voids and k_1 and k_2 obtained from the experiments. From Fig. 6-10, it can be observed that k_1 decreases significantly and k_2 increases slightly with the increase of the void volume. This result indicates that the void volume mainly affects the degree of connection between the wedge and spacer. Additionally, the value of the virtual stiffness k is shown in Fig. 6-11. Figure 6-11 shows that the value of the virtual stiffness k decreases as the void volume increases. This indicates that the fixation of the slot by the wedge decreases with the increase of the void volume, which is in line with what was discussed in Section 6.3.3.

As described, in the actual stator wedge loosening inspection, it is possible to detect the presence or absence of voids based on the characteristics of the gain characteristic waveform (number of generated peaks, resonance frequency, and peak value) obtained by hitting the wedge with the proposed vibration inspection device. Additionally, by identifying the value of the virtual stiffness, which consists of the parameters of the coupled vibration model, the presence or absence of voids can be detected. Furthermore, the degree of wedge loosening can be quantified by identifying the value of virtual stiffness, consisting of coupled vibration model parameters.

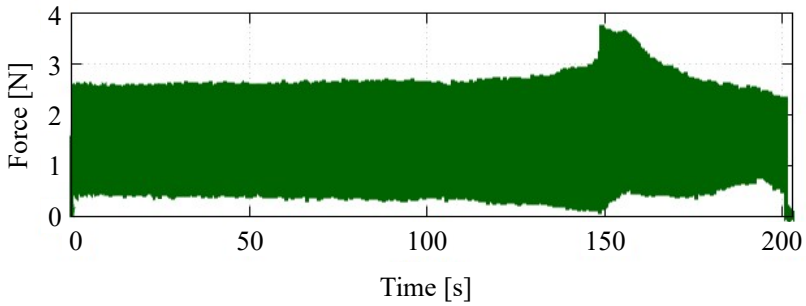

(a) Gap: 1.7 mm.

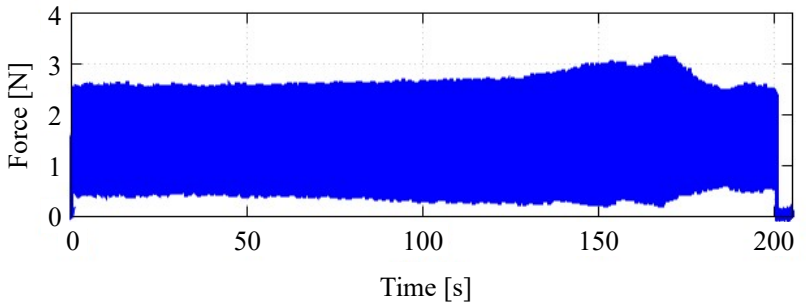

(b) Gap: 1.9 mm.

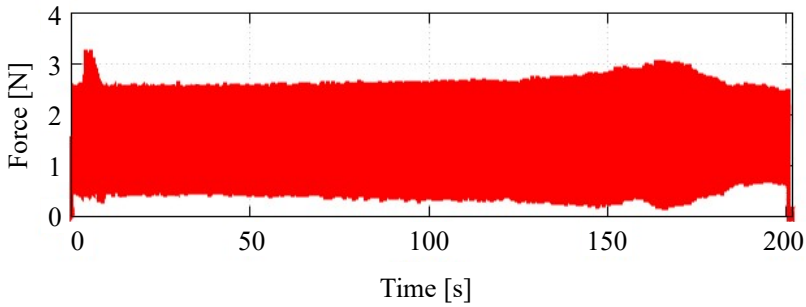

(c) Gap: 2.2 mm.

Fig. 6-8: Experimental results of excitation method.

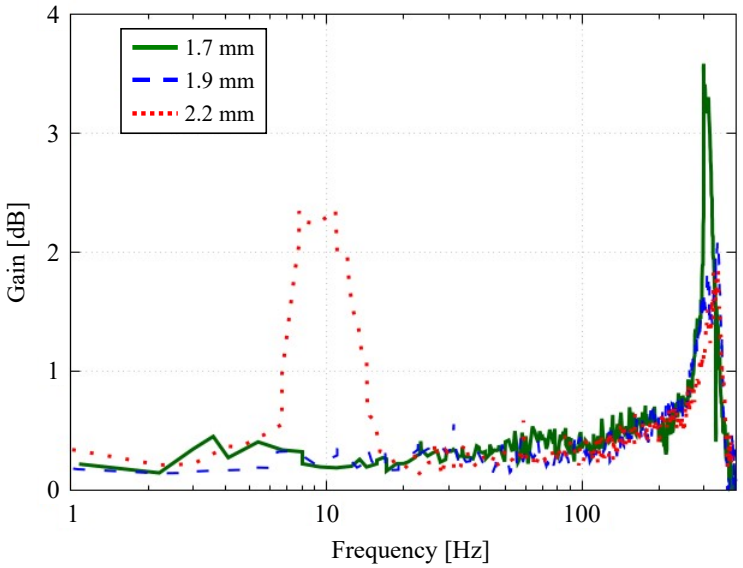

Fig. 6-9: Gain characteristics.

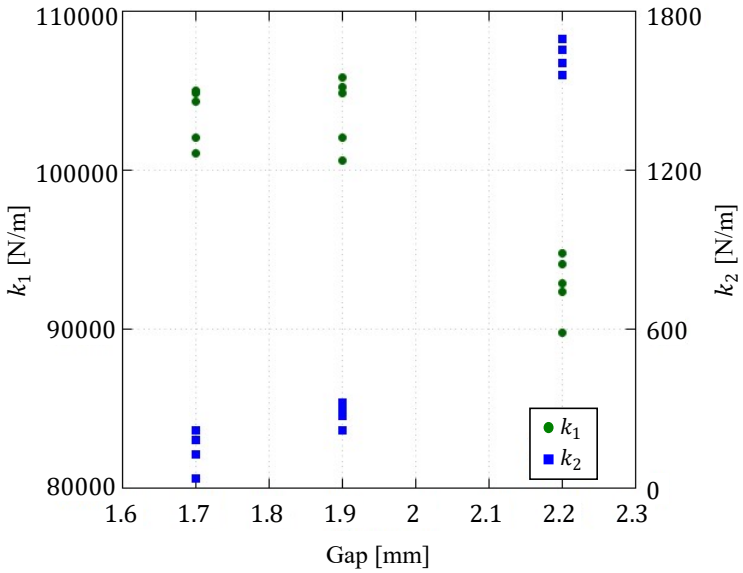

Fig. 6-10: Estimated value of k_1 and k_2.

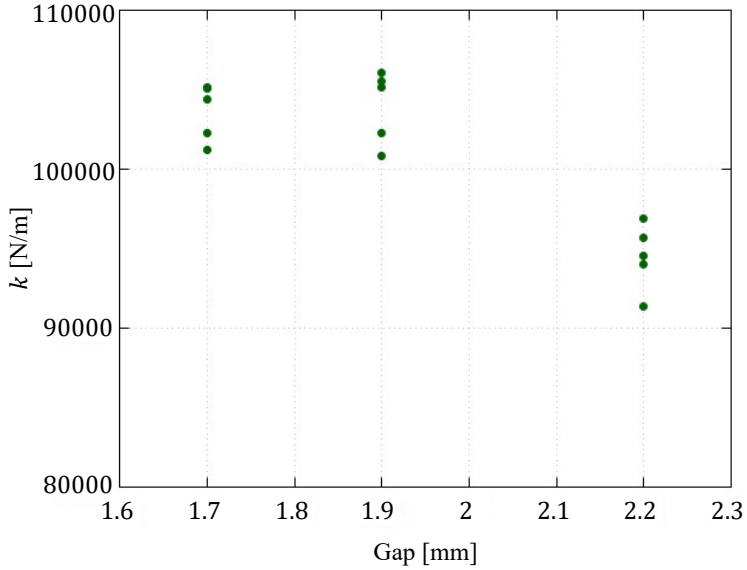

Fig. 6-11: Estimated value of synthetic stiffness k.

6.5 Summary

This chapter proposes a percussion inspection device based on force sensor less control technology to streamline the inspection of stator wedge loosening in generators. The usefulness of the method for detecting the wedge loosening of the generator stator from the striking force and the estimated reaction force obtained by the proposed percussion inspection device is discussed. An experimental device equipped with the proposed percussion inspection device was prototyped, and it was confirmed that the single device could realize the striking and force sensing functions. The proposed device can quantitatively detect the presence or absence of wedge loosening and the degree of loosening through a vibration test on an object that simulates stator wedge loosening. In this study, an inspection method based on the input-output characteristics of force was proposed. The input/output of forces with strikes may be examined from another perspective, that of the relationship between momentum and force product, and this will be a future work. To achieve a fast and precise inspection method using the proposed percussion inspection device, it is desirable to refine the model, including the viscous term, and compare it with the true value.

Chapter 7

Conclusion

The rationalization of the inspection of infrastructure structures is an urgent social issue. One of the solutions to this problem is the introduction of infrastructure inspection robots that can access the inspection target and realize quantitative inspection instead of manual inspection. Intelligent infrastructure inspection robots are expected to expand the range of applications, reduce the number of inspectors and costs, and establish quantitative and sustainable inspection technologies. Infrastructure inspection robots move in and out of the inspection target, interact with the target, and inspect it. The use of force information is inherent in all of these actions. In this dissertation, an approach based on the extraction and application of force information is discussed to develop an intelligent infrastructure inspection robot. Based on the force information, the velocity estimation and motion control of the infrastructure inspection robot and the inspection method of the inside of the structure are discussed.

In Chapter 2, the fundamental techniques for robust motion control and force extraction in this thesis were presented. First, this chapter introduced the disturbance observer (DOB). The DOB is designed to estimate the disturbance to the control target caused by the load and model error based on the nominal model and input-output relationship. Using the DOB, a robust acceleration control system can be constructed. Acceleration is a physical quantity that is generated by a force and produces a change in position. Thus, the acceleration control system can control the position, velocity, and force in a comprehensive manner. Because the DOB has a role in suppressing disturbance, command following characteristics can be designed independent from the disturbance suppression characteristics. Additionally, this chapter introduces the reaction force estimation observer (RFOB). The RFOB estimates the reaction force to the actuator based on the disturbance model such as the friction identified by the DOB. The advantage

of introducing the RFOB is that the performance of the reaction force estimation does not depend on the environment or sensor placement. The introduction of these observers in infrastructure inspection robots that have restrictions on sensor placement and move in extreme environments is highly advantageous. These techniques are also employed in other chapters describing motion control for infrastructure inspection robots and force-information-based structural interior inspection methods.

In Chapter 3, an approach using the DOB and neural networks as a method for estimating the state of an infrastructure inspection robot was discussed. In this chapter, velocity estimation including the slippage of the tracked vehicle employed in the infrastructure inspection robot was specifically addressed. The slippage of tracked vehicles occurs constantly and deteriorates the mobility performance although it is difficult to model because of its complexity. To solve this problem, a translational velocity estimation neural network (TVNN) was constructed to estimate the vehicle velocity including slippage using information correlated with the slippage as input. Another input to the neural network is the disturbance to the crawler mechanism, which is correlated with the slippage, to realize the velocity estimation including the slippage. The system can estimate the state of an infrastructure inspection robot as it moves through an uncertain surrounding environment. In this chapter, an experimental comparison is conducted between the proposed method and conventional methods for the velocity estimation of mobile robots, and the effectiveness of the proposed method is demonstrated based on real data. Furthermore, the training method of the neural network for mobile environments with different friction coefficients (slipperiness) is evaluated by training and evaluating the neural network using multiple environments. A method of applying the proposed method to the three-dimensional movement of an infrastructure inspection robot is realized using the gravity compensation of acceleration, which is one of the inputs of the TVNN, and the effect is demonstrated by experiments.

In Chapter 4, the motion control of the infrastructure inspection robot based on the driving force was discussed. The driving force is the reaction force of the force generated against the road surface and is the dynamics source of the vehicle velocity. In this chapter, a driving force observer (DFOB) based on the vehicle velocity estimated by the TVNN was designed. By feeding back the estimated driving force and controlling it appropriately, the desired vehicle velocity can be achieved, thus suppressing slippage. In the conventional driving force control, the velocity without slip based on the wheel rotation velocity was utilized. However, considering that the driving force is a dynamic source of the vehicle velocity, it is desired to estimate the driving force from the accurate vehicle velocity. Therefore, estimation and control methods of the driving force based on the vehicle velocity including slippage, which is estimated

by the method proposed in Chapter 3, are proposed. The application effect of the proposed driving force control was verified by the experimental evaluation of the slip suppression performance. Although the drive force control can suppress the translational slippage, the interference of the drive force prevents the motion in the turning direction. A driving force distribution method is proposed that utilizes the instantaneous turning center of the vehicle to decouple the crawler. The proposed driving force distribution induces slippage along the turning direction. To ensure the proper tolerance of slippage in the turning direction and to compensate for lateral disturbances including non-holonomic constraints, virtual turning velocity control is proposed. The proposed control system suppresses the equivalent lateral disturbance extracted by the workspace observer (WOB). The experimental results show that the position tracking performance can be improved by appropriately slipping the tracked vehicle while suppressing the lateral disturbance. The tracking performance and stop positioning performance for multiple trajectories by the proposed position control system are confirmed. The velocity estimation and driving force control methods proposed in Chapters 3 and 4 are considered to be applicable to mobile robots traveling in environments where slippage cannot be ignored.

In Chapter 5, a pushing force control mechanism for an infrastructure inspection robot to move adaptively to the target structure was discussed. This chapter presents a pushing force control mechanism to maintain the robot's posture in a narrow space, using an inspection robot in the gap between the rotor and stator of a generator as a subject. The proposed pushing force control mechanism is composed of actuators (motor and air cylinder) and a passive mechanical element. Particularly, for a general air cylinder, the effect of disturbance that prevents precise force control was significant. Therefore, a compensation method using a pre-estimated disturbance model was proposed. The pushing force control performances of the motor- and pneumatic-driven arms were confirmed through experiments. In this chapter, the pushing force control was considered for the primary purpose of posture maintenance. However, in reality, the pushing force is often related to the driving force of the moving mechanism. Therefore, it is necessary to consider the driving force in setting the actual pushing force. The proposed pushing force control mechanism is applicable not only in the generator inspection robots but also in all robots that move in a narrow space while restraining themselves by pushing.

In Chapter 6, a diagnosis method of the condition inside a structure using force information was discussed. In this chapter, a percussion inspection device based on force sensor less control technology is developed to streamline the inspection of generator stator wedge loosening. Additionally, a method of detecting the wedge looseness of the generator stator from the striking force and estimated reaction force

obtained by the proposed device was discussed. This chapter proposes a method to detect abnormal conditions (stator wedge loosening in this chapter) using a coupled vibration model of the internal state of the structure and comparing the model parameters. An experimental device equipped with the proposed percussion inspection device was fabricated, and it was confirmed that a single device can realize the percussion and force sensing functions. Additionally, basic experiments on a target that simulates stator wedge loosening showed that the proposed percussion inspection method is expected to detect stator wedge loosening. Although the subject of this dissertation is the inspection of the stator wedge loosening of a generator, the proposed method can be applied to the inspection of the internal conditions of structures with natural frequencies below the cutoff frequency of the RFOB. Since the proposed percussion inspection method in this chapter considers human sensory information, it can utilize data and technical knowledge from past inspections, facilitating the smooth introduction of the technology. However, some objects cannot be inspected using only human sensory information, which will be an issue in the future.

As described earlier, this dissertation proposes a new methodology for the advancement of inspection robotics. The methodology for realizing advanced inspection robots will become a fundamental technology for infrastructure inspection support and will significantly contribute to solving the urgent issue of labor shortage caused by declining birthrates and an aging population. This dissertation proposes a methodology for realizing the velocity estimation, motion control, environmental adaptation, and inspection functions of infrastructure inspection robots based on force information estimation and application methods. The effectiveness of the proposed methodology was confirmed both theoretically and experimentally. In this dissertation, each method was proposed for subjects such as a tracked vehicle and a generator inspection robot; however, the basic concept and theory are applicable generally. The proposed force-information-based methodology can be expected to help solve social problems using robots.

References

[1] Ministry of Land, Infrastructure, Transport, and Tourism: "White paper on Land, Infrastructure, Transport, and Tourism, 2020", Chapter 2, Section 2, Japan, 2020. (in Japanese)

[2] D. Waleed, S. Mukhopadhyay, U. Tariq, and A. H. El-Hag: "Drone-based ceramic insulators condition monitoring", *IEEE Trans. Instrum. Meas.*, Vol. 70, pp. 1–12, May 2021.

[3] G. Silano, T. Baca, R. Penicka, D. Liuzza, and M. Saska: "Power line inspection tasks with multi-aerial robot systems via signal temporal logic specifications", *IEEE Robot. Autom. Lett.*, Vol. 6, No. 2, pp. 4169–4176, Apr. 2021.

[4] M. Morita, H. Kinjo, S. Sato, T. Sulyyon, and T. Anezaki: "Autonomous flight drone for infrastructure (transmission line) inspection (3)", In *Proc. IEEE ICIIBMS*, pp. 198–201, Nov. 2017.

[5] R. Obradović, I. Vasiljević, D. Kovačević, Z. Marinković, and R. Farkas: "Drone aided inspection during bridge construction", In *Proc. IEEE ZINC*, pp. 1–4, May 2019.

[6] ASM Shihavuddin, X. Chen, V. Fedorov, A. N. Christensen, N. A. B. Riis, K. Branner, A. B. Dahl, and R. R. Paulsen: "Wind turbine surface damage detection by deep learning aided drone inspection analysis", *Energies*, Vol. 12, No. 4, pp. 676–690, Feb. 2019.

[7] J. Kim, J. Lee, and Y. Choi: "LAROB: Laser-guided underwater mobile robot for reactor vessel inspection", *IEEE/ASME Trans. Mechatron.*, Vol. 19, No. 14, pp. 1616–1225, Aug. 2014.

[8] S. Shimono, S. Toyama, and U. Nishizawa: "Development of underwater inspection system for dam inspection: Results of field tests", In *Proc. OCEANS MTS/IEEE Conf.*, pp. 1–4, Sept. 2016.

[9] J. Choi, Y. Lee, T. Kim, J. Jung, and H. Choi: "Development of a ROV for visual inspection of harbor structures", In *Proc. IEEE/OES UT*, pp. 1–4, Feb. 2017.

[10] S. Ray, R. Bhowal, P. Patel, and A. P. K: "An overview of the design and development of a 6 DOF remotely operated vehicle for underwater structural inspection", In *Proc. IEEE ICCISc*, pp. 1–6, Jun. 2021.

[11] A. Hadi, M. Abdollahi, K. Alipour, and B. Tarvirdizadeh: "Design and prototyping a new add-on module to increase traction force of a wheeled sewer inspection robot", In *Proc. RSI/ISM ICRoM*, pp. 254–259, Jul. 2017.

[12] H. Masuta, H. Watanabe, K. Sato, and H. Lim: "Recognition of branch pipe for pipe inspection robot using fiber grating vision sensor", In *Proc. IEEE Int. Conf. URAI*, pp. 633–638, May 2013.

[13] J. Lee, Y. Wu, Y. Jhao, L. Chen, and H. Chen: "Development of mobile robot with vision inspection system and three-axis robot", In *Proc. IEEE ICCRE*, pp. 6–10, Apr. 2018.

[14] M. N. Mohammed, V. S. Nadarajah, N. F. M. Lazim, N. S. Zamani, Omar Ismael Al-Sanjary, Musab A. M. Ali, and S. Al-Youif: "Design and development of pipeline inspection robot for crack and corrosion detection", In *Proc. IEEE ICSPC*, pp. 29–32, Dec. 2018.

[15] M. Dissanayake, T. P. Sattar, O. Howlader, I. Pinson, and T. Gan: "Tracked-wheel crawler robot for vertically aligned mooring chain climbing design, simulation and validation of a climbing robot for mooring chains", In *Proc. IEEE ICIIS*, pp. 1–6, Dec. 2017.

[16] J. Nagase and F. Fukunaga: "Development of a novel crawler mechanism for pipe inspection", In *Proc. IEEE IECON*, pp. 5873–5878, Oct. 2016.

[17] K. H. Cho, Y. H. Jin, H. M. Kim, H. Moon, J. C. Koo, and H. R. Choi: "Multifunctional robotic crawler for inspection of suspension bridge hanger cables: mechanism design and performance validation", *IEEE/ASME Trans. Mechatron.*, Vol. 22, No. 1, pp. 236–246, Feb. 2017.

[18] Guo Rui, Zhang Feng, Cao Lei, and Yong Jun: "A mobile robot for inspection of overhead transmission lines", In *Proc. Int. CARPI*, pp. 1–3, Sept. 2014.

[19] A. Zhu, Y. Tu, W. Zheng, H. Shen, and X. Zhang: "Design and implementation of high-voltage transmission line inspection and foreign bodies removing robot", In *Proc. IEEE Int. Conf. UR*, pp. 852–856, Jun. 2018.

[20] M. Phlernjai, P. Piyathassrikul and P. Ratsamee: "Twist-based crouching motion for multi-legged inspection robot", In *Proc. Int. Symp. ICA-SYMP*, pp. 1–4, Jan. 2021.

[21] P. Kriengkomol, K. Kamiyama, M. Kojima, M. Horade, Y. Mae, and T. Arai: "New tripod walking method for legged inspection robot", In *Proc. IEEE ICMA*, pp. 1078–1083, Oct. 2016.

[22] K. Aihara and K. Ito: "Adaptive switching mechanism of leg stiffness for multi-legged robot", In *Proc. IEEE iEECON*, pp. 1–4, Mar. 2018.

[23] O. Duran, K. Althoefer, and L. D. Seneviratne: "Automated sewer pipe inspection through image processing", In *Proc. IEEE ICRA*, pp. 2551–2556, May 2002.

[24] T. Wu, S. Lu, and Y. Tang: "An in-pipe internal defects inspection system based on the active stereo omnidirectional vision sensor", In *Proc. Int. Conf. FSKD*, pp. 2637–2641, Aug. 2015.

[25] C. J. Salaan, K. Tadakuma, Y. Okada, K. Ohno, and S. Tadokoro: "UAV with two passive rotating hemispherical shells and horizontal rotor for hammering inspection of infrastructure", In *Proc. IEEE/SICE Int. SII*, pp. 769–774, Dec. 2017.

[26] A. Watanabe, J. Even, L. Y. Morales, and C. Ishi: "Robot-assisted acoustic inspection of infrastructures - cooperative hammer sounding inspection", In *Proc. IEEE/RSJ IROS*, pp. 5942–5947, Dec. 2015.

[27] H. Zhong, Z. Ling, C. Miao, W. Guo, and P. Tang: "A new robot-based system for in-pipe ultrasonic inspection of pressure pipelines", In *Proc. IEEE FENDT*, pp. 246–250, Oct. 2017.

[28] D. Zhang, R. Watson, J. Cao, T. Zhao, G. Dobie, C. MacLeod, and G. Pierce: "Dry-coupled airborne ultrasonic inspection using coded excitation", In *Proc. IEEE IUS*, pp. 1–4, Sept. 2017.

[29] M. Togawa, M. Arita, and S. Tanaka: "Non-destructive inspection of concrete structures using an acceleration pickup", In *Proc. SICE-ICASE Int. Joint Conf.*, pp. 5803–5808, Oct. 2006.

[30] Y. Xia, M. Fu, C. Li, F. Pu, and Y. Xu: "Active disturbance rejection control for active suspension system of tracked vehicles with gun", *IEEE Trans. Ind. Electron.*, Vol. 65, No. 5, pp. 4051–4060, May 2018.

[31] S. Morita, T. Hiramatsu, M. Niccolini, A. Argiolas, and M. Ragaglia: "Kinematic track modelling for fast multiple body dynamics simulation of tracked vehicle robot", In *Proc. IEEE Int. Conf. MMAR*, pp. 910–915, Aug. 2018.

[32] Z. Jinzheng, J. Qichun, W. Qi, and Z. Peng: "Analysis and simulation of interaction mechanism between agricultural tracked vehicle and ground", In *Proc. IEEE ICCSEC*, pp. 178–182, Dec. 2017.

[33] Z. Qin, L. Chen, J. Fan, B. Xu, M. Hu, and X. Chen: "An improved real-time slip model identification method for autonomous tracked vehicles using forward trajectory prediction compensation", *IEEE Trans. Instrum. and Meas.*, Vol. 70, pp. 1–12, Jan. 2021.

[34] X. Ding, Z. Wang, L. Zhang, and C. Wang: "Longitudinal vehicle speed estimation for four-wheel-independently-actuated electric vehicles based on multi-sensor fusion" , *IEEE Trans. Veh. Technol.*, Vol. 69, No. 11, pp. 12797–12806, Nov. 2020.

[35] Y. F. Wang, B. M. Nguyen, H. Fujimoto, and Y. Hori: "Multirate estimation and control of body slip angle for electric vehicles based on onboard vision system", *IEEE Trans. Ind. Electron.*, Vol. 61, No. 2, pp. 1133–1143, Feb. 2014.

[36] M. Salah and A. Al-Jarrah: "Robust backstepping control for tracked vehicles under the influence of slipping and skidding", In *Proc. IEEE Int. Conf. REM*, pp. 1–6, May 2019.

[37] R. de Castro, R. Araujo, and D. Freitas: "Wheel slip control of EVs based on sliding mode technique with conditional integrators", *IEEE Trans. Ind. Electron.*, Vol. 60, No. 8, pp. 3256–3271, Aug. 2013.

[38] Z. Ziye, L. Haiou, C. Huiyan, X. Shaohang, and L. Wenli: "Tracking control of unmanned tracked vehicle in off-road conditions with large curvature", In *Proc. IEEE ITSC*, pp. 3867–3873, Oct. 2019.

[39] M. Chen: "Disturbance attenuation tracking control for wheeled mobile robots with skidding and slipping", *IEEE Trans. Ind. Electron.*, Vol. 64, No. 4, pp. 3359–3368, Apr. 2017.

[40] H. S. Kang, C. H. Hyun, and S. Kim: "Robust tracking control using fuzzy disturbance observer for wheeled mobile robots with skidding and slipping", *Int. Jour. Adv. Robot. Syst.*, Vol. 11, No. 1, pp. 1–11, May 2014.

[41] J. Kim and B. K. Kim: "Cornering trajectory planning avoiding slip for differential-wheeled mobile robots", *IEEE Trans. Ind. Electron.*, Vol. 67, No. 8, pp. 6698–6708, Aug. 2020.

[42] J. Y. Wong: "Theory of ground vehicles, 4^{th} edition", *Wiley*, New York, USA, pp. 91–197, Aug. 2008.

[43] P. W. A. Zegelaar, H. B. Pacejka: "The in-plane dynamics of tyres on uneven roads", *J. of Veh. Syst. Dyn.*, Vol. 25, No. 1, pp. 714–730, Jan. 1996.

[44] L. Zhai, X. Zhang, Z. Wang, Y. M. Mok, R. Hou, and Y. Hou: "Steering stability control for four-motor distributed drive high-speed tracked vehicles", *IEEE Access*, Vol. 8, pp. 94968–94983, May 2020.

[45] C. Chatzikomis, A. Sorniotti, P. Gruber, M. Zanchetta, D. Willans, and B. Balcombe: "Comparison of path tracking and torque-vectoring controllers for autonomous electric vehicles", *IEEE Trans. Intell. Veh.*, Vol. 3, No. 4, pp. 559–570, Dec. 2018.

[46] Y. Wang, H. Fujimoto, and S. Hara: "Driving force distribution and control for EV with four in-wheel motors: a case study of acceleration on split-friction surfaces", *IEEE Trans. Ind. Electron.*, Vol. 64, No. 4, pp. 3380–3388, Apr. 2017.

[47] L. Guo, P. Ge, and D. Sun: "Torque distribution algorithm for stability control of electric vehicle driven by four in-wheel motors under emergency conditions", *IEEE Access*, Vol. 7, pp. 104737–104748, Jul. 2019.

[48] K. Ohishi, K. Ohnishi, and K. Miyachi: "Torque-speed regulation of DC motor based on load torque estimation method", In *Proc. of IEEJ IPEC*, pp. 1209-1216, Mar. 1983.

[49] E. Sariyildiz, R. Oboe, and K. Ohnishi: "Disturbance observer-based robust control and its applications: 35th anniversary overview", *IEEE Trans. Ind. Electron.*, Vol. 67, No. 3, pp. 2042–2053, Mar. 2020.

[50] G. Bai, L. Liu, Y. Meng, W. Luo, Q. Gu, and J. Wang: "Path tracking of wheeled mobile robots based on dynamic prediction model", *IEEE Access*, Vol. 7, pp. 39690–39701, Mar. 2019.

[51] N. Ghobadi and S. F. Dehkordi: "Dynamic modeling and sliding mode control of a wheeled mobile robot assuming lateral and longitudinal slip of wheels", In *Proc. IEEE ICRoM*, pp. 150–155, Nov. 2019.

[52] K. Matsushita and T. Murakami: "Nonholonomic equivalent disturbance based backward motion control of tractor-trailer with virtual steering", *IEEE Trans. Ind. Electron.*, Vol. 55, No. 1, pp. 280–287, Jan. 2008.

[53] M. Dissanayake, T. P. Sattar, O. Howlader, I. Pinson, and T. Gan: "Tracked-wheel crawler robot for vertically aligned mooring chain climbing design, simulation and validation of a climbing robot for mooring chains", In *Proc. IEEE ICIIS*, pp. 1–6, Dec. 2017.

[54] A. San-Millan: "Design of a teleoperated wall climbing robot for oil tank inspection", In *Proc. IEEE MED*, pp. 255-261, Jun. 2015.

[55] A. Boonyaprapasorn, T. Maneewarn, and K. Thung-Od: "A prototype of inspection robot for water wall tubes in boiler", In *Proc. IEEE Int. CARPI*, pp. 1–6, Oct. 2014.

[56] A. Ariga, T. Kobayashi, T. Yamaguchi, and S. Hashimoto: "Wall climbing robot in narrow space with pantograph-type structure", In *Proc. IEEE Int. Conf. ROBIO*, pp. 1507–1512, Dec. 2010.

[57] J. J. Park, J. W. Moon, H. Kim, S. C. Jang, D. G. Kim, K. Ahn, S. M. Ryew, H. Moon, and H. R. Choi: "Development of the untethered in-pipe inspection robot for natural gas pipelines", In *Proc. Int. Conf. URAI*, pp. 55–58, Oct. 2013.

[58] Y. S. Kwon, E. J. Jung, H. Lim, and B. J. Yi: "Design of a reconfigurable indoor pipeline inspection robot", In *Proc. IEEE ICCAS*, pp. 712–716, Oct. 2007.

[59] G. Zhang, G. Rossano, W. Eakins, T. Fuhlbrigge, S. Choi, H. Lakhani, and C. Pinto: "A modular air-gap crawler for motor and generator in-situ inspection", In *Proc. IEEE ICIT*, pp. 3166–3171, Mar., 2015.

[60] E. Zwicker and W. Zesch: "A modular inspection robot platform for power plant application", In *Proc. IEEE Int. CARPI*, pp. 1–6, Oct., 2010.

[61] W. Fischer, G. Caprari, R. Siegwart, and R. Moser: "Locomotion system for a mobile robot on magnetic wheels with both axial and circumferential mobility and with only an 8-mm height for generator inspection with the rotor still installed", *IEEE Trans. Ind. Electron.*, Vol. 58, No. 12, pp. 5296–5303, Dec., 2011.

[62] D. Schoeler and P. O. Miranda: "Improved unit reliability and availability through optimised predictive maintenance", *Siemens AG, Power Generation*, Germany, 06 Feb. 2020.

[63] C. Markman and R. J. Zawoysky: "Generator in-situ inspections - a critical part of generator maintenance cost reduction", *GE Energy*, New York, USA, 02 Mar. 2020.

[64] W. Yu, Y. Lv, M. Huang, and B. Yang: "Energy efficiency design for generator slot wedge inspection based on compressive sensing", In *Proc. IEEE ICCA*, pp. 1095–1100, Jun. 2018.

[65] R. Moser and B. Mark: "Automated robotic inspection of large generator stators", In *Proc. of IEEE/ASME Int. Conf. AIM*, pp. 1–5, Sept. 2007.

[66] X. Peng, Z. Jia, S. Gao, Z. Guan, L. Wang, and T. Wang: "A new method for stator slot wedge testing of large generators", *IEEE Trans. Dielectr. and Electr. Insul.*, Vol. 15, No. 4, pp. 933–940, Aug. 2008.

[67] T. Murakami, F. Yu, and K. Ohnish: "Torque sensorless control in multidegree-of-freedom manipulator", *IEEE Trans. Ind. Electron.*, Vol. 40, No. 2, pp. 259–265, Apr. 1993.

[68] K. Ohnishi, M. Shibata, and T. Murakami: "Motion control for advanced mechatronics," *IEEE/ASME Trans. Mechatron.*, Vol. 1, No. 1, pp. 56–67, Mar. 1996.

[69] A. Šabanovic and K. Ohnishi: "Motion control systems," *Wiley-IEEE Press*, pp. 63–107, Mar. 2011.

[70] K. Ohishi, Y. Ohba, and S. Katsura: "Kinematics and dynamics of motion control system based on aceeleration control," *IEEJ Trans. Ind. Appl.*, Vol. 127, No. 6, pp. 545–553, Jun. 2007.

[71] T. Murakami and K. Ohnish: "A study of stability abd workspace decoupling control based on robust control in multi-degrees-of-freedom robot," *IEEJ Trans. Ind. Appl.*, Vol. 113, No. 5, pp. 639–646, May 1993.

[72] S. Katsura, Y. Matsumoto, and K. Ohnish: "Analysis and experimental validation of force bandwidth for force control," *IEEE Trans. Ind. Electron.*, Vol. 53, No. 3, pp. 922–928, Jun. 2006.

[73] S. Kawatsuma, M. Fukushima, and T. Okadai: "Emergency response by robots to Fukushima Daiichi accident: summary and lessons learned," *Int. J. Ind. Rob.*, Vol. 39, No. 5, pp. 428–435, Aug. 2012.

[74] A. Honda, H. Kato, and T. Tsumaki: "Development of simulation system for multi-pair crawlered and transforming explorer," In *Proc. of IEEE IEEE Aerosp. Conf.*, pp. 1–8, Mar. 2015.

[75] T. Shirai and G. Ishigami: "Development of in-wheel sensor system for accurate measurement of wheel terrain interaction characteristics," *J. of Terramechanics*, Vol. 62, pp. 51–61, Dec. 2015.

[76] B. M. D. Wills: "The Measurement of soil shear strength and deformation moduli and a comparison of the actual and theoretical performance of a family of rigid tracks," *J. Agric. Eng. Res.*, Vol. 8, No. 2, pp. 83–88, Jun. 1963.

[77] K. Nagatani, D. Endo, and K. Yoshida: "Improvement of the odometry accuracy of a crawler vehicle with consideration of slippage," In *Proc. IEEE ICRA*, pp. 2752–2757, May 2007.

[78] M. Kurisu, K. Takahashi, T. Konishi, and S. Sarata: "Tracking control for a tracked vehicle based on a virtual wheeled mobile robot," In *Proc. IAARC ISARC*, pp. 482–486, Sept. 2006.

[79] S. G. Zuccaro, S. L. Canfield, and T. W. Hill: "Slip prediction of skid-steer mobile robots in manufacturing environments," In *Proc. ASME IDETC/CIE*, pp. 1–8, Aug. 2017.

[80] H. Fuse and H. Fujimoto: "Driving force controller with variable slip ratio limiter for electric vehicle considering lateral slip based on brush model," In *Proc. IEEE VPPC*, pp. 1–6, Oct. 2019.

[81] T. Hsiao: "Robust wheel torque control for traction/braking force tracking under combined longitudinal and lateral motion," *IEEE Trans. Intell. Transp. Syst.* , Vol. 16, No. 3, pp. 1335–1347, Jun. 2015.

[82] H. Guo, D. Cao, H. Chen, C. Lv, H. Wang, and S. Yang: "Vehicle dynamic state estimation: state of the art schemes and perspectives," *IEEE/CAA J. Auto. Sin.*, Vol. 5, No. 2, pp. 418–431, Mar. 2018.

[83] M. M. Rana, N. Halim, M. M. Rahamna, and A. Abdelhadi: "Position and velocity estimations of 2D-moving object using Kalman filter: Literature review," In *Proc. IEEE ICACT*, pp. 541–544, Feb. 2020.

[84] X. Liang, H. Wang, Y. Liu, Z. Liu, and W. Chen: "Leader-Following formation control of non-holonomic mobile robots with velocity observers," *IEEE/ASME Trans. Mechatron.*, Vol. 25, No. 4, pp. 1747–1755, Aug. 2020.

[85] H. Kato and M. Billinghurst: "Marker tracking and HMD calibration for a video-based augmented reality conferencing system," In *Proc. IEEE/ACM IWAR*, pp. 85–94, Oct. 1999.

[86] R. Faragher: "Understanding the basis of the Kalman filter via a simple and intuitive derivation [Lecture Notes]," *IEEE Signal Processing Mag.*, Vol. 29, pp. 128–132, Sept. 2012.

[87] Z. Sun, Y. Xia, L. Dai, K. Liu, and D. Ma: "Disturbance rejection MPC for tracking of wheeled mobile robot," *IEEE/ASME Trans. Mechatron.*, Vol. 22, No. 6, pp. 2576–2587, Dec. 2017.

[88] M. Tari, S. Nagano, H. Hasegawa, K. Tashiro, S. Murakami, and H. Shimada: "Development of a capacitance measuring robot for the water-cooled stator winding of turbine generators," *IEEE Trans. Energy Convers.*, Vol. 14, No. 4, pp. 1366–1371, Dec., 1999.

[89] H. Kuwahara, A. Matsuzaki, K. Ito, and Y. Arai: "Robotic Inspection Technology Substantially Shortening Time Required for Turbine Generator Inspections," *TOSHIBA Review, Tokyo, Japan*, Vol. 75, No. 6, pp. 52–55, Nov., 2020. (in Japanese)

[90] M. Kurisu: "Tracking control for a tracked vehicle based on prediction model of virtual wheeled robot," In *Proc. IEICE Int. Symp. NOLTA*, pp. 21–24, Sept. 2008.

[91] T. Murakami, N. Oda, Y. Miyazawa, and K. Ohnish: "A motion control strategy based on equivalent mass matrix in multidegree-of-freedom manipulator," *IEEE Trans. Ind. Electron.*, Vol. 42, No. 2, pp. 123–130, Apr. 1995.

[92] D. Saito and T. Murakami: "A turning control of electric wheeled walker device by PSD camera information," In *Proc. IEEE Int. Workshop AMC*, pp. 616–620, Mar. 2014.

[93] J. Wyatt, L. Chua, J. Gannett, I. Goknar, and D. Green: "Energy concepts in the state–space theory of nonlinear n-Ports: I–Passivity," *IEEE Trans. Circuits Syst.*, Vol. 29, No. 7, pp. 417–430, Jul. 1982.

[94] S. Arimoto "Joint-space orthogonalization and passivity for physical interpretations of dextrous robot motions under geometric constraints," *Int. J. of Robust and Nonlinear Control*, Vol. 5, pp. 268–284, Jul. 1995.

[95] R. Ortega, A. Loria, and P.J. Nicklasson "Passivity-based control of Euler-Lagrange systems: applications to mechanical electrical and power systems," *Springer*, London, England, pp. 39–92, 1998.

[96] T. Shibata and T. Murakami "A null space control of two wheels driven mobile manipulator using passivity theory," *IEEJ Trans. Ind. Appl.*, Vol. 127, No. 11, pp. 1109–1116, Nov. 2007.

[97] M. Shibata, K. Isomura, T. Murakami, and K. Ohnishi: "Force sensorless control in a flexible link arm based on estimated reaction torque," *J. of JSPE*, Vol. 63, No. 2, pp. 198–202, Feb. 1997. (in Japanese)

[98] Y. Sudo, Y. Kakinuma, K. Ohnishi, and T. Aoyama: "Development of chatter vibration detection utilizing disturbance observer (1st report) - Precise sensor-less process monitoring utilizing average T method -," *J. of JSPE*, Vol. 77, No. 7, pp. 707–712, Feb. 2011. (in Japanese)

[99] R. Koike, Y. Kakinuma, T. Aoyama, and K. Ohnishi: "Development of chatter vibration detection utilizing disturbance observer (2nd report) - An assorted chatter detection combining moving variance and moving Fourier transform algorithms -," *J. of JSPE*, Vol. 81, No. 7, pp. 692–698, Feb. 2015. (in Japanese)

[100] I. Takeuchi, N. Suzuki, A. Matsui, Y. Mizutani, and S. Katsutra: "Development of a packing-leak tester by high-accuracy force detection," *J. of JSPE*, Vol. 81, No. 3, pp. 242–246, Feb. 2015. (in Japanese)

[101] H. Muramatsu, Y. Kakimi, I. Takeuchi, and S. Katsura: "Package leak detection based on aperiodic anomaly extraction," *IEEE Trans. Emerg. Sel. Topics Ind. Electron.*, Vol. 2, No. 3, pp. 363–370, Jul. 2021.

[102] H. K. Bui, N. Bracikowski, M. Hecquet, K. Zappellini, and J. Ducreux: "Simulation of a large power brushless synchronous generator (BLSG) with a rotating rectifier by a reluctance network for fault analysis and diagnosis," *IEEE Trans. on Ind. Appl.*, Vol. 53, No. 5, pp. 4327–4337, May 2017.

[103] J. Ye, T. Kobayashi, M. Iwata, and M. Murakawa: "Noise robust hammering echo analysis for concrete structure assessment under mismatch conditions: A sparse coding approach," In *Proc. IEEE SAS*, pp. 1–6, Mar. 2017.

[104] H. Fujii, A. Yamashita, and H. Asama: "Automated recognition of material condition using boosting algorithm in hammering test," *J. of JSPE*, Vol. 80, No. 9, pp. 844-850, Sept. 2014. (in Japanese)

[105] T. Tsuruta, K. Yamazaki, K. Ishikawa, and A. Haga: "Impedance measuring to detect fractures in steel frames using resonance circuit on fire resistive covering," *IEEE Trans. Magnetics*, Vol. 49, No. 7, pp. 4036–4039, Jul. 2013.

[106] R. T. Verrillo, A. J. Fraioli, and R. L. Smith: "Sensation magnitude of vibrotactile stimuli," *Perception & Psychophysics*, No. 6, pp. 366–372, Nov. 1969.

List of Achievements

Journals (First Author)

[1] Hiroaki Kuwahara and Toshiyuki Murakami, "Position control considering slip motion of tracked vehicle using driving force distribution and lateral disturbance suppression," *IEEE Access*, vol. 10, pp. 20571-20580, 2022.

[2] Hiroaki Kuwahara and Toshiyuki Murakami, "Tracked vehicle velocity estimation by disturbance observer and machine learning, and its application to driving force control for slippage suppression," *IEEJ Journal of Industry Applications*, vol. 11, no 1, pp. 69-65, 2022.

[3] Hiroaki Kuwahara, Motoki Kokubu, Takahiro Mizoguchi, Tomoyuki Shimono, and Kouhei Ohnishi, "Development of a force sensorless percussion inspection device for detecting internal defects in structures," *Inspection Technology*, Japan Industrial publishing, vol. 26, no. 6, pp. 13–16, 2021. (in Japanese)

[4] Hiroaki Kuwahara, Takahiro Mizoguchi, Tomoyuki Shimono, and Kouhei Ohnishi, "Development of a force sensorless percussion device for rationalization of generator inspection," *Journal of the Japan Society for Precision Engineering*, vol. 86, no. 1, pp. 120–126, 2020. (in Japanese)

[5] Hiroaki Kuwahara, Tomoyuki Shimono, Hiroyuki Tanaka, Daisuke Yashiro, and Kouhei Ohnishi, "Abstraction of action components unconstrained by alignment of haptic sensing points," *IEEE Transactions on Industrial Electronics*, vol. 58, no 8, pp. 3196–3204, 2011.

[6] Hiroaki Kuwahara, Shigeru Susa, Syoyo Hyodo, and Kouhei Ohnishi, "Design method for a bilateral control system considering ambient environment around operated objects," *IEEJ Transactions on Industry Applications*, vol. 129, no. 6, pp. 649–657, 2009. (in Japanese)

Journals (Co-author)

[1] Takahiro Mizoguchi, Hiroaki Kuwahara, and Kouhei Ohnishi, "A design method of force dependent velocity bilateral control based on gyrator property," *IEEJ Transactions on Industry Applica-*

tions, vol. 131, no 3, pp. 304–310, 2011.

[2] Yusuke Suzuki, Hiroaki Kuwahara, Masataka Sato, Kei Mikami, and Kouhei Ohnishi, "Force sensation transmission with same-structured master-slave robot hands using flexible actuators," *Journal of the Japan Society for Precision Engineering*, vol. 76, no 8, pp. 938–944, 2010.

International Conferences (First Author)

[1] Hiroaki Kuwahara, and Toshiyuki Murakami, "Trajectory tracking control with estimated driving force for tracked vehicle using disturbance observer and machine learning," in *Proceedings of the IEEE International Symposium on Industrial Electronics, ISIE 2020, Kyoto, Japan*, June 20–23, 2021.

[2] Hiroaki Kuwahara, and Toshiyuki Murakami, "Tracked vehicle velocity estimation by disturbance observer and machine learning, and its application to driving force control for slippage suppression," in *Proceedings of the IEEJ International Workshop on Sensing, Actuation, Motion Control, and Optimization, SAMCON 2021, Tokyo, Japan*, March 10–12, 2021.

[3] Hiroaki Kuwahara, Kazuma Hiraguri, and Fujio Terai, "Development of pushing control mechanisms for generator inspection robot," in *Proceedings of the IEEE International Workshop on Advanced Motion Control, AMC 2020, Kristiansand, Norway*, pp. 135–142, September 14–16, 2020.

[4] Hiroaki Kuwahara, Fujio Terai, Michele Focchi, Gustavo Andres Medrano-Cerda, Darwin G. Caldwell and Claudio Semini, "A design method of a robust controller for hydraulic actuation with disturbance observers," in *Proceedings of the IEEE International Workshop on Advanced Motion Control, AMC 2016, Auckland, New Zealand*, pp. 289–296, April 22–24, 2016.

[5] Hiroaki Kuwahara, Hiroyuki Tanaka, Yusuke Suzuki, Kouhei Ohnishi, "A reproduction method of human motion based on integrated information for haptic skill education," in *Proceedings of the IEEE International Workshop on Advanced Motion Control, AMC 2010, Nagaoka, Niigata, Japan*, pp. 307–312, March 21–24, 2010.

[6] Hiroaki Kuwahara, Kouhei Ohnishi, Noboru Tsunashima, and Seiichiro Katsura, "Design method for motion reproduction system including time scaling based on robot dynamics," in *Proceedings of the IEEE International Conference on Industrial Technology, ICIT, 2010, Vina del Mar, Chile*, pp. 483–488, March 14–17, 2010.

[7] Hiroaki Kuwahara, Tomoyuki Shimono and Kouhei Ohnishi, "Abstraction of action components based on haptic information," in *Proceedings of the IEEE International Conference on Human System Interactions, HSI 2009, Catania, Italy*, May 21–23, 2009.

International Conferences (Co-author)

[1] Masamitsu Kurisu and Hiroaki Kuwahara, "Development of a tiny impact device for hammering inspection," in *Proceedings of the International Conference on Control, Automation and Systems, ICCAS 2018, PyeongChang, GangWon, Korea*, pp. 494–499, October 17–20, 2018.

[2] Masataka Sato, Tomoyuki Shimono, Hiroaki Kuwahara, Yusuke Kasahara, and Kouhei Ohnishi, "Evalution mehtod of haptic human motion by modal work information," in *Proceedings of the IEEE International Workshop on Advanced Motion Control, AMC 2010, Nagaoka, Niigata, Japan*, pp. 46–49, March 21–24, 2010.

[3] Yusuke Suzuki, Hiroaki Kuwahara, Hiroyuki Tanaka, and Kouhei Ohnishi, "Development and verification of tendon-driven rotary actuator for haptics with flexible actuators and a PE line," in *Proceedings of the IEEE International Workshop on Advanced Motion Control, AMC 2010, Nagaoka, Niigata, Japan*, pp. 484–489, March 21–24, 2010.

Domestic Conferences (First-author)

[1] Hiroaki Kuwahara, and Toshiyuki Murakami, "A velocity estimation method of tracked vehicle based on disturbance observer and machine learning", in *Proceedings of the IEEJ/IAS (D) Online Technical Meetings, DOTeM 2020*, pp. 19–24, September, 2020.

[2] Hiroaki Kuwahara, Takahiro Mizoguchi, Seiji Yamaoka, Maki Fukagawa, Tomoyuki Shimono and Kouhei Ohnishi, "Development and evaluation of force sensorless percussion system for application to inspection robot for infrastructure", in *Proceedings of the Semestrial Meetings of JSPE, Osaka, Japan*, pp. 483–484, September, 2017.

[3] Hiroaki Kuwahara, and Kouhei Ohnishi, "A description method of environmental information based on real-world haptics", in *Proceedings of the Annual Conference of IEEJ Industry Application Society, JIASC 2009, Kohchi, Japan*, pp. 311–316, August, 2009.

[4] Hiroaki Kuwahara, and Kouhei Ohnishi, "A method of motion guide system based on individual action features", in *Proceedings of the IEEJ Technical Meeting on Industrial Instrumentation and Control, IIC 2009, Tokyo, Japan*, pp. 67–72, March, 2009.

[5] Hiroaki Kuwahara, and Kouhei Ohnishi, “A method of grasped object passing system based on modal decomposition”, in *Proceedings of the Annual Conference of IEEJ Industry Application Society, JIASC 2008, Kohchi, Japan*, pp. 53–58, August, 2008.

[6] Hiroaki Kuwahara, Shigeru Susa, Syoyo Hyodo, and Kouhei Ohnish, “A design method of bilateral control taking ambient environment into account”, in *Proceedings of the IEEJ Technical Meeting on Industrial Instrumentation and Control, IIC 2008, Tokyo, Japan*, pp. 91–96, March, 2008.

Domestic Conferences (Co-author)

[1] Takahiro Mizoguchi, Yusuke Kasahara, Hiroaki Kuwahara, Kazuya Kitamura, and Kouhei Ohnishi, “A design method of bilateral control system for user-friendly haptic interfaces”, in *Proceedings of the IEEJ Technical Meeting on Industrial Instrumentation and Control, IIC 2010, Tokyo, Japan*, pp. 19–24, March, 2010.

[2] Keisuke Sugawara, Atsushi Suzuki, Hiroaki Kuwahara, and Kouhei Ohnishi, “Modeling of nonlinear factor in thrust wires and application to bilateral system”, in *Proceedings of the IEEJ Technical Meeting on Industrial Instrumentation and Control, IIC 2010, Tokyo, Japan*, pp. 25–30, March, 2010.

[3] Wataru Motooka, Yusuke Suzuki, Daisuke Yashiro, Hiroaki Kuwahara, and Kouhei Ohnishi, “Dymanic property analysis of real environments using a two degrees-of-freedom haptic forceps robot”, in *Proceedings of the IEEJ Technical Meeting on Industrial Instrumentation and Control, IIC 2010, Tokyo, Japan*, pp. 31–36, March, 2010.

[4] Yusuke Kasahara, Hiroaki Kuwahara, Tomoyuki Shimono, Masataka Sato, and Kouhei Ohnishi, “Motion recognition based on a concept of modal power”, in *Proceedings of the IEEJ Technical Meeting on Industrial Instrumentation and Control, IIC 2009, Tokyo, Japan*, pp. 53–58, March, 2009.

[5] Yusuke Suzuki, Hiroaki Kuwahara, Masataka Sato, Kei Mikami, and Kouhei Ohnishi, “Development of same structured master-slave robot hands using thrust wires”, in *Proceedings of the IEEJ Technical Meeting on Industrial Instrumentation and Control, IIC 2009, Tokyo, Japan*, pp. 67–72, March, 2009.

Awards

[1] JSPE Young Engineer Award

the Japan Society for Precision Engineering (JSPE)

Date: September 22, 2022.

[2] Excellent Presentation Award

Industry Applications Society (IAS), the Institute of Electrical Engineers of Japan (IEEJ)

Date: August 25, 2022.

[3] Excellent Presentation Award

Technical Committee on Mechatronics (MEC), Industry Applications Society (IAS), the Institute of Electrical Engineers of Japan (IEEJ)

Date: January 6, 2021.

[4] JSPE Best Presentation Award

the Japan Society for Precision Engineering (JSPE)

Date: September 22, 2017.

[5] Excellent Presentation Award

Industry Applications Society (IAS), the Institute of Electrical Engineers of Japan (IEEJ)

Date: August 25, 2010.

[6] Excellent Research Activities Award (Master Course)

Keio University

Date: March 25, 2010.